Politecnico di Torino

Politecnico di Torino

Master Degree in Environmental and Land Engineering
Climate Change

Glacier modeling with geophysical data constraints: a case study on the Indren Glacier (NW Italy).

Supervisor:
Chiara Colombero

Co-supervisor:
Andrea Vergnano

Candidate:
Valeria Strallo

Sessione di Laurea Marzo 2023

A.a. 2022/2023

Abstract

The increase in global temperature over the last years has caused the loss of a significant amount of ice bodies all over the world. In particular, mountain or alpine glaciers have shown higher sensitivity to climate variations compared to other glacial environments due to their elevation and reduced areal extent. The consequences of ice melting in Alpine regions include natural hazards, shortage of the water resource for drinking, agricultural and power generation purposes, ecological impacts and economic repercussions on local communities. In these areas, it is therefore essential to analyze variations in ice volume to understand the evolution of glaciers and their response to climate change, as well as to implement effective adaptation measures for these highly vulnerable spots.

This thesis aims to utilize acquisition and modeling techniques to estimate glacial thickness, with the goal of characterizing and monitoring the impacts of climate change on Alpine Glaciers. The Indren Glacier (NW Italian Alps) is selected as test site for the application of the considered methodologies. An analysis of both external and internal variations is carried out on this glacier.

The first fast assessment of ice thickness variations over time was conducted considering the Digital Elevation Models of the area for three different years (1999, 2008 and 2018), covering a time span of more than 20 years from the present days. Despite the different resolution of the considered models, this first study provides a rough estimation of the variations in the glacier's surface topography over the last two decades. It was obtained that the highest elevation variations have occurred between 2008 and 2018. These results are also confirmed by a temperature increase registered over this decade at the closest weather station.

For the analysis of the internal variations, the measurement and quantification of the ice thickness was required. First, Ground Penetrating Radar (GPR) data, acquired in 2020 with a 200-MHz and 70-MHz antenna, were processed and interpreted. This geophysical instrument is ideal for depth estimation in glacial environments due to the low electrical conductivity of ice, which preserves the electromagnetic signal from strong attenuation and enables deep penetration. However, this device loses effectiveness when encountering water-rich or temperate ice. In addition, since GPR data is usually acquired over a sparse network of linear profiles, a bottom topography modeling was required to obtain ice thickness in areas not covered by radar surveys. For this purpose, it was chosen to combine the GPR data with the glaciological model of Clarke et al. (2013) through the Glacier Thickness Estimation (GlaTE) algorithm, which is able to minimize the mismatch between observed and predicted data. The application of GlaTE model to the Indren Glacier demonstrated the benefits of introducing empirical data to constrain the theoretical model, which otherwise significantly underestimated the ice thickness.

Finally, a preliminary temporal study of the Indren Glacier was also performed, exploiting historical open access data and the Minimal Glacier Model, as tool for the analysis of internal variations. This model allowed for the investigation of the fundamental connections between the glacier's length and the climate, as well as ice thickness. The model's simplicity and limited historical data for calibration prevented robust results, but it could be a starting point for more complex models.

Acknowledgments

I would like to thank my supervisor, Chiara Colombero, and co-supervisor, Andrea Vergnano, for their guidance and support throughout this work. They have not only provided me with the necessary technical knowledge but also instilled me their passion and curiosity for geophysics.

I would also like to express my gratitude to Museo Nazionale della Montagna for providing valuable historical materials relevant to the glacier I have studied. Their help and availability has been crucial for enriching my research.

I would also like to thank my mother for her love, encouragement and support throughout my academic journey. Her unwavering faith in me has always given me the strength to overcome all the challenges I have encountered during this experience.

I also want to thank my sister, Giulia, who has been a constant source of guidance and support throughout my whole life. Her love and optimism have taught me to approach life in a cheerful and lighthearted way.

Finally, I would like to thank my friends, who have always been there for me and with laughter and support made this journey much easier and exciting.

Table of Contents

List of Figures

List of Tables

1 Introduction

1.1 Why studying glaciers and focusing on European Alps?

Over the last years the continue increase in the average global temperatures has led to significant losses in ice bodies all over the world. Every year, 750 billion tons[1] of ice melt due to global warming, ending into the sea and contributing to the sea level rise. This can have severe consequences for coastal communities, as it can lead to flooding as well as erosion and other issues.

Glacier monitoring and research is crucial for understanding and managing climate change as these elements are particularly vulnerable spots and respond rapidly to climate variations. The detailed analysis of ice mass changes in glacial environments can also yield valuable information for forecasting future scenarios.

Between the different glacier bodies, mountain or alpine glaciers have been found to be more reactive to temperature variations, responding more quickly to climate change than environments at lower elevations (Pepin, et al. 2015). As an example, the mean global air temperature has risen up to 0.74 ± 0.18 °C between 1906 and 2005, while the European Alps saw an increase of double that amount (Giaccone, et al. 2015). Other studies confirmed that the average temperature in these environments, has indeed risen up to 2 °C between the end of 19th century and the early 21st century, owing to the strong warming acceleration registered since 1990s (Tognetto, et al. 2021). The reason behind such a strong response of mountain glaciers to climate forcing lies not only on their elevation, but also on their small size and high mass turnover rates (Colombero, et al. 2019), which enhance their sensitivity to external factors.

As a consequence, the European Alps have experienced some of the most significant glacier shrinkage due to global temperature rising, with an average thickness reduction of 24 m registered between 1997 and 2017[2].

Studies conducted over a series of European glaciers (Figure 1) have shown that starting from 1997 these have been subject to a mass loss ranging between 8 and 25 m of lost thickness[3].

[1] https://www.theworldcounts.com/challenges/climate-change/global-warming/the-melting-ice-caps
[2] https://climate.copernicus.eu/alpine-glaciers
[3] ESOTC 2018 Headline Climate Indicators – Glaciers, Climate Copernicus EU, https://climate.copernicus.eu/glaciers-0

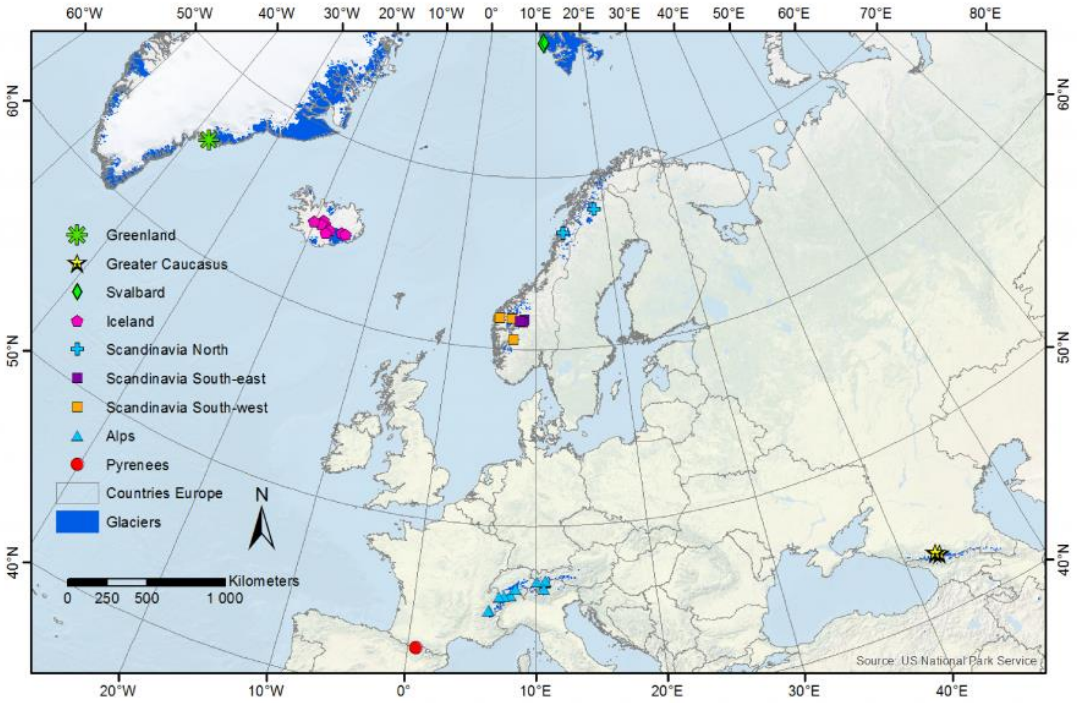

Figure 1: *Geographic distribution of glaciers in Europe. Blue areas highlight the regions covered by glaciers. Colored symbols indicate the location of the reference glaciers used for the calculation of glacier mass balance changes in Europe. Data source: RGI Consortium (2017). Glacier outlines from RGI (2017), location of glacier mass balance series from WGMS (2017), background map from US National Park Service. Credit: WGMS/Copernicus Climate Change Service (C3S)*[4].

Figure 2 illustrates the cumulative mass balance in meter water equivalent (m w.e.) relative to 1997 for the considered glaciers. It is interesting to notice how, even though between 1975 and 1980 there has been a mass increase, the Alps have been subject to an intense and continue mass loss starting from 1997, which was even the strongest observed for all the European glaciers.

[4] Ibid., https://climate.copernicus.eu/glaciers-0

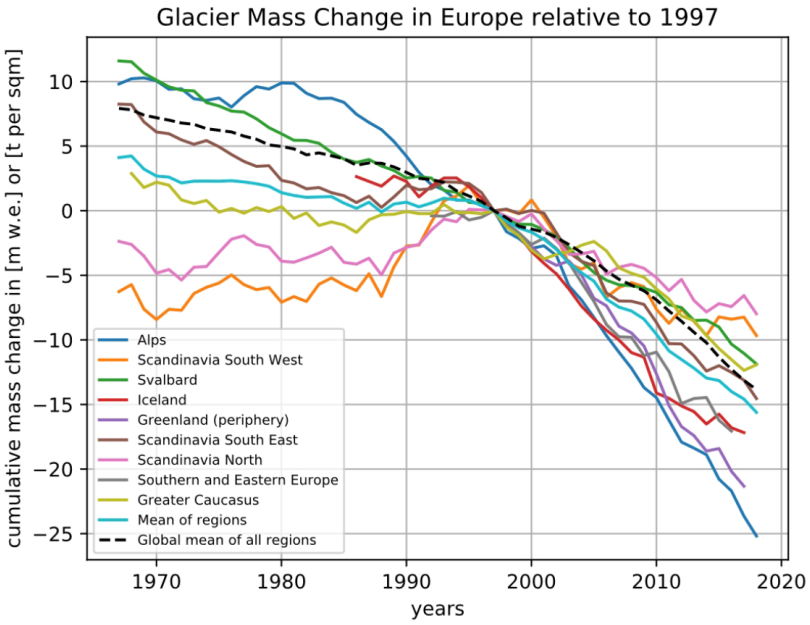

Figure 2: *Cumulative glacier mass changes in Europe from 1967-2018 for glaciers with long-term records in nine different regions. Data source: WGMS (2017, updated). Credit: WGMS /Copernicus Climate Change Service (C3S)*[5].

At the regional scale, Italian glaciers have experienced a large areal decrease due to climate change starting from 1957. In particular, the reduction of ice extension and thus the glacier's fragmentation has led to an increase in the number of small glaciers between 1957 and 2007 (Baroni, et al. 2018). Then, between 2007 and 2015, the continuous increase of temperature and consequent glacier's shrinkage has led to the extinction of these smaller glaciers (Figure 3).

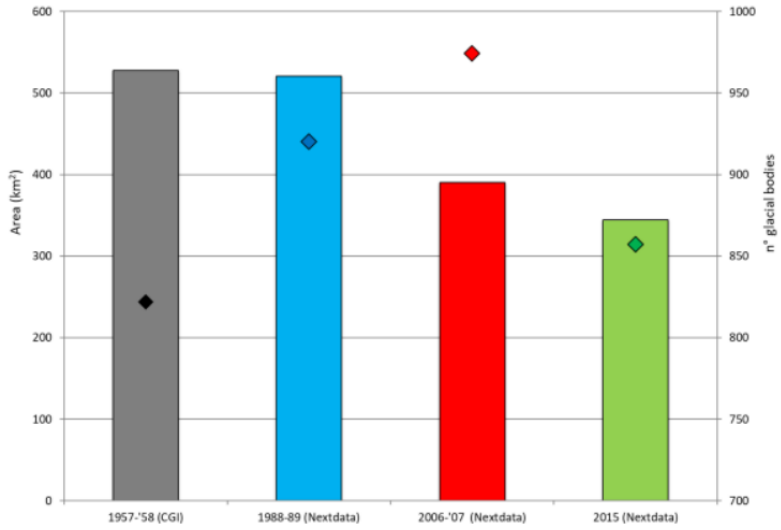

Figure 3: *Areal extent (bar chart) and number of Italian glacial bodies (diamonds) for different timesteps* (Baroni, et al. 2018).

[5] Ibid., p. 10.

The Alps represent an extremely important source for the European local and regional hydrogeological cycle (Colombero, et al. 2019). Four of the major rivers of the continent (Danube, Rhine, Po and Rhone) originate from this area. The water amount stored in Alpine glaciers and then released as runoff in these rivers is used for drinking, agricultural and power generation purposes.

Therefore, ice loss from these areas can have serious consequences for both the environment and local communities not only in the immediate area, but also downstream, far from the source areas. Researches show that "by the end of the century, Europe's mountain cryosphere will have changed to an extent that will impact the landscape, the hydrological regimes, the water resources, and the infrastructure" (Beniston, et al. 2018). As a matter of fact, with climate change, an increase of temperature and a shift from solid to liquid precipitation in these areas is predicted to occur. This will lead to an upward movement of seasonal snow lines to higher elevations and a shortage of the snow period. The result will be a modification in the timing of discharge maxima and in the runoff regimes, affecting the seasonality of water availability and storage. From a quantitative point of view this will result in a shortage of freshwater during dry season. Qualitatively, an increase of sediments and other pollutants in water bodies released by the melted ice will be registered (Milner, et al. 2017).

Glacier-related hazards connected to ice loss must be taken into account too. With ice melting, water accumulation at the bottom of the glacier, between the ice and the bedrock, may occur. Hazardous consequences may involve the outburst of the so-formed endoglacial or subglacial lakes, rapidly releasing a large amount of water that can cause floodings, ice and debris avalanches downstream. Ice melting contributes also to uncover debris present on the glaciers' surface and this may lead to debris flow occurrence. Further evidences have shown that glacial melting can cause an increase in landslides occurrence (Liu, Wu and Gao 2021).

Moreover, it is important to mention that the loss of tourism revenue in areas where glaciers are the major attraction can have severe socioeconomic impacts. As a matter of fact, many alpine communities rely on skiing tourism as their main economical income. With global warming, the possibility to find available ice during all year for skiing purposes is becoming more and more challenging.

Finally, ecological impacts related to glaciers ice melting have to be considered. Several species living in mountainous water streams need cold water temperatures to survive. Some aquatic insects, fundamental components of the food web, are especially sensitive to stream temperature and cannot survive without the cooling effects of glacial meltwater. Such changes in stream habitat may also adversely impact native trout and other keystone salmon species [6]. Additionally, glacier retreat leads to an upward shift of the tree line and consequently an increase of exposed terrain for plant colonization (Beniston, et al. 2018). A research conducted over a herbage sample, has demonstrated how, with glacier extinction, plant diversity may initially increase but more than a fifth of plant species will decline and eventually disappear (Losapio, et al. 2021). On top of that, for the species subject to an increase, rising competition could lead to negative impacts and cascade effects, threatening the ecosystem.

[6] https://www.usgs.gov/faqs/what-are-impacts-glacier-loss-other-losing-aesthetic-landscape-feature

A deep study of ice thickness and volume variations over the past years can help in understanding the glacier's evolution, as well as the cryosphere-climate interaction, and consequently model future scenarios. In this way it is possible to implement the best adaptation measures for these highly vulnerable areas.

1.2 Thesis objective

This thesis primarily focuses on the analysis of field and modeling tools for a reliable quantitative estimation of glacial thickness, in the light of characterization and monitoring of the climate-related ongoing modifications on Alpine Glaciers. For this purpose, Indren Glacier (NW Italian Alps) was selected as a test site for the application of the selected field and modeling methodologies. This work takes advantage of multidisciplinary techniques to analyze the glacier variations over time, considering that, for an exhaustive glacier analysis, it is at least necessary to define its outline, its surface topography and the bottom topography of the bedrock. The investigation of the first two properties allowed for the analysis of superficial variations (Section 3 (Analysis of Superficial Variations)) of the glacier in question, which represents the first phase of this study. These were investigated through remote sensing techniques, which represent an effective tool to obtain good results for hard-to-reach areas with reduced costs and working time with respect to traditional techniques (Lucchesi, Giardino and Perotti 2013). The estimation of the ice thickness (and consequently the bottom morphology) is particularly challenging since geophysical surveys cannot cover the whole surface of the glacier, due to logistical reasons. Furthermore, at the current state, there is no remote sensing technique able to image the subglacial topography. The definition of the ice thickness, and therefore the bottom morphology of a glacier, is of fundamental importance, because it, together with the surface topography, makes it possible to determine changes in its ice volume over time (Colombero, et al. 2019). This information also allows for predicting future scenarios for areas that will be exposed as the glacier retreats. In this work, for the estimation of the Indren Glacier ice thickness, as well as its relation to other parameters, a second analysis (Section 4 (Analysis of Internal Variations)) was conducted by taking into account different techniques.

At the moment, one interesting tool for the ice thickness estimation is the Ground Penetrating Radar (GPR, also called echo-sounding). However, the utilization of GPR data alone does not provide a comprehensive depiction of the bottom topography of a glacier. This is due to the fact that GPR data is usually obtained from a limited set of profiles, resulting in sparse coverage. Thus, the estimation of ice depth through only echo-sounding data cannot be considered complete and can lead to strong inaccuracies. The implementation of a model is therefore required.

Over the years different models for the ice thickness estimation of glaciers have been developed. These types of models can be based on geometric properties, like the one developed by Clarke et al. (2013), or on glacier-physics properties, like the method developed by Farinotti et al. (2017) which is based on glacier mass turnover and ice flow mechanics (Clarke, et al. 2013). However these methods could lead to high levels of uncertainty. The physical relations and basic assumptions adopted for thickness estimation may indeed oversimplify the problem and may not be suitable for site-specific estimations. In addition,

most of these models lack any calibration or validation with local or areal information retrieved from field measurements.

In this work, GPR data were combined together with the recently developed Glacier Thickness Estimation algorithm (GlaTE), to estimate the Indren Glacier ice thickness. The choice of the GlaTE model for this study relies on the fact that this algorithm is able to constrain the glacial model with field data (GPR in particular) to minimize the discrepancies between observed and predicted data (Langhammer, et al. 2019). This represents an interesting tool to obtain more reliable results for ice thickness estimations. Moreover, this model shows a high flexibility because it is able to work with any type of glacial model present in literature and it allows to add any additional constrain to the model in a straightforward way. Additionally, this is a static model, therefore it describes the site of interest from a spatial point of view, without need of historical information regarding the evolution of the glacier. For the implementation of the algorithm, GPR data, as well as aerial and satellite images were used, whereas the model developed by Clarke et al. (2013) was used as glaciological constraint.

Additionally, to provide a complete understanding, a preliminary temporal analysis of the glacier in question was performed as part of the Analysis of Internal Variations. For this purpose, the Minimal Glacier Model (MGM), developed by Oerlemans (2011), was used. This model allowed to roughly investigate the Indren Glacier's length-climate relationship over the area of interest considering the geometrical historical data of the glacier and the temperature trends in that area. Through simple assumptions, as well as few input parameters, this model also allowed to investigate the relationships between the length and the thickness of Indren Glacier.

Figure 4 shows the structure of this thesis, with the two main sections and the relative tools used for both analysis.

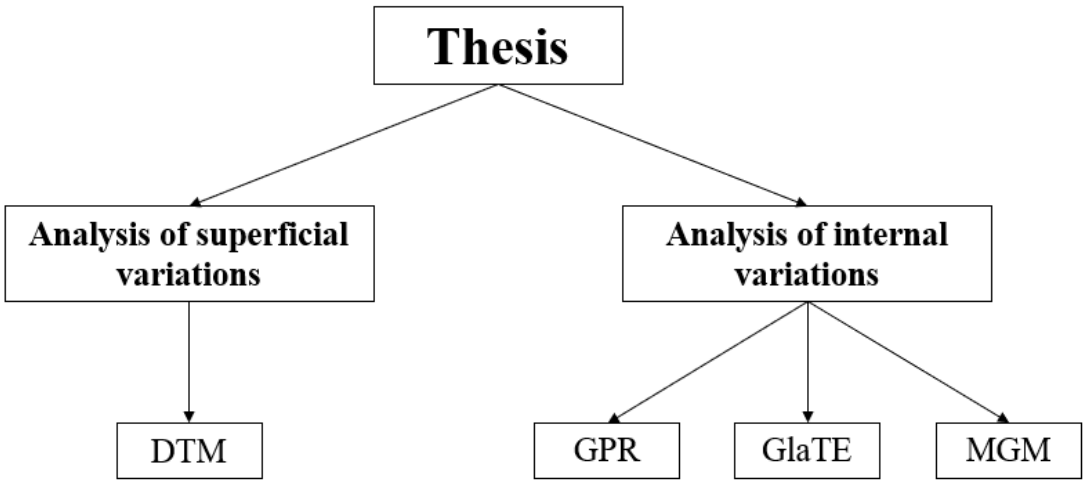

Figure 4: *Block diagram showing the structure of the thesis: Analysis of superficial variations conducted by means of Digital Terrain Models; Analysis of internal variations conducted both with measurement tools (i.e., Ground Penetrating Radar) and modelling techniques (i.e., Glacier Thickness Estimation algorithm and Minimal Glacier Model).*

The work will be subdivided into five sections, being the first two, Section 1 (Introduction) and Section 2 (Test Site: The Indren Glacier), respectively. Section 3 (Analysis of Superficial

Variations) will address the evaluation of the Digital Elevation Models of the area of interest over the years, providing for a first fast assessment of the glacier's thickness variation. This section will be subdivided in three sub-sections: Section 3.1 (Available data and acquisition techniques), where a brief description of the used data will be performed; Section 3.2 (Methodology), where the methods used for the processing of the rough data will be addressed and Section 3.2 (Results), where the obtained outcomes from the previous analysis will be displayed. Section 4 (Analysis of Internal Variations), will be subdivided into Section 4.1 (Methodology) and Section 4.2 (Results). Both of the last two sub-sections will deal with the three different tools, GPR, GlaTE, MGM. Finally, in Section 5 (Discussion) the results obtained through the different tools will be analyzed.

Although the aforementioned techniques will be addressed separately in this work, it is worthy to remember that their integration and combination into a unified investigation is what provided an exhaustive and comprehensive analysis of the site of interest.

The reason for selecting the European Alps, and Indren Glacier in particular, was driven by both the vulnerability of the area and the rich amount of data that has been collected in this region over the years. As a matter of fact, the deep interaction between humans and mountains in this region, made possible a "long and rich" glacier science history in these areas, putting down the roots for the international glacier research (Haeberli, Oerlemans and Zemp 2019). Thus, the availability of both remote sensing and in situ measurements made it interesting to study and model this area through a comprehensive analysis.

2 Test Site: the Indren Glacier

The Indren Glacier is an Italian Alpine glacier located at the top of the Lys and Sesia valleys, in the Aosta Valley region, at the border with Piedmont. It is found on the Monte Rosa massif which belongs to the Italian Pennine Alps (NW Italian Alps, Figure 5). In this area, the Monte Rosa massif results from the collision of the European continental margin and Ocean crust units from the Tethys (Tognetto, et al. 2021).

The glacier is located at the foot of Vincent Pyramid and it feeds the Lys stream. It oriented towards South[7] and is in direct contact with a proglacial pond (Colombo, et al. 2019). Glacial processes have been the main drivers of the geomorphological evolution of this area. However, in the last period mostly erosional and depositional landforms due to gravitational processes have contributed most in shaping the area (Tognetto, et al. 2021). The Aosta Valley, likewise, the other alpine regions, has shown a strong glacier retreat starting from the end of the Little Ice Age (LIA), having lost c.a. 60% of its glacierized area (Viani, Machguth, et al. 2017).

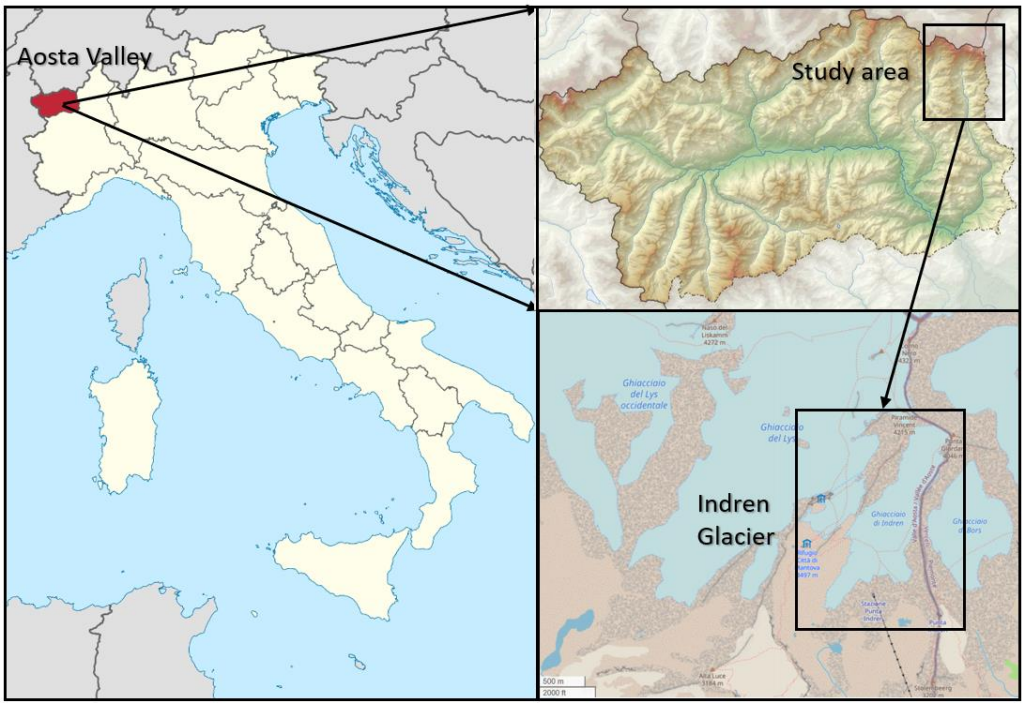

Figure 5: *Geographical location of the site of interest. Left panel: location of the Aosta Valley region[8]. Upper right panel: focus on the location of the study area[9]. Lower right panel: focus on the Indren Glacier location[10].*

On average, the annual air temperature near the glacier terminus is -4°C, with an annual precipitation of 1500 mm (Freppaz, et al. 2021). Snow usually persists from early October to late June (Freppaz, et al. 2021). According to the Gabiet weather station, located 4 km away from the glacier, in the last century the maximum air temperatures have increased of

[7] https://sites.unimi.it/glaciol/wp-content/uploads/2019/02/4-valle-daosta.pdf
[8] https://it.wikipedia.org/wiki/Valle_d%27Aosta
[9] https://www.freeworldmaps.net/europe/italy/aostavalley.html
[10] https://www.sentieridellealpi.it/2021/05/31/sentieri-delle-alpi-da-punta-indren-al-rifugio-gnifetti/

0.015°C/year, while the number of rainy precipitation days have increased of 0.17 days/year (Colombo, et al. 2019). Fresh snow has instead decreased of 1.75 cm/year (Colombo, et al. 2019), also snow cover permanence reductions have been observed (Giaccone, et al. 2015). Between 1927 and 2013, the Indren Glacier has retreated around 500 m (Colombo, et al. 2019). In 2018 the glacier's elevation ranged between 3085 and 4046 m. In 2019 the estimated covered area of the glacier was around 0.9 km^2 and the elevation of the terminus was located at 3130 m (Tognetto, et al. 2021). Furthermore, evidences have shown that starting from 1850 the glacier front has retreated of 1 km (Viani, Machguth, et al. 2020).

In the past years Indren Glacier was composed by two lobes, a larger one and a smaller one on the western part (Figure 6). In 1970s the glacier has become an important touristic attraction, owing to the construction of a ski lift and the presence of the Monterosa Ski resort, which is one of the largest Italian ski resorts (Tognetto, et al. 2021). The glacier was a central destination and was frequented both in winter and summer periods. Over time, the landscape and morphology of the glacier have totally changed, the smaller lobe has disappeared due to continuous retreat and summer skiing activities have stopped in 1997 (Maggioni, et al. 2009). Figure 6 shows the Glacier area evolution between 1999 and 2018. While Figure 7 shows the frontal retreat of the oriental lobe of the glacier starting from 1850, where this year is taken as reference value for the end of the Little Ice Age period.

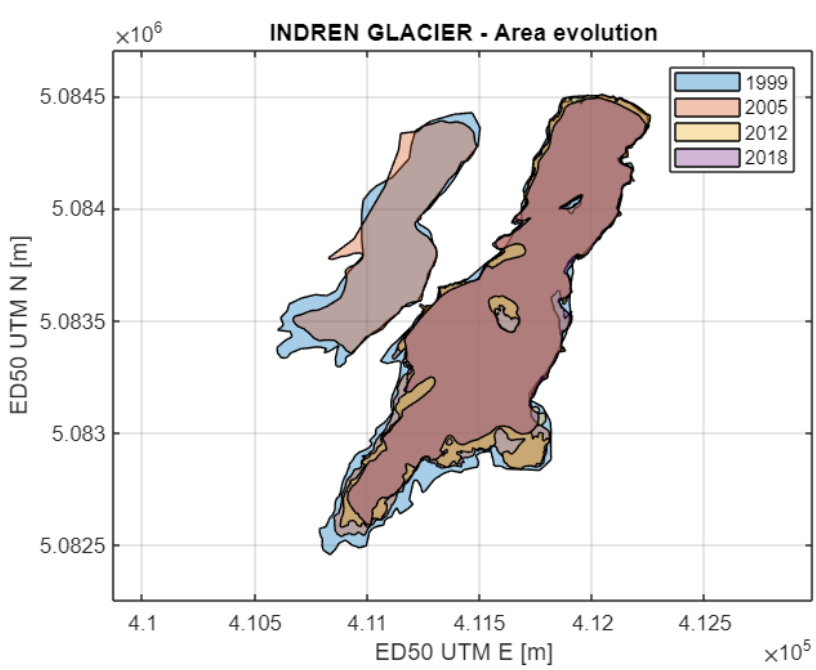

Figure 6: *Area evolution of Indren Glacier between 1999, 2005, 2012 and 2018 respectively. A consistent shrinkage of the glacier can be observed, with the complete melting of the smaller lobe between 2005 and 2012. Data for 1999, 2005 and 2012 was downloaded from Catasto dei Ghiacciai[11]. 2018 glacier's outline was reconstructed from a UAV photogrammetric flight[12].*

[11] http://catastoghiacciai.regione.vda.it/Schede/Geonavigatore/geonav.htm
[12] Courtesy of Fondazione Montagna Sicura: https://www.fondazionemontagnasicura.org/

Figure 7: *Frontal retreat of left lobe of Indren glacier starting from 1850. Processing on 2006 orthophoto*[13].

Additionally, looking at Figure 8, a significant ice loss can be observed between 1915 (Figure 8 (a)) and 2020 (Figure 8 (b)). Over this century, the intense ice melting activity has lead to the emersion of huge portions of rock.

[13] La Carovana dei Ghiacciai, Report 2020, Legambiente: https://www.legambiente.it/wp-content/uploads/2020/12/caronava-dei-ghiacciai-report-2020.pdf

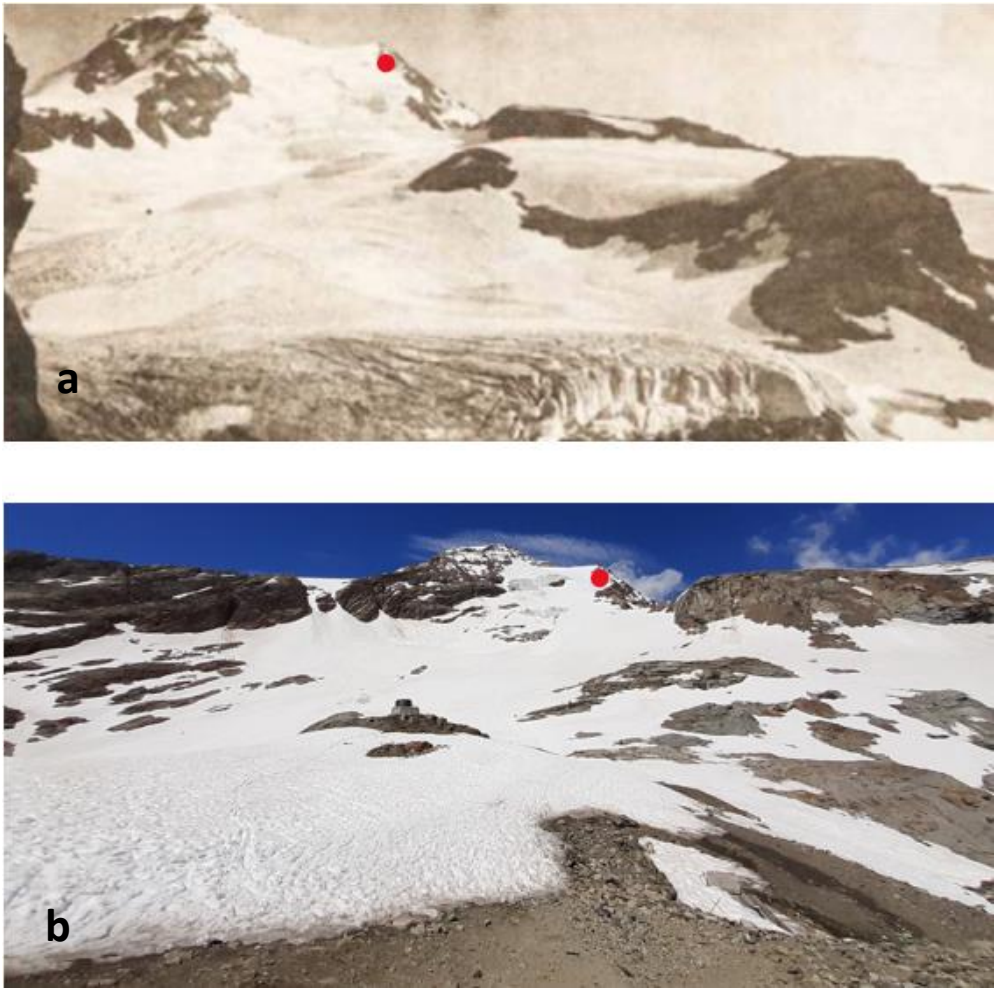

Figure 8*: Indren Glacier in (a) 1915[14] and (b) 2020[15]. The red dots are used as reference points in the two pictures*.

2.1 Historical pictures of the glacier

Some historical archives of the Indren Glacier from 1901, taken from Museo Nazionale della Montagna[16], will be shown in this section to gain an insight into the past conditions of the glacier.

[14] Ibid., https://www.legambiente.it/wp-content/uploads/2020/12/caronava-dei-ghiacciai-report-2020.pdf
[15] Courtesy of Colombero Chiara. Picture taken during the GPR survey of July 4th, 2020.
[16] https://www.museomontagna.org/

Figure 9: *Picture of Indren Glacier's mouth in August 1901.*

Figure 9 shows the glacier's mouth, from where the accumulated melted snow outflows. This represents a good indicator of the state of the glacier, as by monitoring and observing whether it is restricting or enlarging over the years, the amount of outgoing water can be estimated.

Figure 10 shows the left and right tributaries of the glacier which were present in 1901.

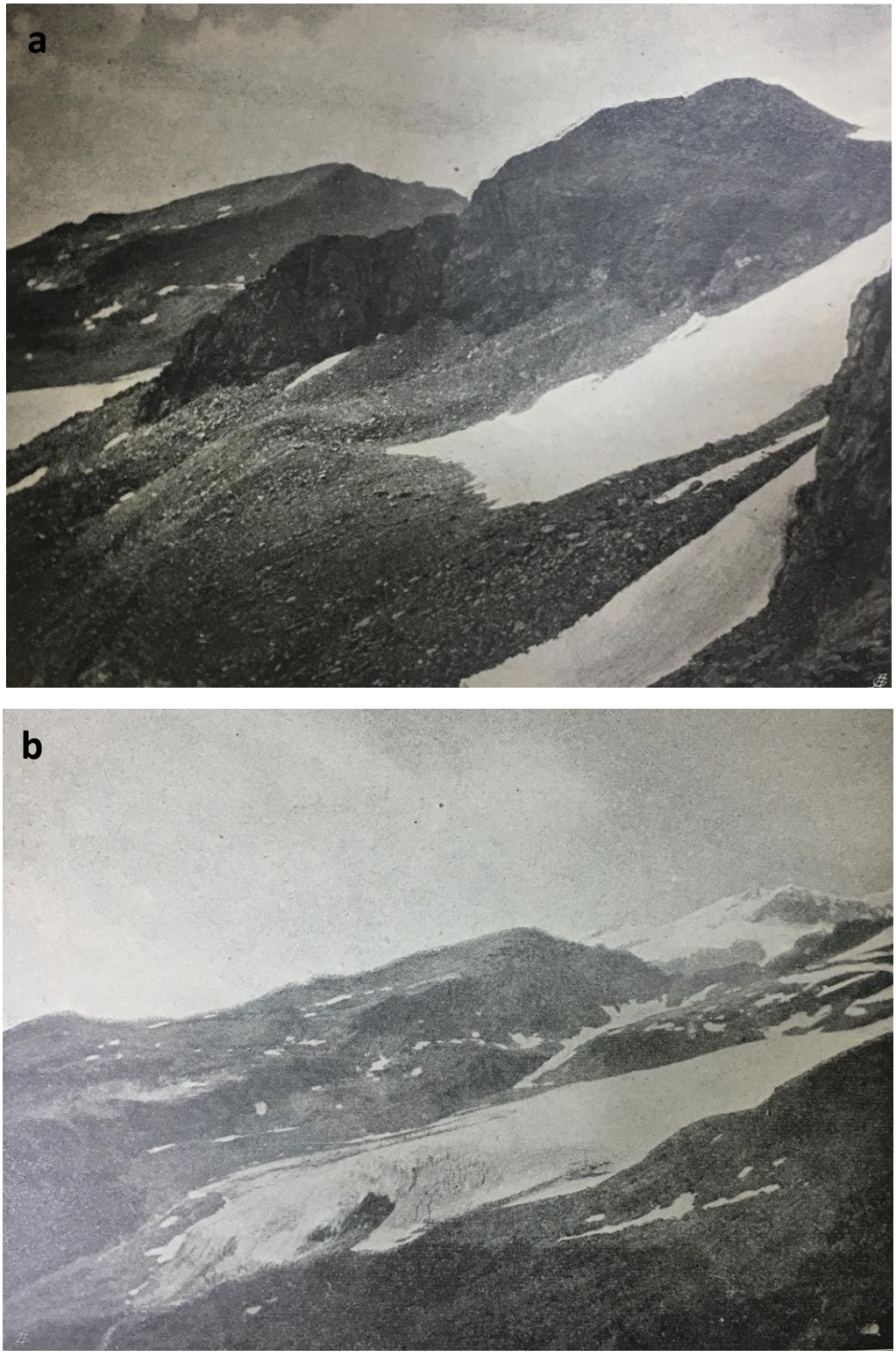

Figure 10: *Picture of Indren Glacier's left (a) and right (b) tributaries, respectively, in August 1901.*

Additionally, within the archive, two sketches defining the lithology of the area were found (Figure 11).

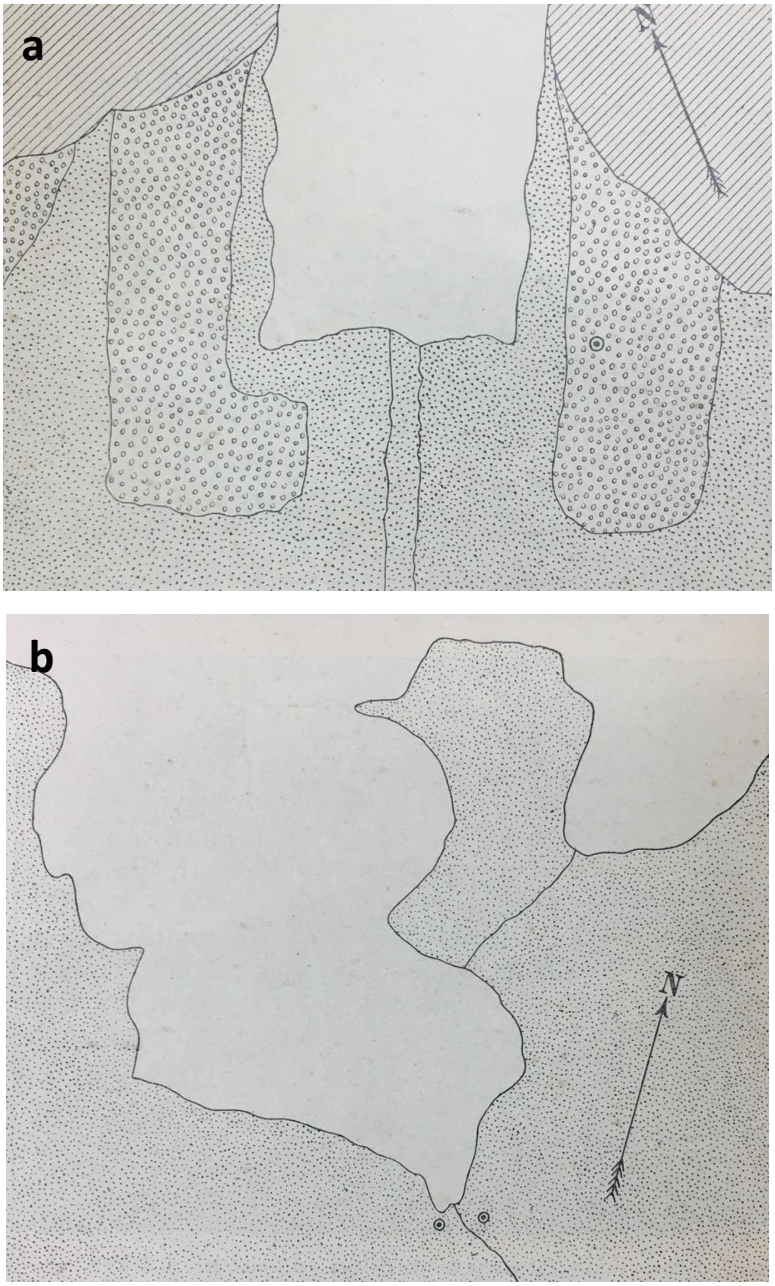

Figure 11: *Sketch showing the left (a, scale: 1:5005) and right (b, scale: 1:6250) fronts of Indren Glacier. Points indicate debris areas, circles represent the moraines, lines show rock zones.*

From Figure 11, it can be observed that there is a high amount of debris which leave the rock undercover in some areas. This could also be noticed by looking at Figure 10.

Unfortunately, there were no available pictures of the same areas of the glacier for present days, thus no comparison could be performed. However the wo lateral moraines of the left front of the glacier are still visible nowadays (Figure 12).

Figure 12: *Focus on the area below Indren Glacier (left front)[17]. The blue dashed lines show the profile of the moraines. Imagery date: October 2017.*

Comparing the ice location with respect to the moraines in Figure 12 and Figure 11 (a) a significant retreat of the front of the left lobe can be observed.

[17] Source: Google Earth.

3 Analysis of Superficial Variations

In this section the analysis of superficial variations of Indren Glacier will be addressed. For this purpose, the Digital Elevation Models (DEMs), namely, Digital Terrain Models (DTMs) of the area of interest were used. In particular, the DEM of 1999, 2008 and 2018 were considered. The distribution of elevation information over two ranges of 10 years offered a good opportunity to investigate changes occurred over a significant time interval, deriving a preliminary estimation of the ice thickness variations over time.

3.1 Available data and acquisition techniques

The 1999 and 2008 DTMs were directly downloaded from the Aosta Valley portal[18]. The technical sheet outlining the method used to obtain the datasets, was provided along with the datasets itself.

The 1999 DTM was obtained by interpolating the information contained in the elevation points and contour lines, which were directly extracted from the large-scale "Carta Tecninca Regionale Numerica"[19]. The resolution of this dataset was 100 m and its reference system was UTM-ED50, namely, the standard reference system used in the Aosta Valley.

The 2008 DTM consisted in the union of two datasets, one acquired in 2005-2006 and one in 2008. For simplicity it will be addressed to as 2008 DTM. The data acquired in 2005 had the objective to cover the zones in Aosta Valley subject to debris flow hazards together with the main fluvial areas of the territory. This dataset was characterized by a 0.5 m resolution and UTM-ED50 as reference system[20]. In 2008 the remaining part of the region, left uncovered by the 2005-2006 survey, was acquired, with a 2 m resolution and the same reference system of the other campaign[21]. Both surveys were carried out by means of a LiDAR (Light Detection and Ranging) scanner, mounted on board of an aerial platform. This type of system allowed for the collection of a point cloud, where each point was defined by its coordinates (x,y,z). The position of the point was defined by measuring the time difference between the emitted signal and the received one, considering also the intensity of the latter. From the elevation information stored in each point, it was possible to obtain the Digital Surface Model (DSM, blue line in Figure 13). This last one contained all the acquired points, also including those referred to anthropic constructions and vegetation. Through a classification procedure, from which it was possible to give a physical meaning to each point, and a consequent filtering processing, it was obtained the final DTM (red line in Figure 13).

[18] https://mappe.partout.it/pub/geonavitg/geodownload.asp?carta=DTM99
[19] https://metadati.partout.it/metadata_documents/DTM_1999.pdf
[20] ttps://metadati.partout.it/metadata_documents/DTM_2005.pdf
[21] https://metadati.partout.it/metadata_documents/DTM_2008.pdf

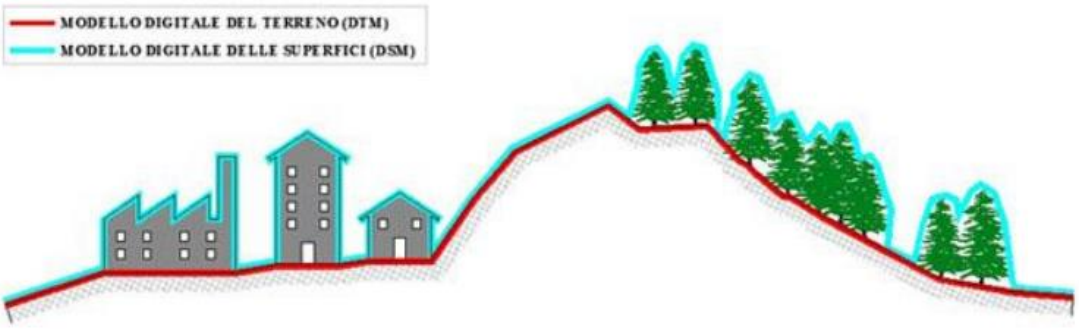

Figure 13: *Sketch showing the difference between Digital Terrain Model (red) and Digital Surface Model (blue)[22]. In the DTM, buildings and vegetation are excluded through an interpolation technique and only the terrain topography is considered.*

The 2018 DTM was obtained through the drone photogrammetric flight carried out by Fondazione Montagna Sicura on the 4th July of 2018, along with the orthophoto of the relevant area. The average resolution of the dataset was <1 m, and its reference system was WGS84. Differently form the other two datasets, which had the elevation defined in orthometric height, this DTM was characterized by an elevation expressed in ellipsoidal height.

Additionally to the DTMs, the perimeters of the glacier shown in Figure 6 were used. In particular the one of 1999, 2005 and 2018 were utilized.

3.2 Methodology

To work with the different Digital Elevation Models and perform comparison analysis, they had to be defined in the same reference system. For this purpose, QGIS was used and the datasets coordinates were all converted into WGS84 UTM32.

Secondly, the conversion of the ellipsoidal height of the 2018 DEM into orthometric height was required. Since no grid was provided for this dataset, this conversion could not be performed directly through ConveRgo, namely, the official Italian software used for coordinate and altimetric transformations. Hence, a manual elevation conversion was performed. To this aim, the computation of geodetic undulation was needed. This was estimated by taking into account both the Digital Elevation Models of 2008 and 2018. A series of control points located outside of the glacier (Figure 14) were chosen and their elevation was computed from both DEMs. Then, it was computed the average elevation difference between 2008 and 2018, obtaining a geodetic undulation of -55 m $\pm$ 2 m. The ConveRgo software was then used in a second moment to validate the obtained result. Using this tool, it was possible to compute the geodetic undulation for a random point located in the area of interest. A value of -53 m was obtained, consistently with the value found using the control points. Therefore, the amount of 55 m was subtracted from the 2018 DEM through ArcGIS Pro obtaining the orthometric height for all the points of this dataset. Despite not being the rigorous approach, the results obtained through this method can still be considered acceptable as uncertain outcomes would likely have been obtained using other approaches as well.

[22] Ibid. p. 24, DTM 2005-2008.

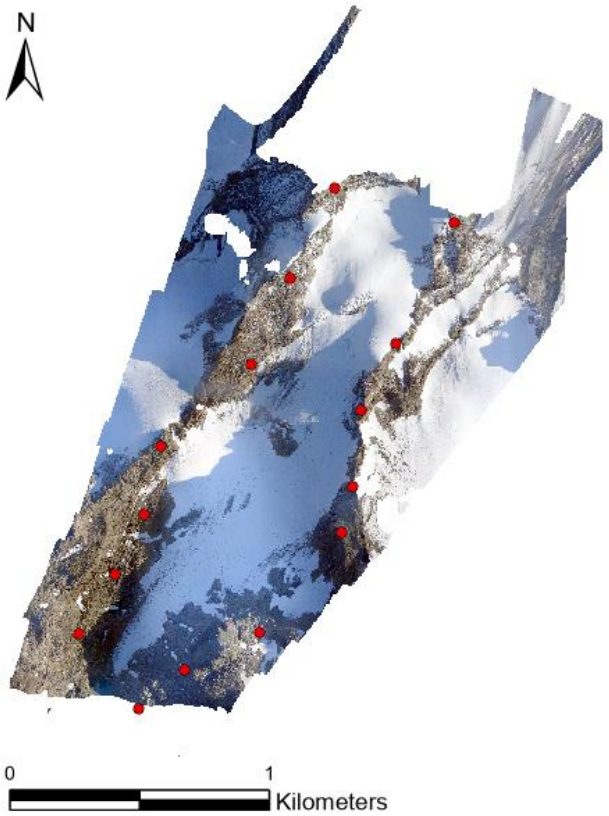

Figure 14: *Orthophoto of the Indren Glacier acquired in 2018. The red circles represent the location of the control points used for the ellipsoidal-to-orthometric height conversion. It can be noted how these were located outside the glacier area, on the rock, to be sure no significant elevation change occurred between 2008 and 2018.*

Both the previously described procedures allowed for a correct comparison of the datasets form a referenced system point of view. However, the difference in resolution of the latest datasets from the oldest one made it difficult to clearly highlight through a layer subtraction the variations that have occurred over the years. In order to improve the comparison visualization and be compliant with the earliest dataset, some smoothing proceedings were applied to the latest ones.

The 2008 layer was easily resampled over the 1999 grid with ArcGIS Pro. Nevertheless, this was not sufficient for a good data visualization, thus a low pass filter was applied to the 2008-1999 difference.

Concerning the DEM of 2018, the resample to the 1999 cell resolution could not be performed because their difference was too large and information would have been lost. Therefore the smoothing processing only included the application of a low pass filter to the 2018-1999 difference.

Detailed information on the applied processing method for smoothing the layers differences is reported in Appendix A.

3.2 Results

Figure 15 shows the three different DEMs after the reference system adjustments, cut over their respective perimeters.

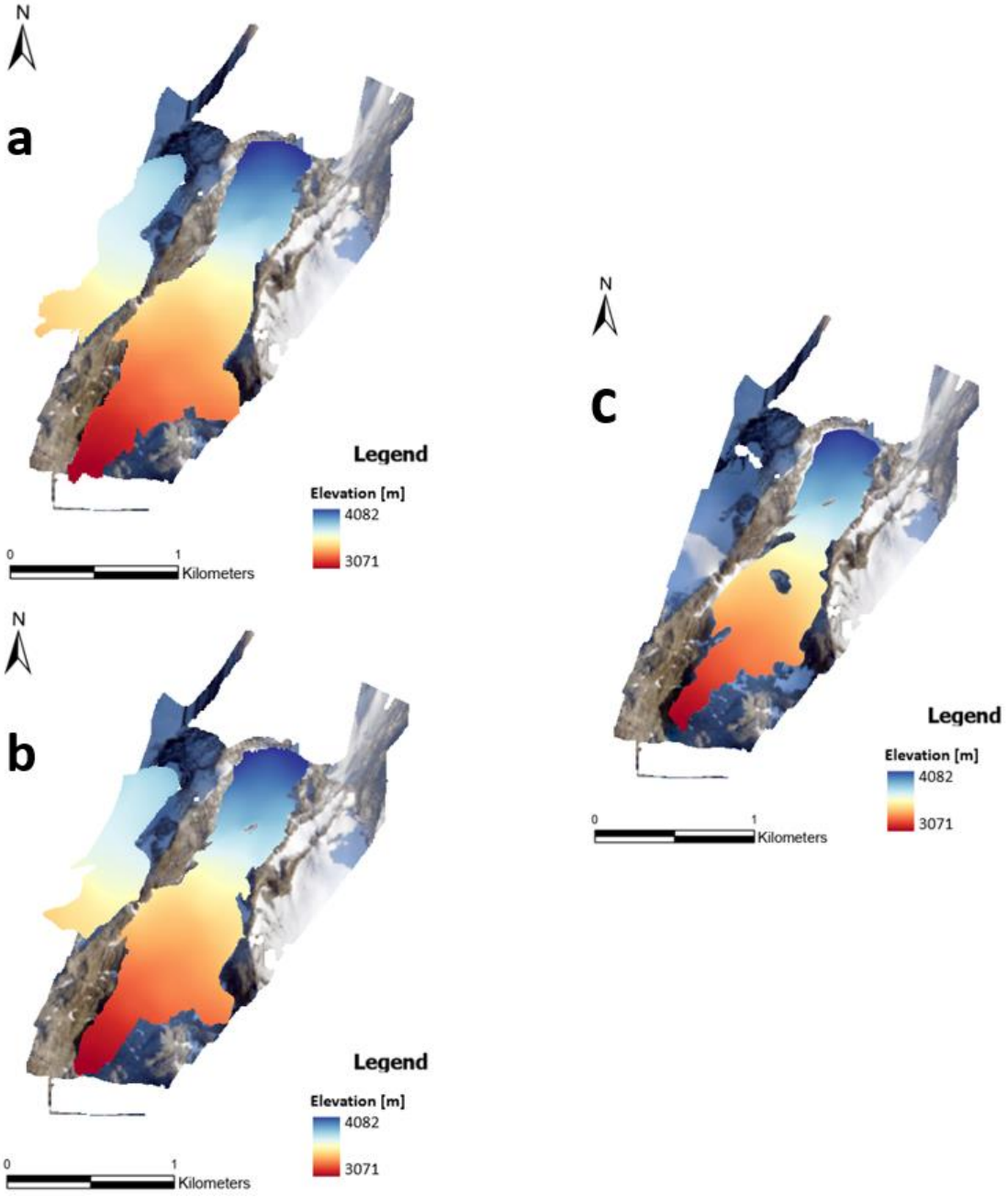

Figure 15: *Orthophoto of the Indren Glacier with the Digital Elevation Models of 1999 (a), 2008 (b) and 2018 (c), cut over their relative perimeters.*

Looking at the obtained results it can be noticed that in 2008, a hole in the glacier appeared at the highest elevations. Ten years later, in 2018, a second hole appeared at mid-elevations and the smaller lobe of the glacier disappeared.

Figure 16 instead displays the subtractions between the different DEMs after the smoothing procedure. Notice that the differences were obtained by subtracting the earliest years to the latest ones in order to visualize the positive values of the color scale as increase in elevation.

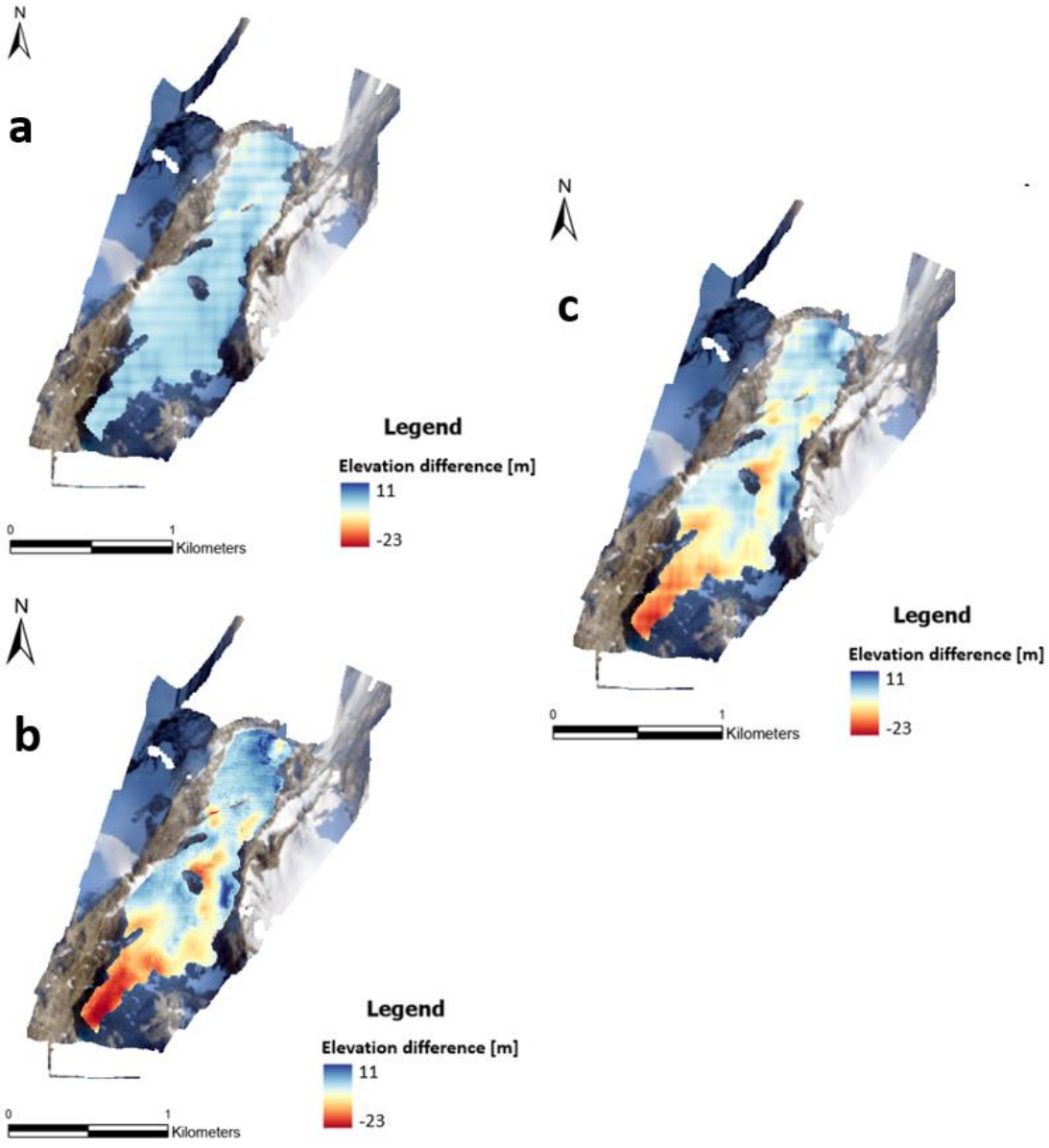

Figure 16: *Digital Elevation Models differences between : (a) 1999 and 2008 ; (b) 2008 and 2018; (c) 1999 and 2018.*

In this case the different datasets were all cut over the perimeter of Indren Glacier observed in 2018, in order to better visualize the changes occurred in the remaining present portions of the glacier.

The color scale of Figure 16 was standardized for all three layers by considering the minimum and maximum values observed across the three cases. This standardization aimed emphasizing the extent of the fluctuations. However, the chosen color scale was too broad to accurately visualize the changes in elevation for the difference between 1999 and 2008. Figure 17 shows the subtraction of these two layers using the original color scale.

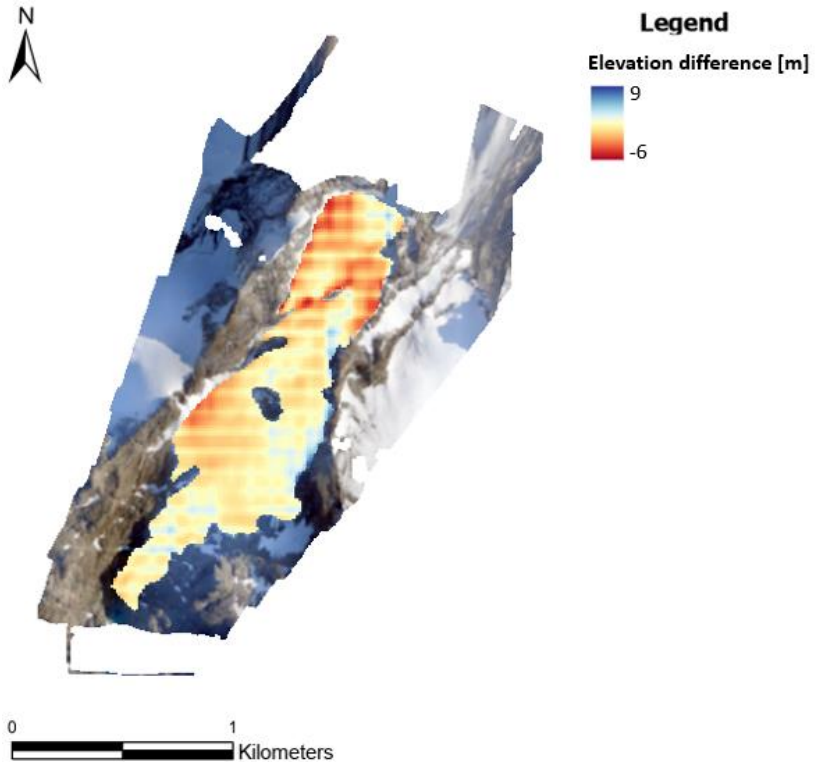

Figure 17: *Digital Elevation Model difference between 1999 and 2008 with the original range of elevation.*

4 Analysis of Internal Variations

In this section the different investigation methods used to retrieve information regarding the Indren Glacier thickness and its dependance to climate forcings, as well as other factors, will be addressed.

First, the GPR system and equipment, as well as the data processing will be described. Secondly the GlaTE model and its constraints will be discussed. Finally, the Minimal Glacier Model and its basic equations, together with its assumptions will be addressed.

4.1 Methodology

4.1.1 GPR

During the last decades, Ground Penetrating Radar techniques have assumed more relevance in the context of glacier studies because of the ability of electromagnetic waves to penetrate deeply into the ice layer without being invasive. These types of systems were already commercially available from 1970 but they have gained interest for geophysical and other applications only in the recent years (Navarro and Eisen 2009) because of the introduction of real time and continuous digitalization, which made their utilization more straightforward.

4.1.1.1 Working principle

The Ground Penetrating Radar instrument is composed by a transmitter and a receiver antenna, generally contained in the same case. The instrument is moved by an operator along a survey line (Figure 18) and sends an electromagnetic pulse into the subsurface through the transmitter. When the signal encounters a discontinuity into the subsoil (e.g. a material with different electromagnetic properties), it is reflected back to the surface, where it is collected by the receiver. The antenna frequency of these types of instruments ranges between 10 MHz, typical for glaciological investigations at great depth, and 2.5 GHz, typical for non-destructive material tests at high resolution (Godio and Colombero 2020-2021).

Figure 18: *Picture representing the Ground Penetrating Radar survey conducted on Indren Glacier in July 2020. The white box is the GPR instrument which is dragged over the ground surface by the first operator. The second technician carries the acquisition unit and visualizes the acquired data in real time.* (Godio and Colombero 2020-2021).

Figure 19 shows the general working principle of the instrument: the radiated energy propagates by means of a cone of radiation and when it encounters a target, it is able to retrieve its distance from the antenna by measuring the two-way travel time (twt), namely, the time required from the signal to be emitted by the transmitter and recorded at the receiver.

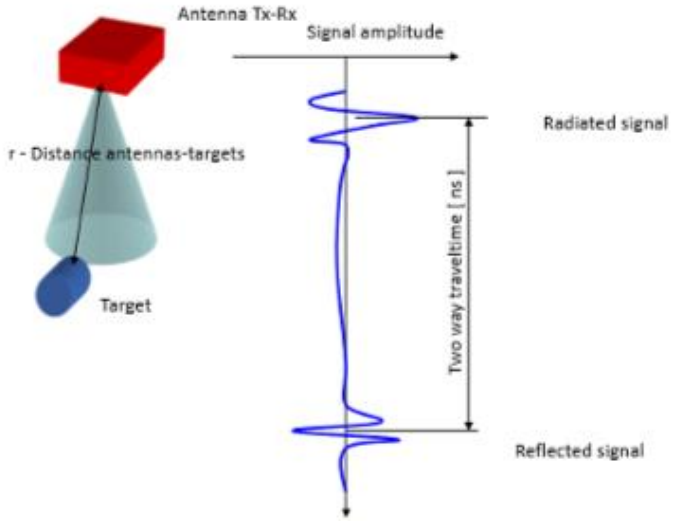

Figure 19: *On the left: GPR antenna-target arrangement with the typical cone of radiation distribution. On the right: amplitude of radiated and reflected signal* (Godio and Colombero 2020-2021).

Additionally to the transmitter/receiver antennas, the system is composed by a Control Unit (CU), which has the task of sending the signal and collect/record the reflected one. The CU gathers all the signals and, after averaging them together, stores them, typically at a rate of 50 echoes per second (Godio and Colombero 2020-2021). This stacking procedure has the objective to reduce the noise of the signal. In this manner, it is possible to enhance the amplitude of the trace, which is the non-random signal, and diminish the random signal (i.e., the noise).

The final stacked signal represent the radar trace, by arranging each radar trace side by side it is possible to retrieve the radargram.

The central unit is generally controlled by an internal CPU or an external computer. The system equipment also includes cables for the connection between the antennas and the CU, and a GPS unit for the georeferentiation of the antenna.

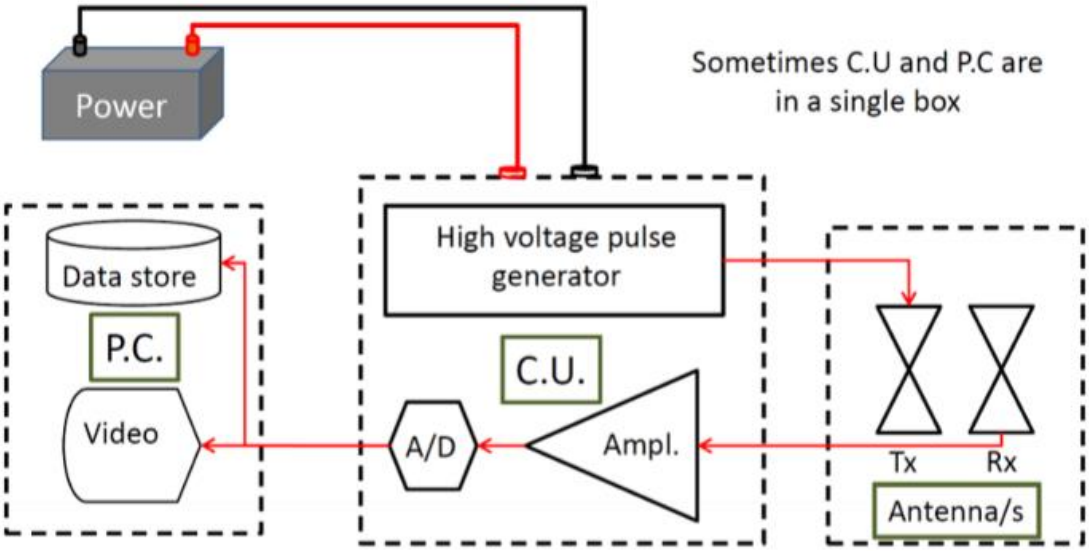

Figure 20: *Block diagram of a GPR system equipment* (Godio and Colombero 2020-2021).

Figure 20 shows the block diagram of the GPR system. The instrument is connected to a power source, coupled to an high voltage pulse generator, which operates in a range of 40-100 V. Commercial GPR systems cannot work with a voltage higher than 100 V because of safety restrictions. The high voltage pulse is sent to the transmitter antenna (Tx) and the reflected signal is collected by the receiver antenna (Rx). Then the signal is sent first to an amplifier and then to an analog to digital converter (A/D) in order to store the data in a magnetic memory inside the PC unit. Then, the data can be either stored or displayed in a video.

4.1.1.2 Application to Indren glacier case

As already mentioned, GPR techniques are particularly useful for the application to glacial environments. This is due to mainly two reasons. The first one depends on the typical glacier configuration, which can be approximated to a two layer system (Figure 21), with an ice layer sitting above the bedrock.

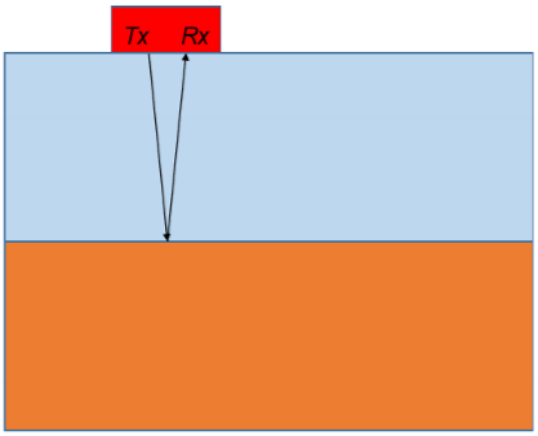

Figure 21: *Schematization of GPR working principle in simple system composed by two parallel layers with different electromagnetic properties* (Godio and Colombero 2020-2021).

Within this simple model, the depth of the ice layer can be easily retrieved considering the twt of the signal measured by the instrument:

$$z = \frac{twt\ v}{2} \tag{1}$$

Where v is the typical velocity of the media through which the signal is travelling, which depends on the light speed ($c = 3 * 10^8\ m/s$) and on the relative electrical permittivity of the material (ε_r(-)), following:

$$v = \frac{c}{\sqrt{\varepsilon}} \tag{2}$$

For pure ice v=0.17 m/ns ($\varepsilon_r = 3$). This simple formulation assumes that the first medium is homogeneous and the electromagnetic wave velocity remains constant along the material. However, the presence of water droplets and debris inside the ice matrix causes a velocity variation that is generally neglected during the time-to-depth conversion (Equation 1). In addition, the presence of these heterogeneities is strongly affecting the attenuation of the electromagnetic signal.

The second reason why the GPR technology is well suited for ice thickness estimations, lies indeed in the electromagnetic properties of the media constituting these environments. As a matter of fact, ice is an almost non-conductive material (Table 1), transparent to the penetration of the radar signal. This permits the GPR signals to undisturbedly travel in the first layer, with very limited attenuation and be reflected back, when encountering the second layer. This property allows the electromagnetic signals to reach considerable depths of investigation, as in favorable conditions, hundreds of meters of penetration depths can be reached (Forte, et al. 2021).

Table 1: *Permittivity (ε_r), conductivity (σ), velocity (v) and attenuation coefficient (α) values for different materials* (Annan 2005)*. Notice the small value of ice conductivity, which also affects the attenuation coefficient.*

Material	ε_r	σ (mS/m)	v (m/ns)	α (dB/m)
Air	1	0	0.30	0
Distilled water	80	0.01	0.033	2 × 10-3
Fresh water	80	0.5	0.033	0.1
Sea water	80	3000	.01	103
Dry sand	3–5	0.01	0.15	0.01
Saturated sand	20–30	1–10	0.06	0.03–0.3
Limestone	4–8	0.5–2	0.12	0.4–1
Shales	5–15	1–100	0.09	1–100
Silts	5–30	1–100	0.07	1–100
Clays	5–40	2–1000	0.06	1–300
Granite	4–6	0.01–1	0.13	0.01–1
Dry salt	5–6	0.01–1	0.13	0.01–1
Ice	3–4	0.01	0.16	0.01

For this study, two GPR datasets coming from two survey campaigns conducted on Indren Glacier on different days of July 2020 were used. The first dataset consisted of 12 lines acquired with a 200-MHz IDS antenna and a vertical resolution (Δz) of 0.2 m. This last parameter was retrieved as follows:

$$\Delta z = \frac{\lambda}{4} \tag{3}$$

With λ (m) being the antenna wavelength, dependent on the frequency, f (Hz), and the velocity of the ice layer:

$$\lambda = \frac{v}{f} \tag{4}$$

The second survey campaign was carried out with a 70-MHz IDS antenna and a lower vertical resolution of 0.6 m, three times coarser than the previous case. The quality of this second dataset was very poor, probably because of the low resolution and of issues encountered during the acquisition phase. This made it particularly hard to retrieve useful information and only three of the seven available lines could be utilized for this analysis.

The arrangement of the considered GPR profiles is represented in Figure 22.

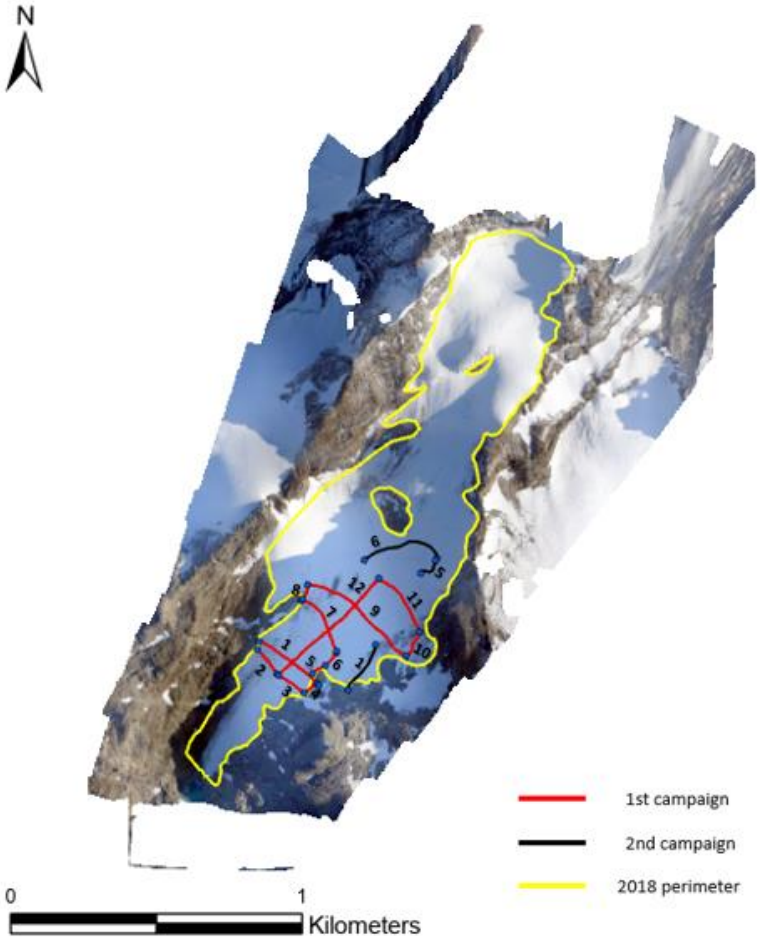

Figure 22: *Orthophoto of Indren Glacier with the GPR profiles acquired over the two campaign surveys, with their relative identifying number. The figure only displays the lines that were considered in this thesis (i.e., all the profiles acquired on the first survey campaign and line 1, 5 and 6 of the second survey campaign).*

4.1.1.3 Data processing

The raw GPR data was a set of ASCII files which were imported and visualized with the ReflexW software. This tool allowed to directly picture the time-depth conversion on the radargram (considering a constant velocity in Equation 1). Additionally, this software was used to process the data in order to enhance the signal to noise ratio. Two separate, yet identical, processing flows were executed, one for the first dataset and the other for the second one. In this section, the procedure used to clear the signal will be explained using an example line (line 9 from the first campaign).

The original signal of profile 9 is shown in Figure 23.

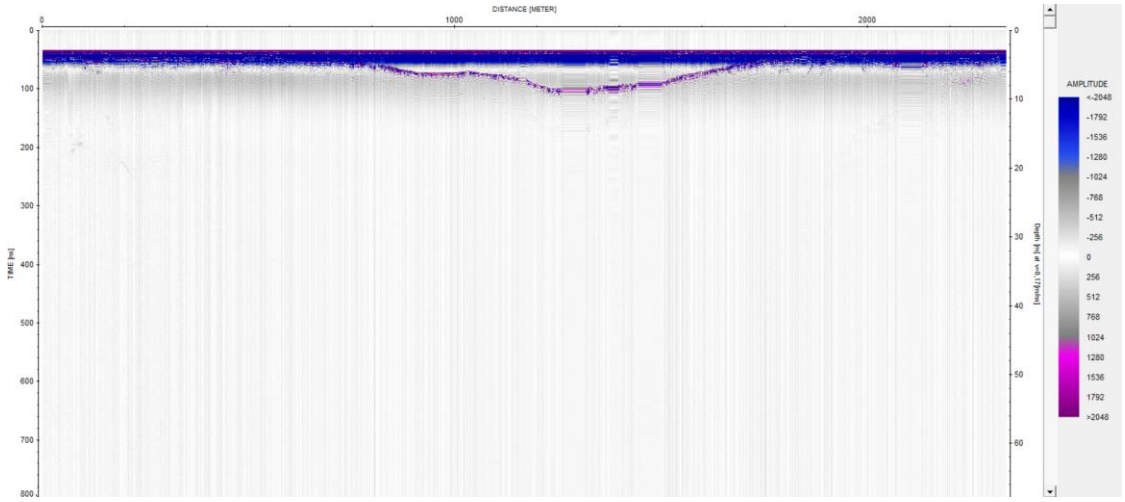

Figure 23: *Raw GPR data of an example line (profile 9 of first survey campaign).*

The processing flow, included the following steps:

1. Move start time: this first procedure allowed to remove the delays in the signal occurred during the acquisition phase. This was accomplished by removing the part of the radargram before the time zero (Figure 24).

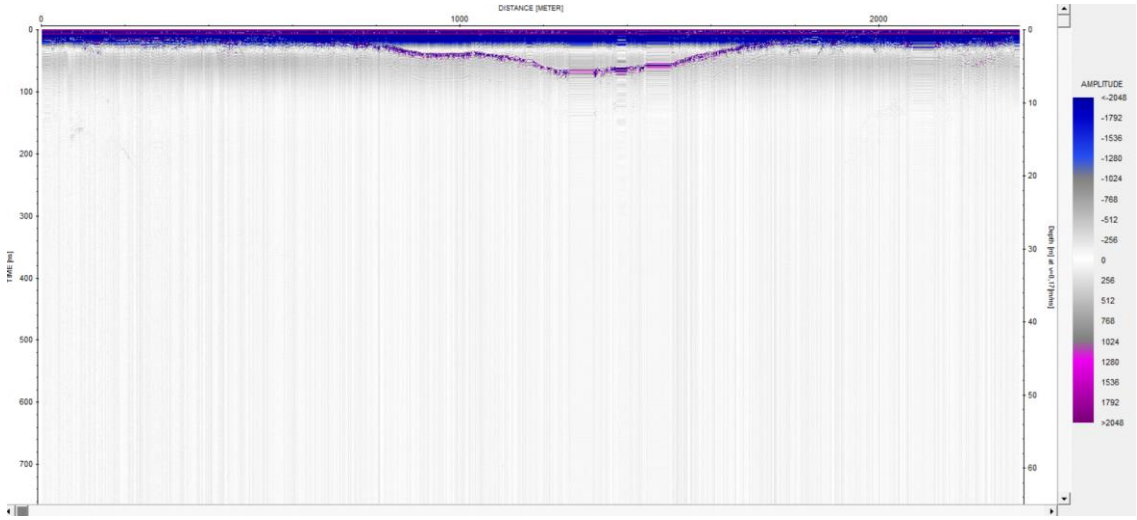

Figure 24: *Radargram of line 9 after the "Move start time" processing step.*

2. Dewow: this represents a high pass filter that was used in order to remove the continuous low frequencies in all traces. Through this setting a mean value was calculated for each trace and it was then subtracted from the central point (Figure 25).

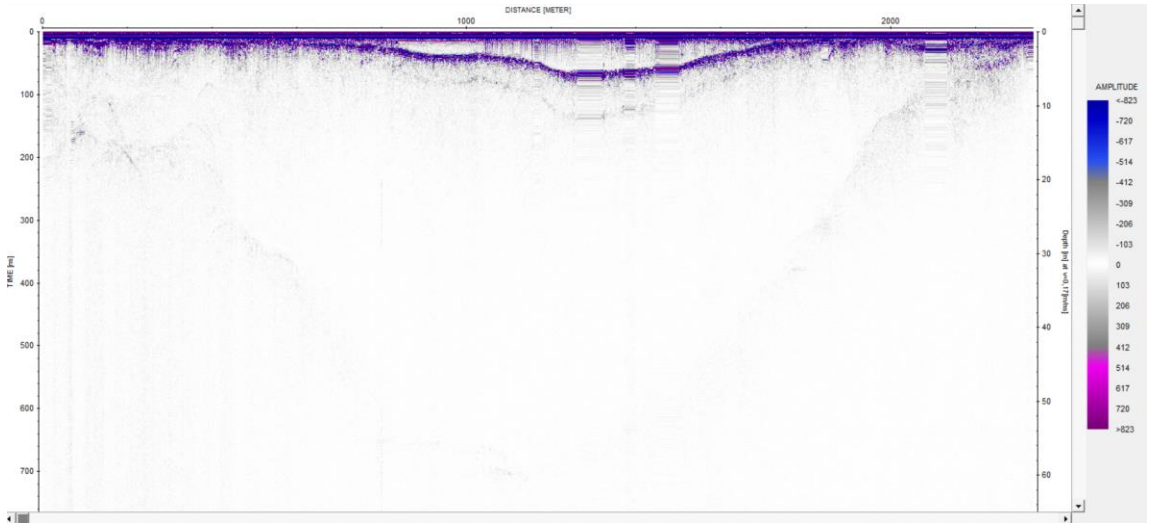

Figure 25: *Radargram of line 9 after "Dewow" processing step.*

3. Background removal: This step was applied to the processing flow because GPR data often present a clutter which can be recognized as horizontal stripes. The presence of this effect can be due to GPR system noise, ground bounce, scattering due to uneven soil and reflections from external anomalies (Sandmeier Geophysical Research - Introduction to the processing of GPR-data within REFLEXW). With background removal it was possible to subtract the average value of all the radargrams to the single traces, removing the constant events from the radargram. The result is shown in Figure 26.

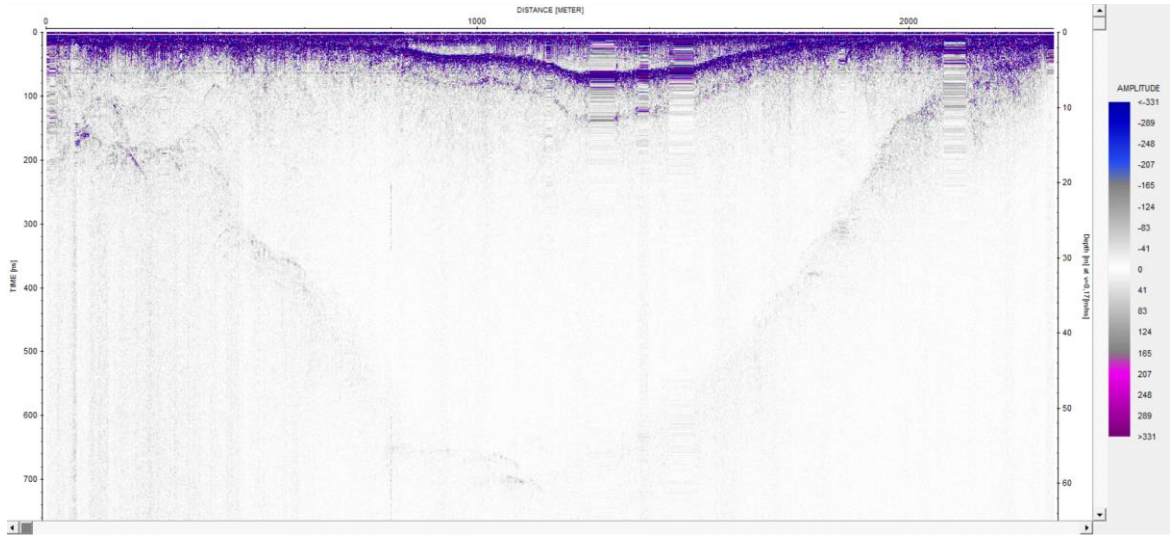

Figure 26: *Radargram of line 9 after "Background removal" processing step.*

4. Divergence compensation: This step was performed because generally the signal is attenuated with increasing depth due to geometrical spreading. By the application of this gain to the radargram, it was possible to recover the signal also at higher depths (Figure 27).

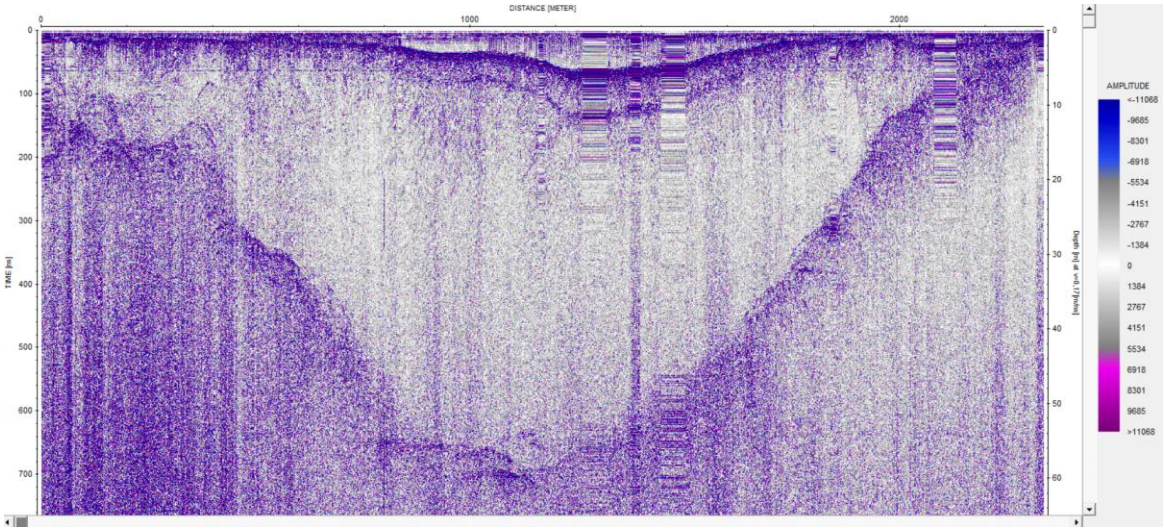

Figure 27: *Radargram of line 9 after "Divergence compensation" processing step.*

5. Stationary traces removal: This step was applied to the traces in order to remove the continuous horizontal stripes present in the radargrams, which could lead to an incorrect depth localization. These stationary traces were the effect of the acquisition phase, and were caused by the continuous recording of the instrument, even when it was not moving. Figure 28 shows the radargram after the stationary traces removal.

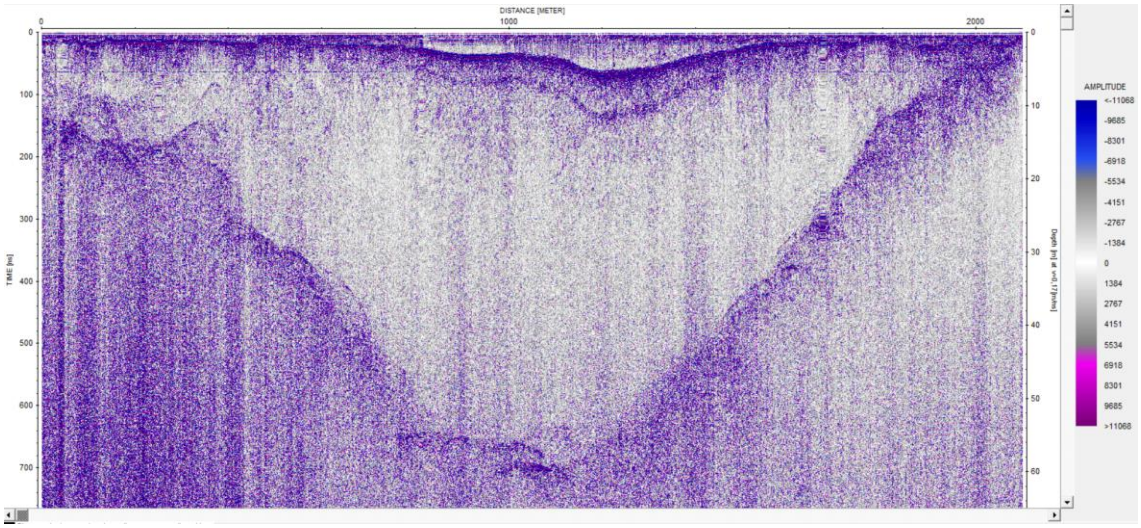

Figure 28: *Radargram of line 9 after "Stationary traces removal" processing step.*

6. Length adjustment: This final step was required because the automatic computation of the radargram length was linear from the first trace position and did not match with the real length of the acquired section. In order to solve this problem a manual length adjustment was performed (Figure 29).

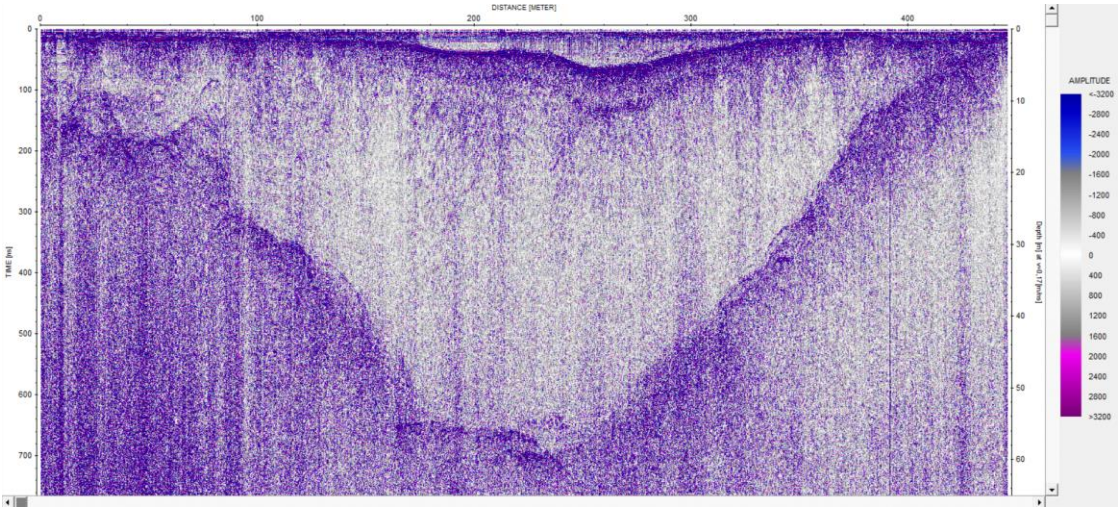

Figure 29: *Radargram of line 9 after "Length adjustment" processing step.*

4.1.2 Spatial Modeling: GlaTE

Over the past years, some glacial models have been developed in order to estimate the ice thickness of a glacier starting from observable surface parameters, such as the slope. In the last years new models considering also mass conservation constraints as well as basal shear stress parameters have appeared in literature. However these models are always based on some simplifications which can lead to significant uncertainties in the results.

The Glacier Thickness Estimation Algorithm, developed by Langhammer et al. (2019), allows to constrain a glaciological model with the ice thickness estimated by means of GPR surveys and obtain the overall thickness distribution through an inversion procedure. This ensures a higher degree of accuracy in the obtained results.

In addition to the GPR limits, this model incorporates a set of other constraints that are integrated with the GPR one to form a cohesive system of equations. The main constraining factors and the relative formulas taken into account by the authors of this model will be briefly described in the next paragraph, closely following the procedure explained by Langhammer et al. (2019).

4.1.2.1 GPR data constraint

The constraint related to the GPR data is expressed according to the following equation:

$$Gh^{est} = h^{GPR} \tag{5}$$

Where:

(i) G is a $N^{GPR} x M$ matrix, with ones on the main diagonal and zeros outside;
(ii) N^{GPR} is the number of available GPR data points;
(iii) M is the location of the points defined over a regular grid, R;
(iv) h^{est} is a vector containing the ice thickness at all the M locations, also including the ice thickness estimation for the unknown points.
(v) h^{GPR} is a vector containing the ice thickness of GPR data (i.e., known points).

In order to have the GPR data falling inside the cells of the regular grid, the algorithm is able to obtain h^{GPR} by interpolating/extrapolating the radar data to the nearest grid points of R.

4.1.2.2 Glaciological model constraint

The second constraint is related to the glaciological model. For this purpose the authors adopted the approach followed by Clarke et al.(2013), linking the basal shear stress of the glacier to the ice thickness and the surface slope. To this end, the DEM of the area and the mask defining the outline of the glacier are required. The glacier's mask consists in a matrix, with the same size of the DEM, containing ones where ice cover is present and zeroes elsewhere.

To implement this second constraint, the algorithm first has to subdivide the glacier into flow sheds, which are "glacier flow units defined by their ice catchment" (Clarke, et al. 2013). This task can be accomplished by means of the Matlab TOPO-Toolbox. Once the flow sheds are defined, considering the ice volume conservation principle, the following apparent mass balance is applied to each of them:

$$\tilde{b} = \dot{b} - \frac{\partial h}{\partial t} \tag{6}$$

Here, $\dot{b}$ is the ice equivalent mass balance rate ($m\ yr^{-1}$) and $\frac{\partial h}{\partial t}$ is the rate of change of ice thickness ($m\ yr^{-1}$).

The flow sheds are then subdivided into a preselected number of elevation zones D_i and for each of them it is computed the ice discharge $Q_i (m^3 yr^{-1})$ through their lower boundary according to the formula below:

$$Q_i = \int_{\Omega_{D_i}} \tilde{b} \tag{7}$$

Where Ω_{D_i} is the area of the zone D_i.

Then, from the above formulation, according to Clarke et al. (2013), the basal shear stress can be expressed as follows:

$$\tau = \left[\frac{(n\ +\ 2)\rho g \sin(\varphi)^2\ \xi\ q}{2A} \right]^{\frac{1}{n+2}} \tag{8}$$

Where:

(i) n represents the exponent of the Glen's flow law for ice ;
(ii) ρ corresponds to the ice density;
(iii) g is the gravitational acceleration;

(iv) A is the creep rate factor. This parameter is taken from literature, but its value can vary different orders of magnitude;
(v) φ is the surface slope averaged along the lower boundary of D_i;
(vi) ξ is the creeping contribution relative to the basal sliding to the ice flux and varies between 0 and 1. The value of this parameter is not always correctly selected;
(vii) q is the specific ice discharge: $q = \overline{Q_i}/l_i$, with $\overline{Q_i}$, average of Q_i within D_i and l_i, length of the lower boundary of D_i.

Finally, averaging the basal shear stress in the longitudinal direction, τ^* is obtained and from it, it is possible to retrieve the glacial model ice thickness:

$$\hat{h}^{glac} = \frac{\tau^*}{\rho g \, sin(\varphi)} \tag{9}$$

The expression of τ involves a number of parameter that may exhibit significant levels of uncertainties, consequently the final value of $\hat{h}^{\mathrm{glac}}$ can have large ambiguities being subject to large overestimations or underestimations. For this purpose, the authors of the GlaTE model, have introduced a new parameter, α_{GPR}, in order to take into account this effect:

$$h^{glac} = \alpha_{GPR}\hat{h}^{\mathrm{glac}} \tag{10}$$

Where α_{GPR} can be computed by means of a tuning procedure, by minimizing the following difference:

$$\left\| h_{GPR} - \alpha_{GPR}\hat{h}^{glac} \right\|^2 \tag{11}$$

However, since differences between the ice thickness coming from the GPR data and the one estimated with the glaciological model can still be present, instead of working directly with h^{glac}, the authors have preferred to work with its spatial gradient. Finally the expression of the glaciological constraint is:

$$Lh^{est} = \nabla h^{glac} \tag{12}$$

Where L is a difference operator of dimension MxM.

4.1.2.3 Glacier boundaries constraint

The third constraint of the algorithm pertains to the glacier boundaries. It's expression is reported here:

$$Bh^{est} = 0 \tag{13}$$

Where B is a MxM matrix with ones in appropriate places on the main diagonal and zeros elsewhere.

4.1.2.4 Smoothing constraint

The last constraint concerns the smoothing of the model and is expressed as:

$$Sh^{est} = 0 \tag{14}$$

Where S is a MxM smoothing matrix .

This step is necessary as the aforementioned equations may result in multiple reasonable solutions. The smoothing constraint applies the principle of Occam's razor, which favors the simplest solution, in this case, the smoothest one, as the most likely correct one.

4.1.2.5 Final model and weighting factors

Finally, all the constraints can be solved into one single matrix:

$$\begin{pmatrix} \lambda_1 \mathbf{G} \\ \lambda_2 \mathbf{L} \\ \lambda_3 \mathbf{B} \\ \lambda_4 \mathbf{S} \end{pmatrix} \boldsymbol{h}^{\text{est}} = \begin{pmatrix} \lambda_1 \boldsymbol{h}^{\text{GPR}} \\ \lambda_2 \nabla \boldsymbol{h}^{\text{glac}} \\ 0 \\ 0 \end{pmatrix} \tag{15}$$

Where $\lambda_1, \lambda_2, \lambda_3, \lambda_4$ are weighting coefficients which depend on the confidence on all the individual contributions. For this purpose, different considerations were made by the authors. To λ_3 is generally given a fixed value (e.g., 1). While λ_1, λ_2 and λ_4 are obtained through an iterative method to make the system of equations solvable.

First, λ_1 is set equal to 1, while a small value is assigned to λ_2, leading to a high λ_1 / λ_2 ratio. This expresses a high confidence in the GPR data and a lower confidence in the estimated ice thickness with the glaciological model. Additionally, a large value is assigned to λ_4 for an over-smoothened ice thickness. Then, a first GlaTE inversion is performed with these parameters. Consequently the value for λ_4 is gradually reduced until when a predefined percentage of h^{est} matches h^{GPR} within its accuracy limits ($\pm\varepsilon^{GPR}$) or until when the following condition is met:

$$\lambda_4 = \lambda_{4_{min}} \tag{16}$$

Where $\lambda_{4_{min}}$ is a predefined lower threshold for the weighting factor. In this way, the new smoothing coefficient, $\overline{\lambda_4}$, is found, where its value is expected to be high because of the high λ_1 / λ_2.

Consequently, in order to increase the importance of the glaciological model constraint, the λ_1 / λ_2 ratio is decreased and the aforementioned steps are repeated again in an iterative process. The final weighting factors values are obtained when $\overline{\lambda_4} = \lambda_{4_{min}}$ without reaching the prescribed data match or when the λ_1 / λ_2 has reached a predefined lower limit.

4.1.2.6 Application to Indren Glacier

In order to apply the GlaTE model to the Indren Glacier case, three input datasets were required: i) GPR data, ii) DEM of the area of interest and iii) mask of the glacier's perimeter.

For this purpose, the processed GPR data represented in Figure 22 were used. Concerning the DEM, the one acquired in 2018 and described in Section 3.1 (Available data and acquisition techniques), was resampled to a cell size of 5x5 m. This step was necessary because the DTM's original high resolution would have taken too long time for the model to process it. Finally, for the glacier's mask, the 2018 perimeter, shown in Figure 6, was used and processed in order to meet the model's demands.

The algorithm was run for three different situations, changing the parameter defining the interpolation smoothness. Through this parameter, the resolution of the DEM (5 m) was multiplied by a specific value. In particular, three different amounts were considered, 5, 10, 20. This enabled the generation of results with varying resolutions:

(i) 25 m of resolution: 5 m x 5;
(ii) 50 m of resolution: 5 m x10;
(iii) 100 m of resolution: 5 m x 20.

4.1.3 Temporal Modelling: Minimal Glacier Model

A variety of glaciological models exist within the literature. An analysis of the Indren Glacier from a spatial perspective has already been conducted with the GlaTE algorithm, for static characterization in the present-day conditions. However, in order to gain a more comprehensive understanding of the glacier evolution over time, it has been decided to additionally perform an analysis from a temporal perspective.

Starting from 1900 a series of attempts to model glaciological environments and their interaction with climate were made. Over time the complexity of the developed models, either used to describe individual glaciers or national networks of glaciers, has increased. However, complex numerical models may often be inadequate in describing the glacier's evolution because of the dependence of their solutions to the resolution of the computational mesh grid. The Minimal Glacier Model, developed in 2011 by Oerlemans, was chosen for this task as it is well-suited for temporal analysis and is simpler to use than the previous methods employed in the spatial analysis of Indren Glacier.

As a matter of fact, this model has no spatial resolution. Therefore, the glacier's quantity do not vary in space but only in time. Although, this approach is much simpler compared to others found in literature, it still represents a good way for analyzing the basic relationships between glacier's modifications and temperature trends.

Moreover, the Minimal Glacier Model is composed by a limited number of parameters and this gives the possibility to better understand each of them individually, leading to a direct connection between the glacier dynamics and climate change when limited information are available. Finally, this model has the advantage of allowing a straightforward calibration by means of historical data.

This model is based on an instantaneous relationship between the glacier's length and depth and it assumes an uniform glacier width, a constant slope, a constant density and a constant mass balance gradient along the glacier. Furthermore, the ice thickness is assumed uniform and equal to the mean ice thickness $H(t)$, which changes with time.

Finally, this model assumes that larger glaciers have greater ice thicknesses, while smaller glaciers have shallower depths. This assumption is based on the idea that the ice behaves like a plastic material (perfect plasticity assumption), meaning that the amount of stress on the bottom of the glacier is limited and cannot exceed a certain point. This relationship between the glacier's thickness and its horizontal dimension allows for predictions to be made about the glacier thickness based on its size.

In order to estimate the evolution of the glacier, this model is based on the integration of the continuity equation over the entire glacier:

$$\frac{dV}{dt} = \int \dot{b}\, dx\, dy + C \tag{17}$$

Where V is the ice volume, t is time, $\dot{b}$ is the balance rate, x and y are the horizontal coordinates and C represents the mass changes at the front of the glacier.

The balance rate "is defined as the net annual gain or loss of mass at the glacier surface" (Oerlemans 2008) and has a directly proportional relationship with altitude. As altitude increases, so does the balance rate, due to the decrease in air temperature, which causes a reduction in turbulent heat transfer to the surface and in downward longwave radiation from the atmosphere. This results in increased precipitation, further contributing to the higher balance rate at higher elevations.

According to the balance rate, the glacier can be subdivided into two zones: the accumulation and the ablation zones. The accumulation zone is where generally no runoff of snow occurs during the summer period and $\dot{b} > 0$. This zone corresponds to the highest part of the glacier. The ablation zone, located at lower altitudes, is where the snow accumulated during winter melts in late spring and summer. Here, the balance rate is negative (i.e., $\dot{b} < 0$). These two zones are separated by means of the equilibrium line, for which $\dot{b} = 0$. For the steady flow state condition, ice must flow downward from the accumulation to the ablation zone, causing a movement in the equilibrium line altitude (ELA). When the climate shows a temperature increase, the ELA moves upwards, leading to a reduction of the accumulation zone and an increase of the ablation zone. The consequence is a negative mass balance and glacier shrinkage (Figure 30). For the Alps case, the ELA can vary within a range of few hundred meters depending on temperature, precipitation and aspect (Haeberli, Oerlemans and Zemp 2019).

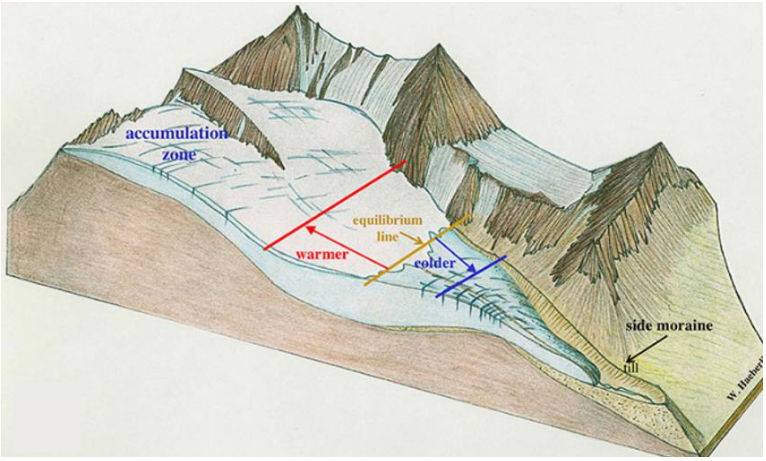

Figure 30: *Sketch of a typical mountain glacier representing shifts in ELA with varying climatic conditions* (Haeberli, Oerlemans and Zemp 2019).

The balance gradient defines the change in balance rate per unit of elevation rate:

$$\beta = \frac{d\dot{b}}{dz} \tag{18}$$

Where z is the altitude and β ranges between 0.003 and 0.01 $m\,w.e.\ a^{-1}m^{-1}$ (Oerlemans 2008) and it can be utilized to estimate the rate of mass gain or loss in the glacier to understand its response to changing climate. For this model β is considered to be constant.

The simple geometry of the model is represented in Figure 31:

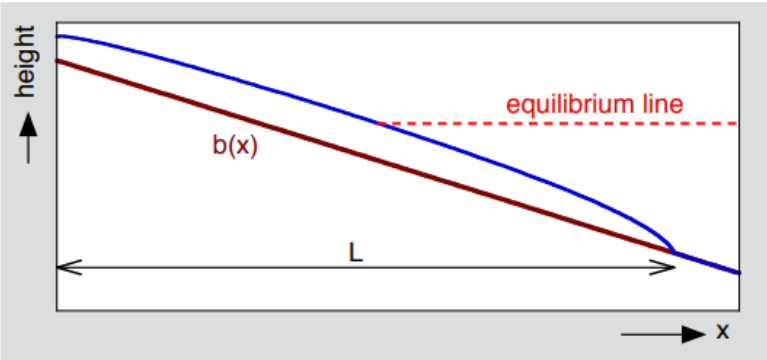

Figure 31: *Diagram illustrating the simple geometry adopted by the Minimal Glacier Model. The blue curved line represents the glacier, lying on a constant bed slope* (Oerlemans 2008).

Where $b(x)$ is the bed with constant slope, s, and is given by:

$$b(x) = b_0 - s\,x \tag{19}$$

Then, according to this simplified model the balance rate is assumed to vary linearly with altitude:

$$\dot{b} = \beta(h - E)$$

(20)

Where h is the altitude line and E is the equilibrium line altitude (ELA).

In this work, the Minimal Glacier Model was applied to Indren Glacier for two purposes:

(i) A first order estimate of glacier's length dependence on air temperature;
(ii) A rough investigation of the glacier's length-thickness relationship.

4.1.3.1 Sensitivity to temperature modifications

With the aforementioned simplifications and assuming to have the equilibrium line following an isotherm, Oerlemans (2011) developed the following expression:

$$\frac{dE}{dT_{fa}} = -\frac{1}{\gamma_a}$$

(21)

Where dT_{fa} is the ambient free air temperature gradient ($°C\ year^{-1}$) and γ_a is the temperature lapse rate ($\gamma_a < 0$ ($°C\ km^{-1}$)). This formula implies that for a given change in temperature, the change in equilibrium line will be proportional and negative, expressing what already discussed in the foregoing paragraph: as the temperature increases, the equilibrium line will move downwards and vice versa.

From this formula, another expression, showing the sensitivity of the glacier's length (L) to temperature changes, as a function of only the atmospheric lapse rate and bed slope was derived by the author:

$$\frac{dL}{dT_{fa}} = \frac{2}{\gamma_a s}$$

(22)

This expression corresponds to the curve shown in Figure 32.

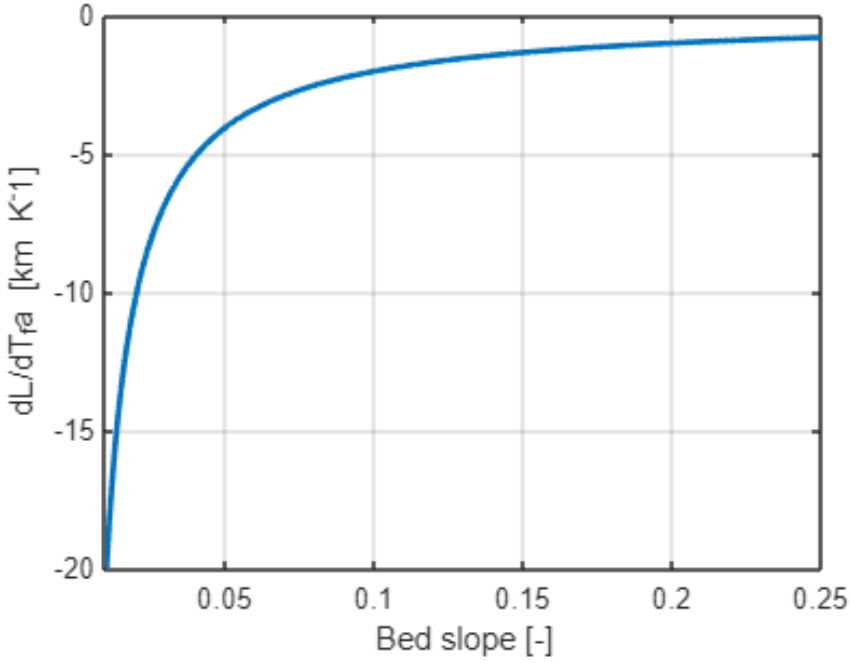

Figure 32: *Glacier length and air temperature relationship as a function of bed slope (assuming* $\gamma_a = -9.8\,°C/km$*).*

According to this model the sensitivity of the glacier's length to the temperature variations, is expected to be larger for small values of the bed slope.

Equation 22 was applied to the Indren Glacier in order to estimate its annual length change with temperature. The modeled horizontal variations were then compared to the actual observed changes, using historical data of the glacier's geometry.

For the application of this model it was assumed an adiabatic lapse rate for dry air equal to $\gamma_a = -9.8\,°C/km$.

In the next paragraphs the procedure followed in order to find the two input parameters of the model, namely the average bed slope and the free air temperature gradient, will be briefly described.

4.1.3.1.1 AVERAGE SLOPE ESTIMATION

For the estimation of the mean slope, s, of the glacier, the DEM of 2008 was utilized, as described in Section 3 (Analysis of Superficial Variations). Starting from it, the slope was retrieved by computing the elevation gradient cell by cell, along the East and North directions (Figure 33).

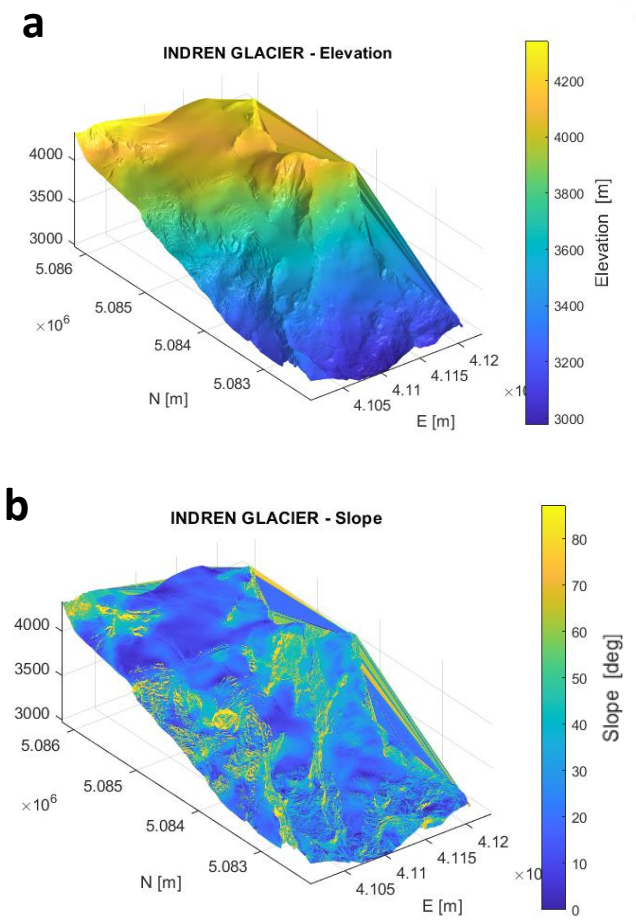

Figure 33: *3-D visualization of Mountain sector containing Indren Glacier: (a) Digital Elevation Model; (b) Slope.*

The obtained slope layer was then trimmed within the 2018 perimeter and the average slope within this area was calculated to obtain the final bed slope of the glacier at 27°.

4.1.3.1.2 FREE AIR TEMPERATURE GRADIENT ESTIMATION

For the estimation of the free air temperature gradient, dT_{fa}, open access temperature data coming from three different meteo stations close to Indren Glacier were considered: Bocchetta delle Pisse, Capanna Margherita and Gabiet (Figure 34).

Figure 34: *Location of the three meteo stations with respect to Indren Glacier[23]. Capanna Margherita and Bocchetta delle Pisse belong to the Piedmont region administration, whereas Gabiet is located in the Aosta Valley.*

In particular, Table 2, shows more detailed information regarding the location, data source and data availability of the meteo stations:

Table 2: *Detailed overview of the three distinct stations.*

Station Name	Region	Data source	Longitude (deg)	Latitude (deg)	Z (m asl)	Data availability
Bocchetta delle Pisse	Piedmont	ARPA Piemonte[24]	7.901	45.876	2410	1988-2022
Capanna Margherita	Piedmont	ARPA Piemonte	7.877	45.927	4554	2002-2022
Gabiet	Aosta Valley	Regione VdA[25]	7.849	45.852	2379	2002-2022

The two closer meteorological stations to the Indren Glacier are located in Bocchetta delle Pisse and Capanna Margherita, however the data available from the latter only covers a period of 20 years (2002-2022).

[23] Source: Google Earth.
[24] https://www.arpa.piemonte.it/rischinaturali/accesso-ai-dati/annali_meteoidrologici/annali-meteo-idro/banca-dati-meteorologica.html
[25] https://presidi2.regione.vda.it/str_dataview_download

For a more robust estimate of the temperature gradient, it is generally recommended to use a timeseries of at least 30 years. Therefore, for the implementation of the Minimal Glacier Model, the data from Bocchetta delle Pisse, with the longest timeseries (1988-2022), was used.
Nevertheless, to gain a more comprehensive understanding of the climate in the area of interest, the free air temperature gradient was calculated for all three stations (Table 3). For this purpose, the same processing steps were applied to all three datasets, however, the following section details the processing executed specifically to the Bocchetta delle Pisse dataset (see Appendix B for the processing flow of Capanna Margherita and Gabiet data sets). Figure 35 shows the original dataset of temperature registered at the reference meteorological station.

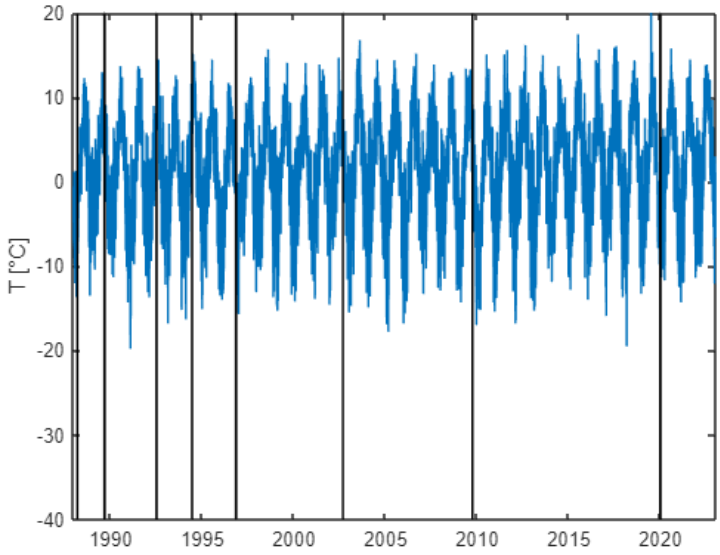

Figure 35: *Raw temperature data acquired at Bocchetta delle Pisse (1988-2022).*

The black vertical lines in the graph indicate the days of the year when the meteorological station was not recording data, probably because of a malfunctioning of the instruments on those days.

These missing data were replaced with average values calculated by considering the same days of the year for those years that had measurements. Additionally, the dataset was cut to complete years to obtain the same number of measurements for each day. The results are shown in Figure 36.

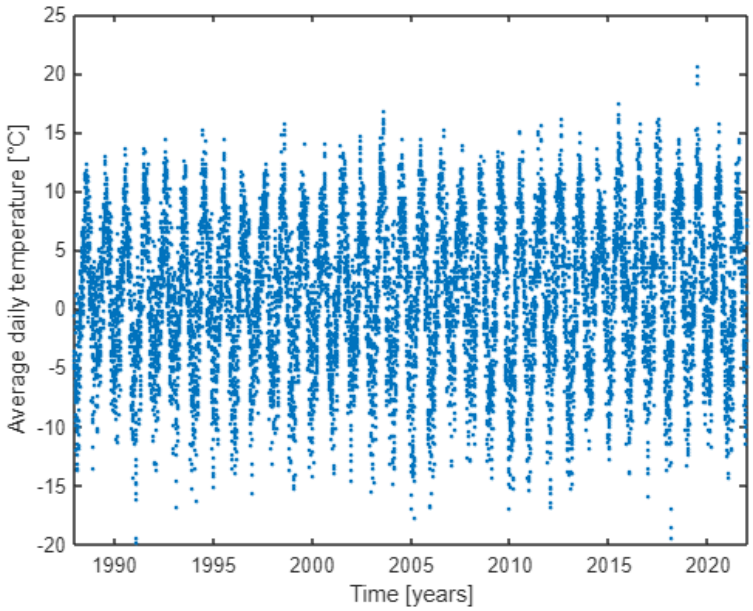

Figure 36: *Temperature data after gap filling process.*

As it is possible to see, the dataset shows a periodic behavior due to the astronomic component (i.e., changes in solar radiation during the year because of the Earth's rotation). The periodic component can be expressed according to the following:

$$\psi = A_1 \cos(2\pi f_1 t + \phi_1) + A_2 \cos(2\pi f_2 t + \phi_2) + \cdots + A_n \cos(2\pi f_n t + \phi_n) \quad (23)$$

Where t is time, A is the amplitude, f is the frequency and ϕ is the phase of the harmonic components. The harmonics considered in this analysis were those related to one year (f_1), six months (f_2) and four months (f_3). By performing a spectral analysis of the data (Figure 37), it was possible to retrieve the amplitude and the phase of f_1, f_2 and f_3.

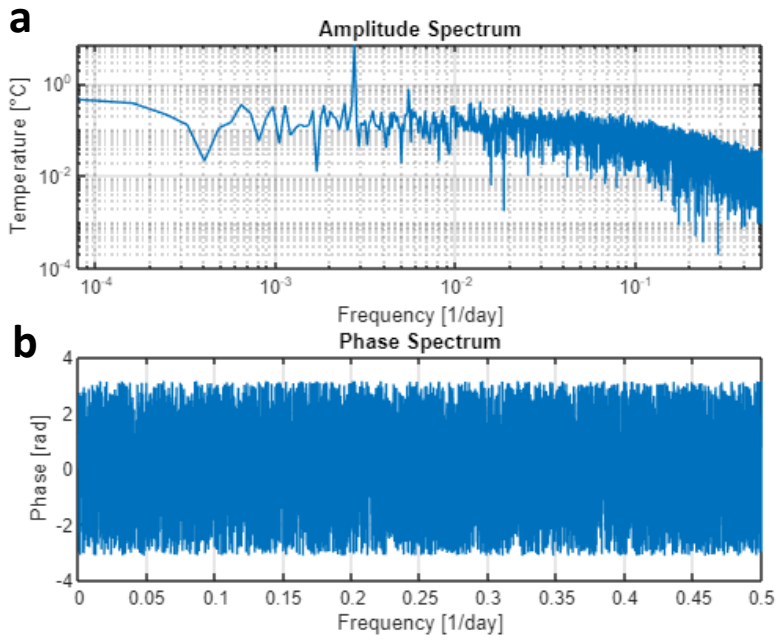

Figure 37: *(a) Amplitude Spectrum (b) Phase Spectrum of the temperature data.*

Once all the parameters of the above equation were found, the astronomic component shown in Figure 38, was computed and removed from the data, obtaining the residual variation represented in Figure 39.

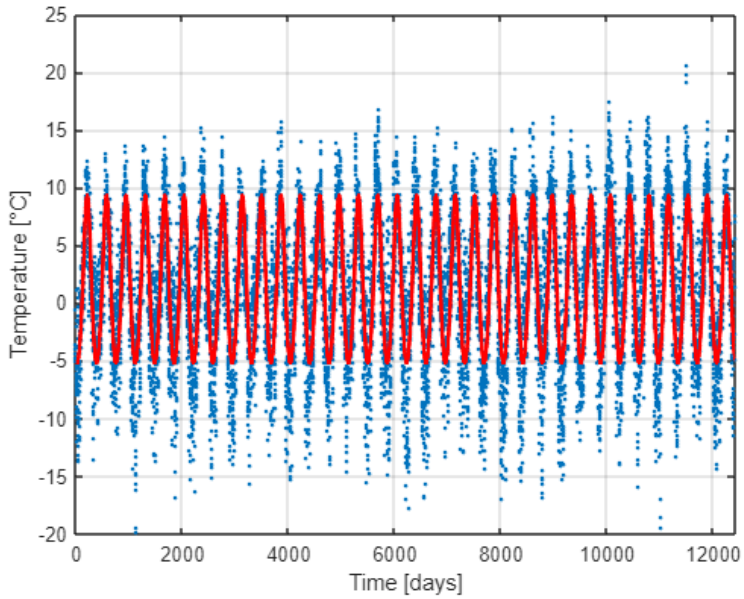

Figure 38: *Temperature data (blue) with astronomic component (red).*

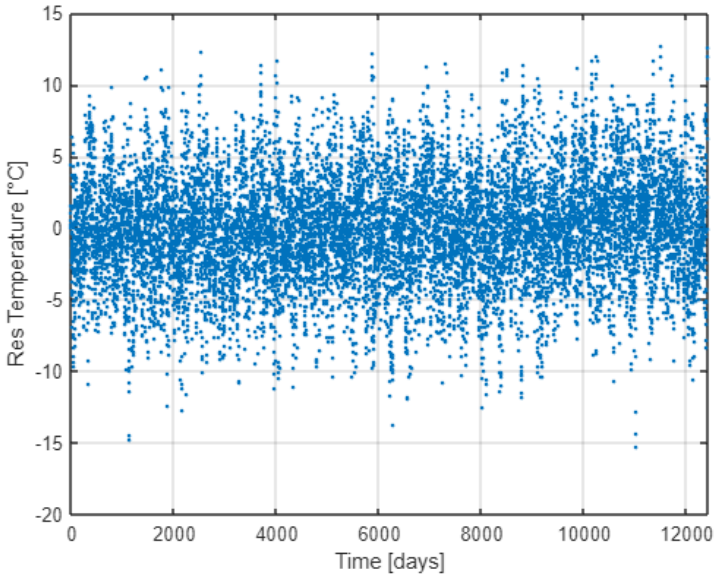

Figure 39: *Data residuals obtained through the removal of the astronomic component.*

Then, the residuals were fitted with a regression line in order to highlight the changes of temperature during the years (Figure 40).

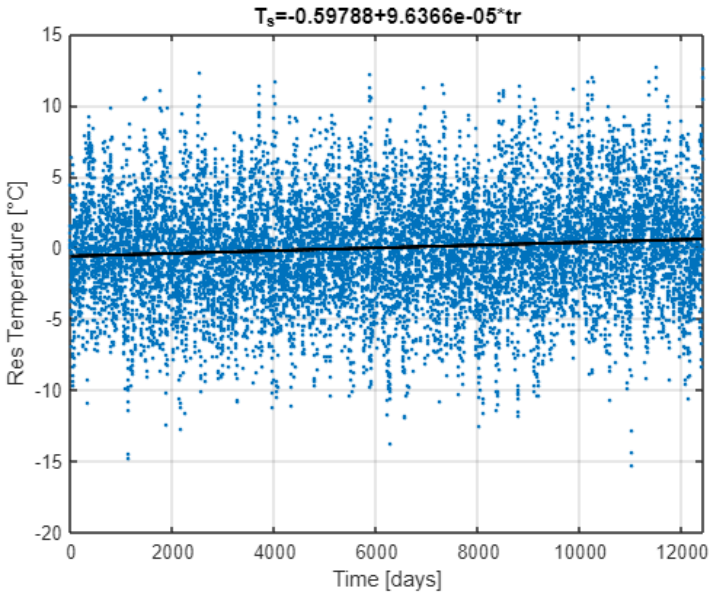

Figure 40: *Data residuals (blue) with linear regression (black).*

Finally, from the slope of the fitting line the free air temperature gradient, dT_{fa} was retrieved. The final results, obtained for all three stations, are displayed in Table 3.

Table 3: *Final free air temperature gradient obtained for the three different meteorological stations.*

Meteo station	Annual trend dT_{fa} ($°C\ year^{-1}$)	Standard deviation ($°C\ year^{-1}$)
Bocchetta delle Pisse	0.040	± 0.003
Capanna Margherita	0.040	± 0.009
Gabiet	0.038	± 0.008

As you can see the final results for all three stations are similar, so using any of these values in the Minimal Glacier Model would not significantly impact the outcome. Thus the average gradient value of 0.04 °C/year, detected from Bocchetta delle Pisse station, was used as input in the model (Equation 22).

4.1.3.2 Length-thickness relationship

Oerlemans also provided a simple formulation describing the relationship between the glacier's thickness and length, starting from the ice volume expression:

$$V = w\, H(t)\, L(t) \tag{24}$$

Where w is the glacier width, assumed constant, while $L(t)$ and $H(t)$ are the time varying length and thickness, respectively.

The L-H correlation is presented as follows:

$$H = \frac{\alpha_m\, L^{\frac{1}{2}}}{1 + v\, s} \tag{25}$$

Where α_m and v are constants, with the first parameter depending on the ice thickness value. This relationship implies that the characteristic basal shear stress, which is roughly proportional to the ice thickness multiplied by the bed slope, increases with glacier length (Oerlemans 2008).

For the application of the Minimal Glacier Model to the Indren Glacier, initial values of $v = 10$ (-) and $\alpha_m = 3$ ($m^{0.5}$) were directly taken from Oerlemans. These values were then tuned to the case of Indren Glacier using geometrical historical data.

4.1.3.3 Historical data validation

The Indren Glacier historical data[26] used both for the validation of the sensitivity of the length to temperature and the fitting of v and α_m parameters included a dataset of only 10 years (1820, 1882, 1941, 1952, 1968, 1975, 1999, 2005, 2012 and 2019). The data collection contained the area as well as the minimum, maximum and average elevation information of

[26] http://catastoghiacciai.partout.it/ice/bd_attuale?l=it

the glacier, but not all variables were defined for each year. Some years also had rough thickness estimations and corresponding ice volume calculations based on the thickness and glacier area. However, thickness data was limited and only available for a few years, with the latest measurement from 1975.

Figure 41 shows the ice thickness, glacier area and the ice volume, computed as the product between the glacier's area and thickness, for those years containing both information.

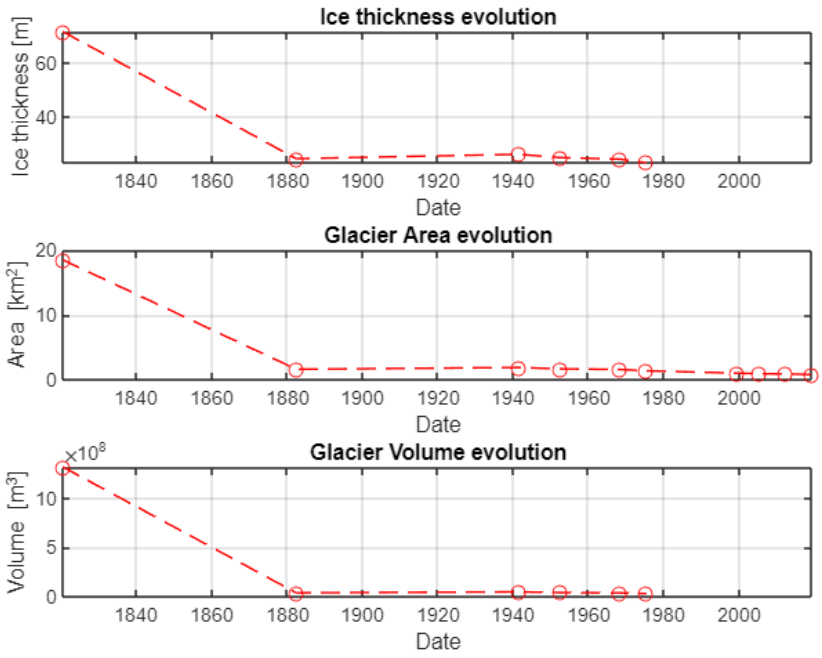

Figure 41: *Historical data of Indren Glacier ice thickness, area and volume, respectively. Years with available data are marked with circles in the graph.*

It is possible to note that between 1820 and 1880 a huge decrease in ice thickness, glacier area and consequently glacier volume has occurred, and in general a decreasing trend for all the parameters can be detected.

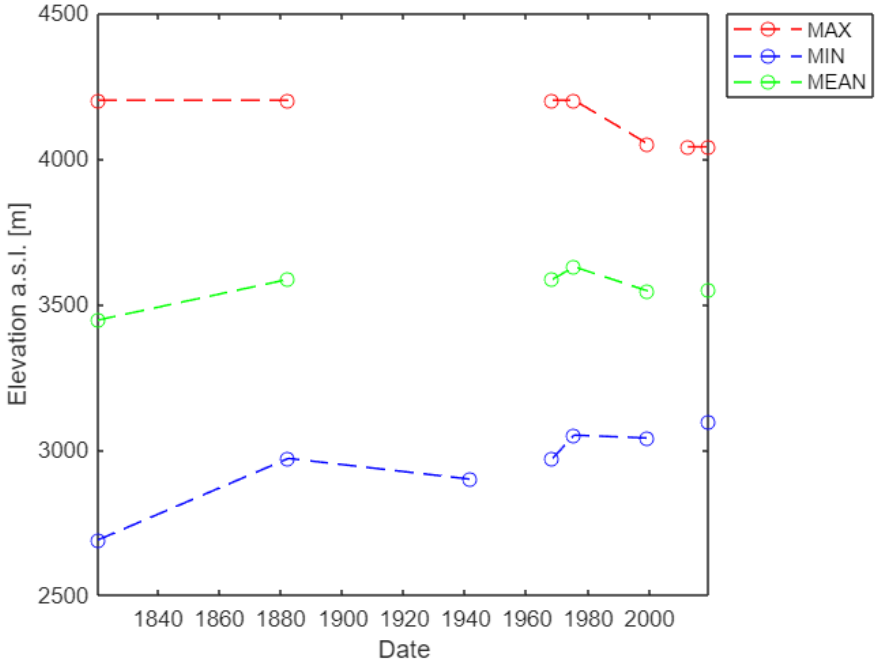

Figure 42: *Minimum, average and maximum elevation of Indren Glacier over the years. Circles indicate years with available data.*

Looking at the elevation data (Figure 42) an upward trend in the minimum elevation is noticeable. This is due to the glacier's retreating over time with rising temperatures, resulting in a shift of the minimum glacier elevation to higher altitudes.

On the other hand, the maximum elevation does not seem to be affected by the temperature variations and it appears to remain quite stable over the years. However, starting from 1980 a decreasing behavior is detectable. This can be due to a lack of snow and ice accumulation in the highest part of the basin which could be caused by a decrease in precipitation over the last years of the timeseries.

The mean elevation, instead, is balanced by the maximum and minimum elevation trends over time.

Using these data it was possible to estimate the occurred length variations over the years. First, 1975 and 2019 were taken as reference, as these represent the years with the earliest and latest thickness measurements. The observed length of the glacier was calculated for the reference years according to the following:

$$L_{r.y} = \frac{H_{max_{r.y}} - H_{min_{r.y}}}{s} \tag{26}$$

Where the r.y suffix stands for reference year, and H_{max} and H_{min} are the minimum and maximum elevations, respectively. This calculation allowed for the estimation of the observed

length changes between 1975 and 2019. Then this same procedure was carried out a second time, taking 1999 and 2019 as reference years.

4.2 Results

In this section, the results of the different analysis are shown.

4.2.1 GPR

After the processing steps described in Section 4.1.1 (GPR), the final radargrams were obtained. Through a visual inspection it was possible to retrieve the ice thickness in the considered locations by manually picking where the amplitude contrast was higher. For this purpose, the radargrams' color-scale was adjusted case by case in order to better visualize the glacier's bottom.

The final radargrams with the picked bottom depth are shown in this section, where the red lines represent the bedrock outline. Additionally, for profiles 1, 2-3 and 7 of the first survey campaign, it was also traced the hypothesized bedrock for the areas where the bottom was not visible but could be inferred. This, represented by a black dotted line, was not included in the depth picking because it was characterized by high levels of uncertainty, and since the GPR data were used in a second moment as constraint to the GlaTE model, it was preferred to avoid any interpretations that lacked a high degree of confidence. Nevertheless, for the sake of completeness, it was chosen to show the possible bottom behavior.

For simplicity, the data of the first survey campaign will be shown first (line 1 to 12, 200-MHz antenna), and those of the second campaign (line 1, 5 and 6, 70-MHz antenna) will be considered afterwards.

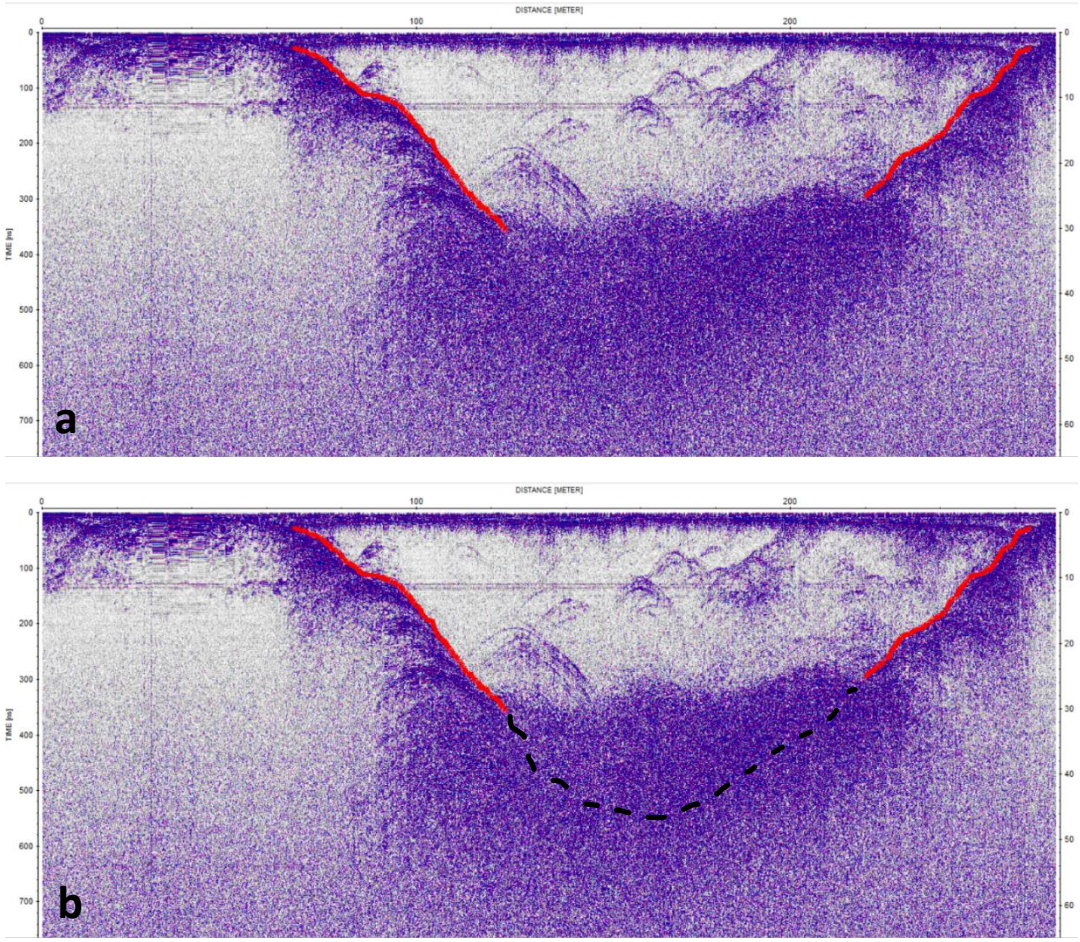

Figure 43: *Radargram of line 1 (first survey campaign, 200-MHz GPR antenna) with (a): picked visible glacier bottom interface only (red solid line), and (b): interpreted bottom morphology (black dashed line). The left y-axis is the twt (ns), while the right y-axis indicates the depth (m) considering a constant velocity of 0.17 m/ns. For the reflection amplitude scale refer to Figure 24.*

Figure 43 (a) shows the radargram of line 1 with the picked bottom. The signal was very clear at the lateral sides of the profile, while in the central part there was a diffuse-scattering phenomenon that did not allow any interpretation. This peculiar effect was present also for other profiles, and it will be addressed in Section 5 (Discussion). By ideally continuing the depth picking also in the high scattering area (Figure 43 (b)), it seems that the bottom could reach a depth of 40-50 m there. This value seems reasonable also considering the location of profile 1, which crosses the central part of the glacier (Figure 22), where generally the highest depths are reached.

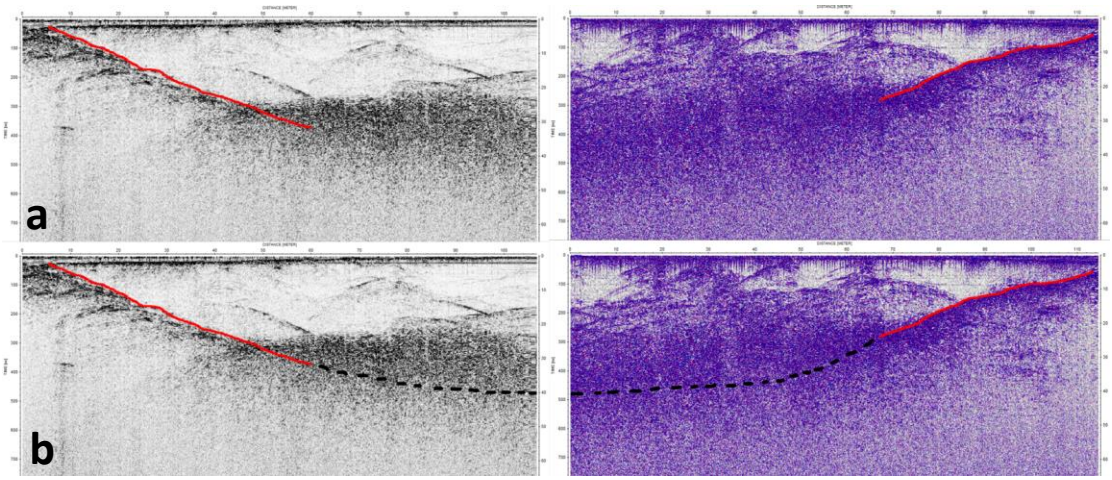

Figure 44: *Radargrams of lines 2 and 3, respectively, with (a): picked depth (red solid line) only, and (b): picked depth and interpreted depth (black dashed line). The left y-axis is the twt (ns), while the right y-axis indicates the depth (m) considering a constant velocity of 0.17 m/ns. Two different color scales are used to differentiate the two GPR profiles.*

Figure 44 shows the two adjacent profiles, 2 and 3. The glacier's depth was picked separately for the two cases. Putting the results together, it can be concluded that the obtained outcomes are coherent, where the shallowest depths are confined to the lateral sides, deepening as going towards the center. Also in this case the lack of confidence in the high scattering area did not allow a complete bottom picking, leaving room for subjective interpretations (Figure 44 (b)). Nonetheless, these interpretations are consistent and suggest a maximum depth of 40 m at the point where both lines converge. This smaller value compared to the maximum depth reached in line 1 depends on the location of acquisition of profiles 2 and 3, closer to the glacier's front, which is generally characterized by shallower depths.

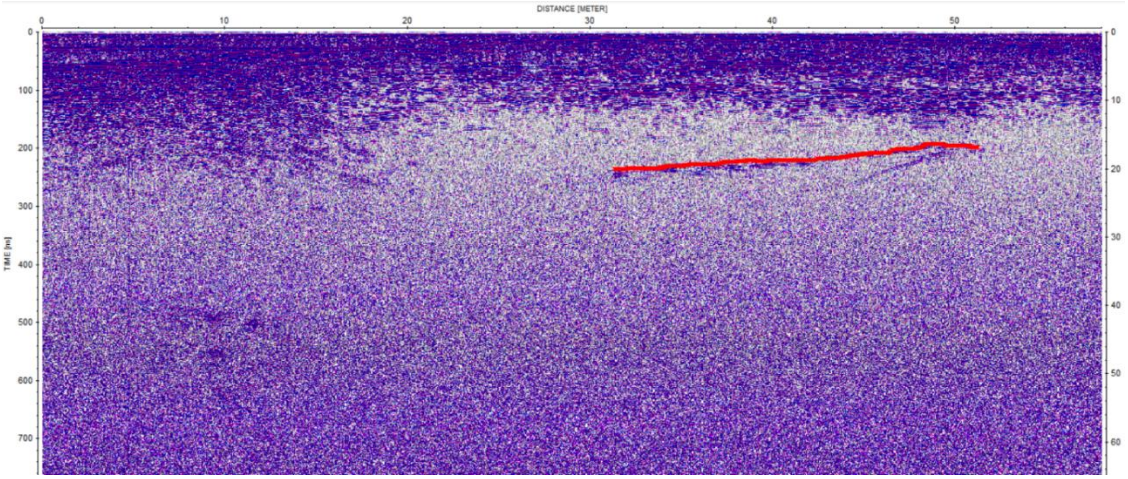

Figure 45: *Radargram of line 4 with picked depth (red solid line). The left y-axis is the twt (ns), while the right y-axis indicates the depth (m) considering a constant velocity of 0.17 m/ns.*

Figure 45 displays the results obtained for line 4. In this case, the signal was not very clear and it was possible to retrieve only few meters of the bottom: approximately 20 m long, corresponding to a depth varying between 15 and 20 m. By looking at Figure 22 it seems that this line was acquired outside the glacier's perimeter, directly on the bedrock. However, it should be recalled that the orthophoto of the glacier, and consequently its perimeter outline were taken in 2018, whereas the GPR survey was carried out in 2020. Therefore, during these two years some modifications in the glacier's perimeter may have occurred. Even though the reliability of this line was not clear, the observed depth was picked anyway. This decision was aimed by the fact that inserting this data in the GlaTE model would not have affected the final results because this algorithm only uses data falling inside the glacier's mask (i.e., 2018 perimeter).

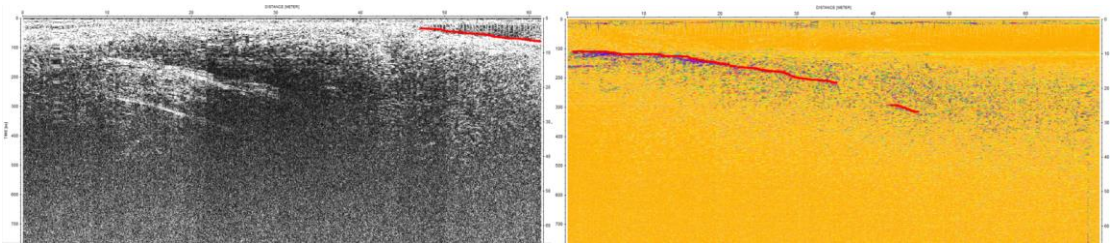

Figure 46: *Radargrams of lines 5 and 6, respectively, with picked depth (red solid line). The left y-axis is the twt (ns), while the right y-axis indicates the depth (m) considering a constant velocity of 0.17 m/ns. Two different color scales are used to differentiate the two GPR profiles.*

Figure 46 shows the depths retrieved for line 5 and 6. Similarly to lines 2 and 3, also these profiles were adjacent and the results taken for the two cases separately, confirm each other. These lines were acquired at the external side of the glacier, where the shallowest depths are expected. The obtained results are in line with this general assumption, as the depths are quite shallow, reaching a maximum value of approximately 30 m for profile 6.

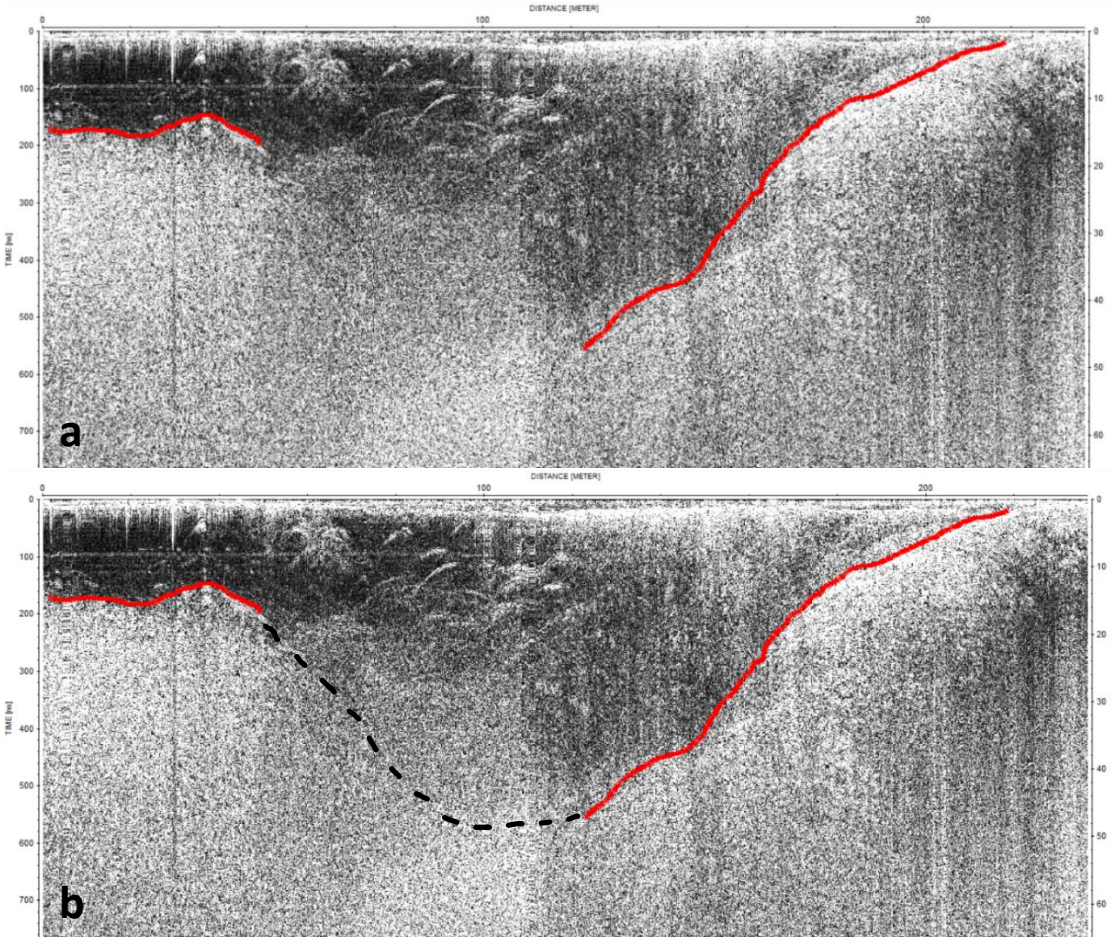

Figure 47: *Radargram of line 7 with (a): picked depth (red solid line) only, and (b): picked depth and hypothesized depth (black dashed line). The left y-axis is the twt (ns), while the right y-axis indicates the depth (m) considering a constant velocity of 0.17 m/ns.*

Line 7 (Figure 47 (a)) was acquired on the central part of the glacier, crossing it from side to side. This explains the high depth values (around 50 m) reached towards the center of the line. Also in this case, the diffuse scattering in the central area did not allow a complete bottom picking. Nevertheless, it was still possible to infer a probable bottom behavior (Figure 47 (b)).

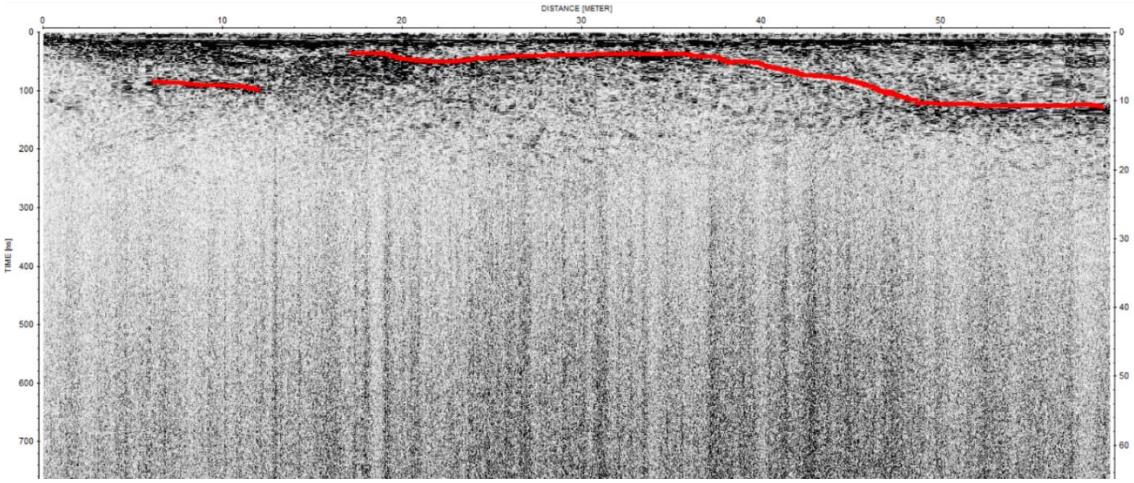

Figure 48: *Radargram of line 8 with picked depth (red solid line). The left y-axis is the twt (ns), while the right y-axis indicates the depth (m) considering a constant velocity of 0.17 m/ns.*

Figure 48 shows the result obtained for line 8. This profile was acquired close to the western border of the glacier. Therefore, it can be stated that the shallow depths observed in this radargram are compliant with the location where they were recorded.

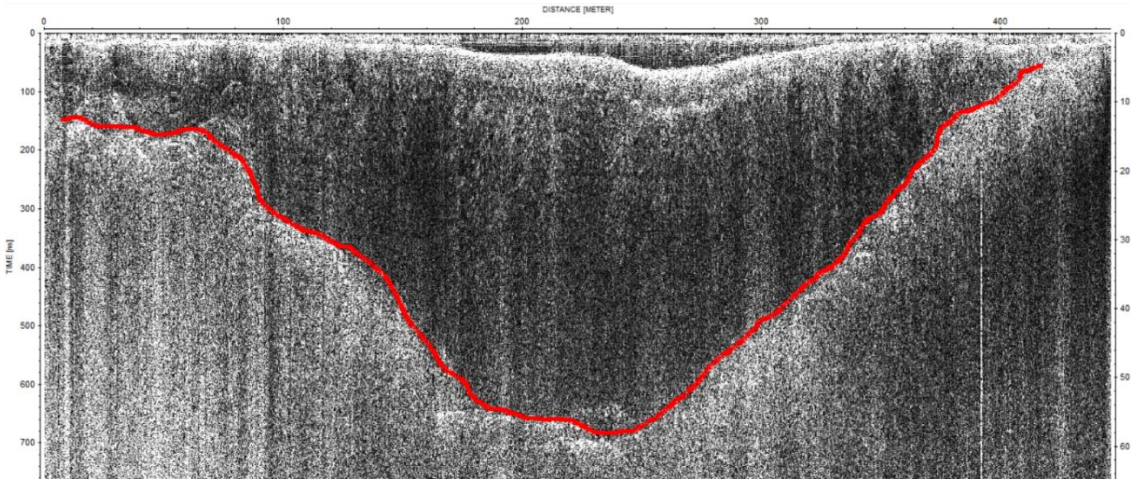

Figure 49: *Radargram of line 9 with picked depth (red solid line). The left y-axis is the twt (ns), while the right y-axis indicates the depth (m) considering a constant velocity of 0.17 m/ns.*

Line 9, represented in Figure 49, covered almost all the central part of the glacier, crossing it from the western to the eastern side for a total of 400 m length. The good quality of this data allowed to confidently pick the glacier's bottom along the whole profile. Here, the highest reached depth is around 60 m. Due to the high reliability of this profile, it could be used to further confirm the depth picked for line 8, as the right side of this last one touches the left part of line 9. In both cases a depth of c.a. 11 m was depicted. For a better visualization of the data intersections refer to Figure 56.

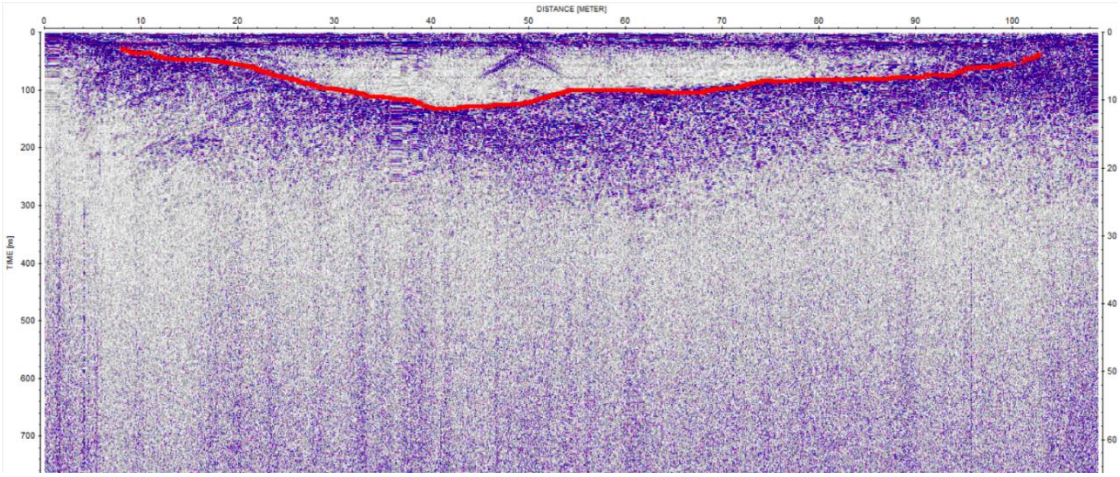

Figure 50: *Radargram of line 10 with picked depth (red solid line). The left y-axis is the twt (ns), while the right y-axis indicates the depth (m) considering a constant velocity of 0.17 m/ns.*

Figure 50 shows the results obtained for line 10. Again, the depths are quite shallow, not exceeding a value of 10 m, because the profile was acquired at the glacier's border.

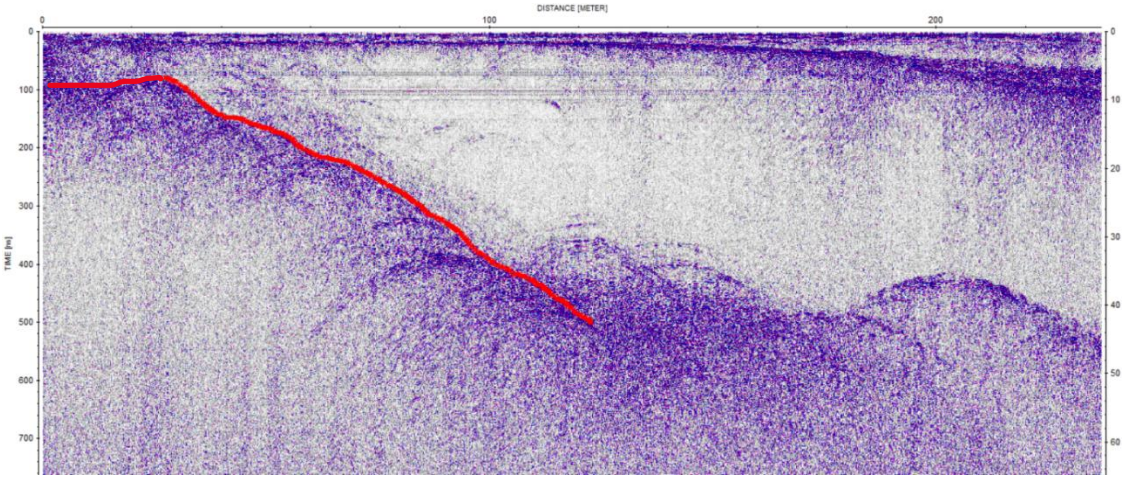

Figure 51: *Radargram of line 11 with picked depth (red solid line). The left y-axis is the twt (ns), while the right y-axis indicates the depth (m) considering a constant velocity of 0.17 m/ns.*

Figure 51 depicts the results of line 11. Similarly to other profiles, there is a loss of information as going towards the center of the glacier, however in this case it wasn't possible to assume any bottom behavior because of the high scattering.

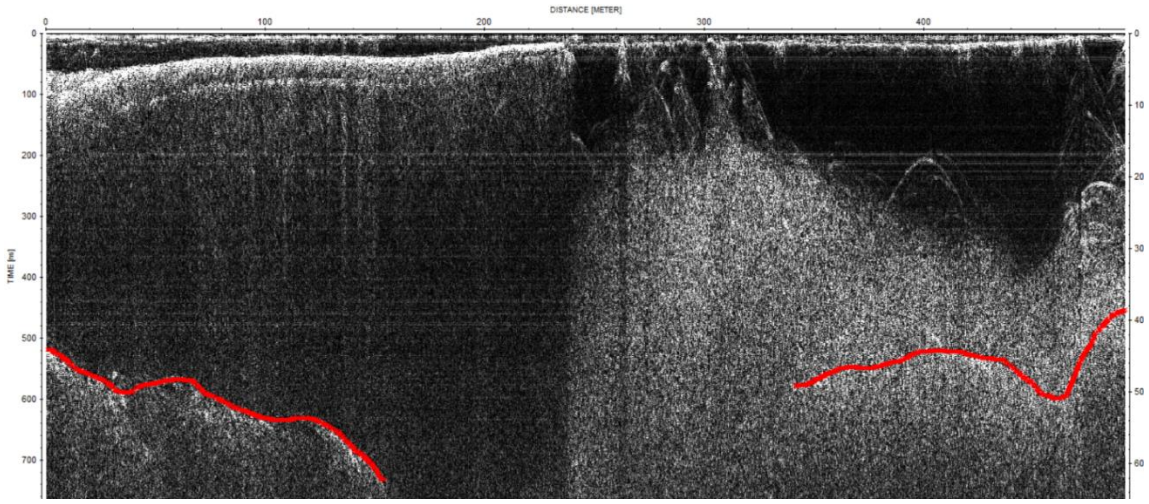

Figure 52: *Radargram of line 12 with picked depth (red solid line). The left y-axis is the twt (ns), while the right y-axis indicates the depth (m) considering a constant velocity of 0.17 m/ns.*

The results obtained for line 12 are displayed in Figure 52. Here, the scattering phenomena was particularly evident, with a much clearer signal on the left side of the radargram, compared to the right side. This line was the longest one of both survey campaigns, covering the glacier's surface longitudinally. Although it wasn't possible to retrieve any bottom morphology for the central part of the profile, it can be stated that the depths reached along this line are the highest, also considering its axial longitudinal location. This can also be confirmed by looking at the left side of Figure 52 where a maximum depth of c.a. 65 m can be observed. After this location, the glacier's bottoms probably exceeds the recorded twt.

The results obtained for lines 1,5 and 6 of the second survey campaign are shown in Figure 53, Figure 54 and Figure 55, respectively.

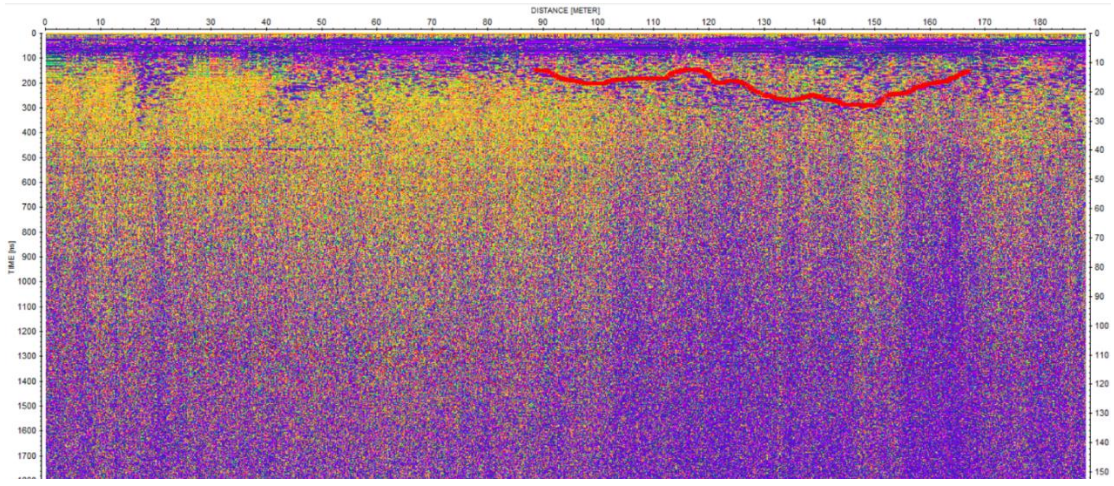

Figure 53: *Radargram of line 1(second survey campaign, 70-MHz GPR antenna) with picked depth (red solid line). The left y-axis is the twt (ns), while the right y-axis indicates the depth (m) considering a constant velocity of 0.17 m/ns.*

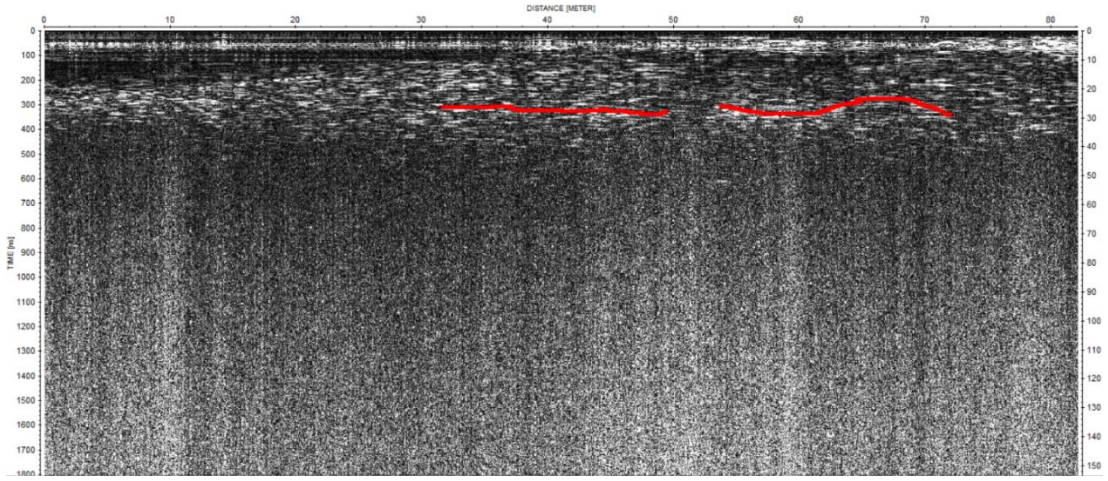

Figure 54: *Radargram of line 5 with picked depth (red solid line). The left y-axis is the twt (ns), while the right y-axis indicates the depth (m) considering a constant velocity of 0.17 m/ns.*

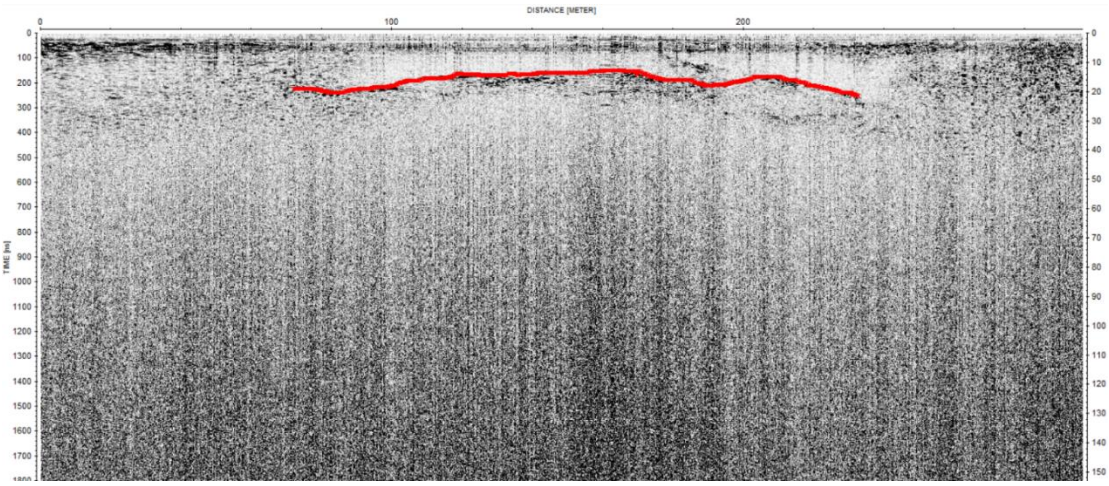

Figure 55: *Radargram of line 6 with picked depth (red solid line). The left y-axis is the twt (ns), while the right y-axis indicates the depth (m) considering a constant velocity of 0.17 m/ns.*

As already mentioned, it can be observed that the signal coming from the second survey campaign is of lower quality, probably because of issues occurred during the acquisition phase as well as the lower resolution of the 70-MHz antenna. However, it was still possible to retrieve some glacier bottom information. In particular, the results obtained for line 1 are partially confirmed by looking at line 10 (Figure 50): the two profiles are indeed very close to each other, where their distance is minimum in correspondence of the central part of line 10. In this zone, the picked depth is approximately 10 m for both profiles.

Concerning line 6, the picked depths seem to be quite shallow considering its location in the central part of the glacier (Figure 22). However, it is possible to note that this line was acquired close to the hole that has been forming over the years because of ice melting, therefore the low ice thickness values registered on line 6 might be due to the bottom morphology of the glacier which may be characterized by shallower bedrock in that area. Furthermore, considering also line 5, it can be observed that the two profiles confirm each other as the depicted depth remains quite constant at around 30 m for both cases.

The obtained results were displayed on ArcGIS Pro (Figure 56), highlighting the picked depths location through a color scale subdivided into 13 classes, with a 5 m range. From a first inspection, the typical U-shape glacier configuration can be recognized, where the shallowest depths are confined to the external areas, and the higher ones are found in the central zone.

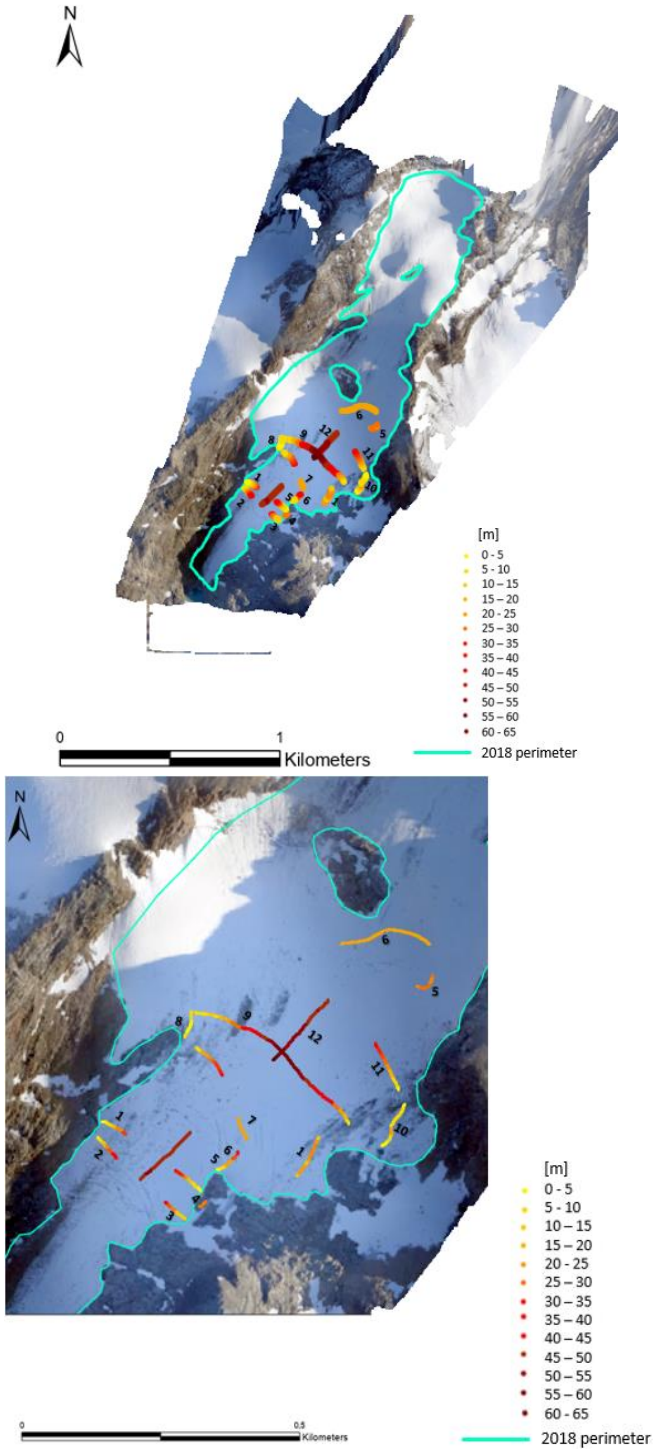

Figure 56: *Picked depths visualization on ArcGIS Pro with zoom on the GPR survey area. Colors indicate the ice thickness.*

Unfortunately, the high scattering zone present in the central area of the glacier did not allow to compare the different results obtained for the single lines where they converge. Only profiles 9 and 8, as well as lines 9 and 12 cross each other, showing a consistency in the obtained results. Nevertheless, even though the other picked depths do not meet each other, viewing them together, a general coherence can be observed, reinforcing the observations made by examining the radargrams.

4.2.2 GlaTE

As previously stated, the model was tested under three different smoothing scenarios, in order to investigate the estimated thickness variations with the resolution.

The following figures present the obtained results in different subplots. In particular, panel (a) shows the ice thickness estimation when only the glaciological model is applied (h^{glac}). Panel (b) displays the interpolation of the GPR data (h^{GPR}). Panel (c) illustrates the results from the GlaTE model (h^{est}), constraining the glaciological model with the GPR data. Panel (d) compares the results of the GlaTE model with those of Clarke et al. (2013) ($h^{est} - h^{glac}$).

These results are shown in Figure 57 for a smoothness factor equal to 5 (25 m resolution). Figure 58 displays the results for a smoothness factor equal to 10 (50 m resolution), while Figure 59 illustrates the obtained results for a smoothness factor equal to 20 (100 m resolution).

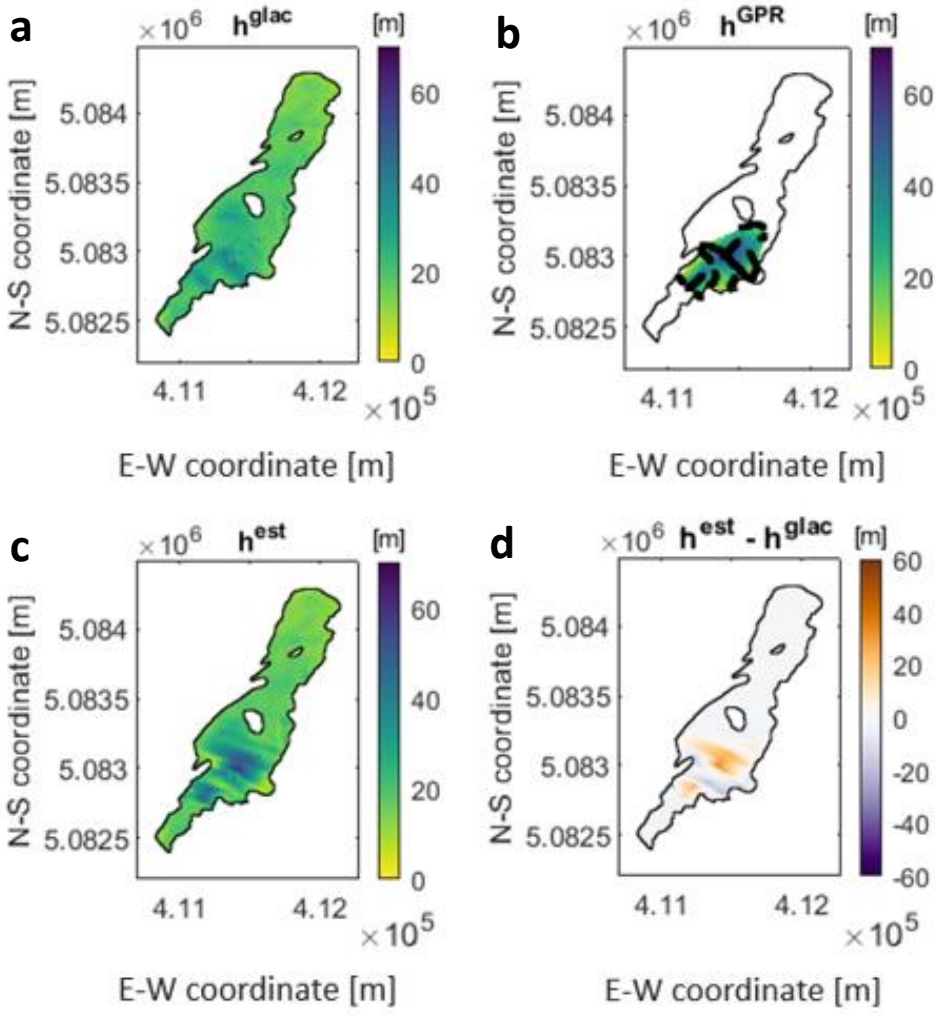

Figure 57: *Ice thickness results obtained using only (a) Clarke et al. (2013) glaciological model or (b) GPR constraint. Panel (c) shows the GlaTe results, while panel (d) shows the difference between results of panel (c) and (a). Colors indicate the ice thickness or ice thickness difference. Results obtained for a smoothness factor equal to 5 (i.e., 25 m resolution).*

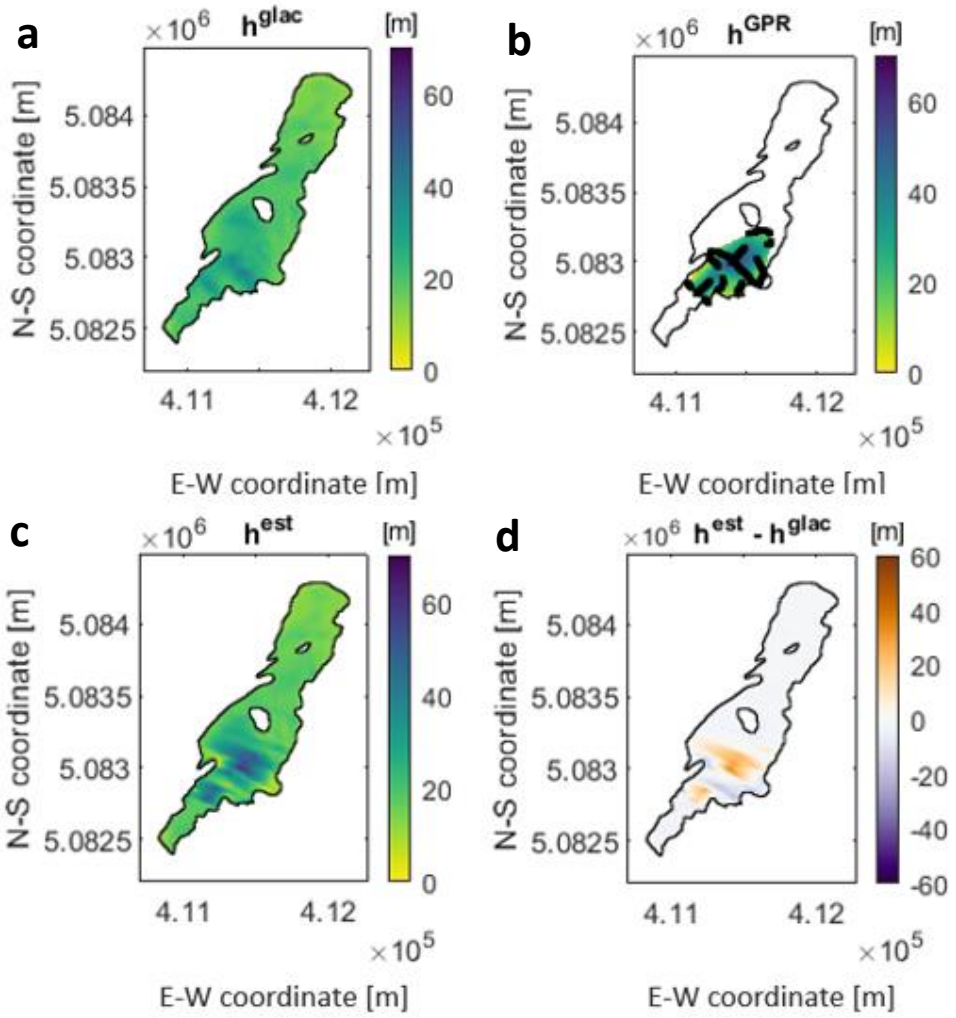

Figure 58: *Ice thickness results obtained using only (a) Clarke et al. (2013) glaciological model or (b) GPR constraint. Panel (c) shows the GlaTe results, while panel (d) shows the difference between results of panel (c) and (a). Colors indicate the ice thickness or ice thickness difference. Results obtained for a smoothness factor equal to 10 (i.e., 50 m resolution).*

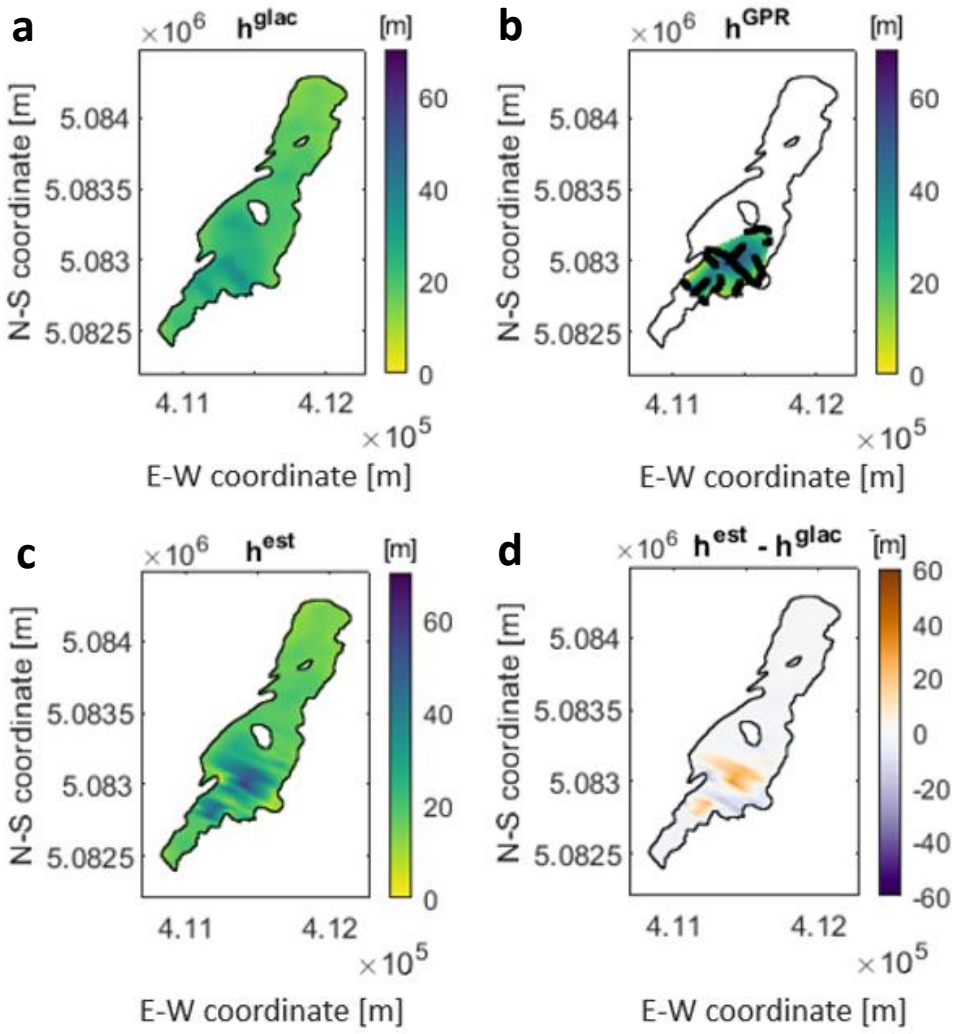

Figure 59: *Ice thickness results obtained using only (a) Clarke et al. (2013) glaciological model or (b) GPR constraint. Panel (c) shows the GlaTe results, while panel (d) shows the difference between results of panel (c) and (a). Colors indicate the ice thickness or ice thickness difference. Results obtained for a smoothness factor equal to 20 (i.e., 100 m resolution).*

The following considerations apply equally to the three resolution conditions as the overall trends are quite comparable.

Firstly, it is worthy to notice that the model's predictions for ice thickness in Panel B are only applicable within the area between the GPR profiles. This is a result of the model only performing data interpolation, as opposed to extrapolation.

Regardless, the interpolated GPR data, still confirms the U-shape of the glacier previously observed by examining Figure 56.

In contrast, the glaciological model, developed by Clarke et al. (2013), exhibits a more uniform behavior, with minimal variations in ice thickness.

The GlaTE model was able to smoothen up the discrepancies between h^{glac} and h^{GPR} by integrating the results of the two models, resulting in more accurate outcomes.

The $h^{est} - h^{glac}$ highlights the areas where the glacial model overestimates/underestimates the ice thickness. As it could be expected, the highest contrasts between the two models are concentrated in the region covered by the GPR surveys.

4.2.3 Minimal Glacier Model

4.2.3.1 Sensitivity to Temperature modifications

Applying the model Equation 22 (considering a mean slope of 27°, an adiabatic lapse rate of 9.8 °C/km, and an annual gradient temperature of +0.04 °C/year) an annual length variation of -16.02 m/year was obtained.

As previously mentioned, this result was compared with historical data to estimate the accuracy of the model.

Considering the elevation variations between 1975 and 2019 a total length reduction of 402.23 m was observed, with an annual reduction of approximately 9.14 m/year. Whereas considering the Minimal Glacier Model, it was estimated a total length reduction of 704.76 m over these 44 years, showing a model tendency to overestimate the length reductions.

The second analysis yielded an annual length variation of -6.38 m/year, with a total reduction of 127.54 m between 1999 and 2019. From the model it was obtained a total variation of -346.35 m over these 20 years.

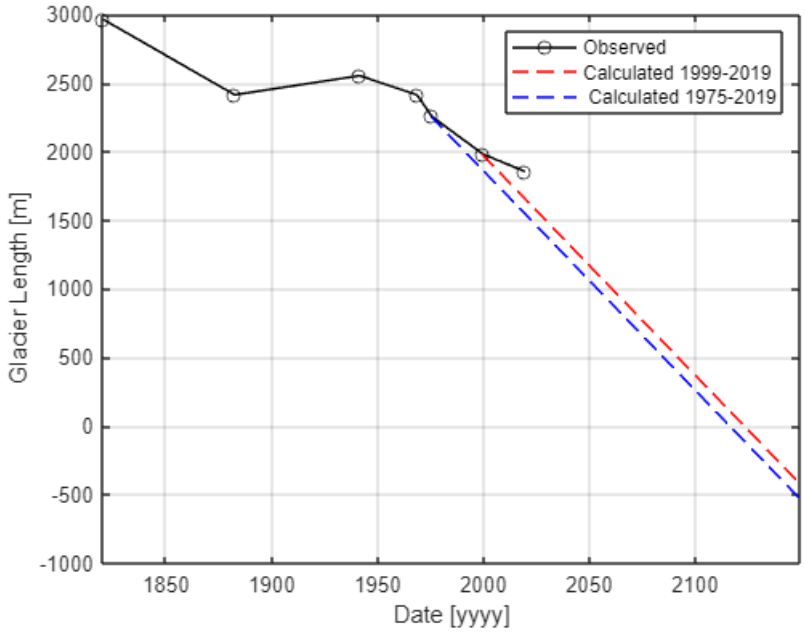

Figure 60: *Model results comparison between (1975-2019) and (1999-2019), with free air temperature gradient* $\mathrm{dT_{fa}} = 0.04\ °\mathrm{C}/year$*, taken from observed data at Bocchetta delle Pisse.*

Figure 60 shows the results of the Minimal Glacier Model considering the two time intervals described above. According to the model, taking 1975 and 1999 as reference years, by 2140 the Indren Glacier will be completely disappeared (glacier length reaches zero value). Nevertheless, it is possible to see that, in this case, the model is strongly influenced by the sudden length decrease occurred in 1975. This is the reason why the comparison was

performed a second time, between 1999 and 2019, excluding year 1975. However, although the second analysis displays a less pronounced decreasing trend, it still tends to overestimate the glacier's shrinkage. In this case, in fact, the glacier is estimated to disappear by 2150.

Comparing the obtained results with observed data it can be stated that the model shows significant inaccuracies. This is caused by the oversimplifications performed by the model. In particular, the heavily simplified bed slope estimation, as well as the uncertain value of the adiabatic lapse rate, have contributed to increase the model inaccuracy.

For this purpose a new analysis, considering a new value of the free air temperature gradient ($dT_{fa} = 0.02\ °C/year$), which could better fit the historical data, was conducted. The results of this analysis are represented in Figure 61 where the same steps implemented in the first analysis were followed, considering again the two time intervals: 1975-2019 and 1999-2019.

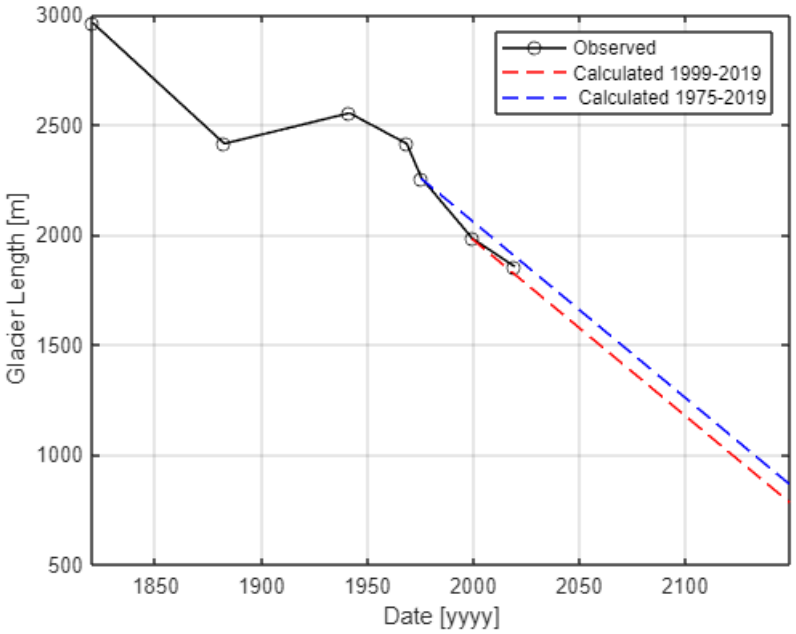

Figure 61: *Model results comparison between (1975-2019) and (1999-2019), with hypothesized free air temperature gradient* $\mathrm{dT_{fa}} = 0.02\ °C/year$.

The new calculations indeed reveals that the model, considering the new free air temperature gradient value, is more effective in interpreting historical data than in the previous case. In particular, in this case it was obtained a modeled annual length variation of -8.01 °C/year, with a total reduction of 352.38 m between 1975 and 2019 and 160.17 m between 1999 and 2019.

Table 4 shows a summary of the obtained results from the model, as well as from the historical data analysis:

Table 4: *Obtained results from Minimal Glacier Model considering the two different* $\mathrm{dT_{fa}}$ *values and time intervals and historical data analysis.*

	Model		Historical data	
	Total length variation (m)	Annual length variation ($m\ year^{-1}$)	Total length variation (m)	Annual length variation ($m\ year^{-1}$)
$dT_{fa} = 0.04\ °C\ year^{-1}$				
1975 - 2019	-704.76	-16.02	-402.23	-9.14
1999 - 2019	-346.35	-16.02	-127.54	-6.38
$dT_{fa} = 0.02\ °C\ year^{-1}$				
1975 - 2019	-352.38	-8.01	-402.23	-9.14
1999 - 2019	-160.17	-8.01	-127.54	-6.38

4..2.3.2 Length-thickness relationship

For the length thickness relationship Equation 25 was used, with an ice thickness ranging between 0 and 50 m.

Both thickness and length information of Indren Glacier were available only for 4 years: 1882, 1941, 1968 and 1975. The historical data were plot on the same graph of the model curve, in order to assess the ability of the model to fit them (Figure 62).

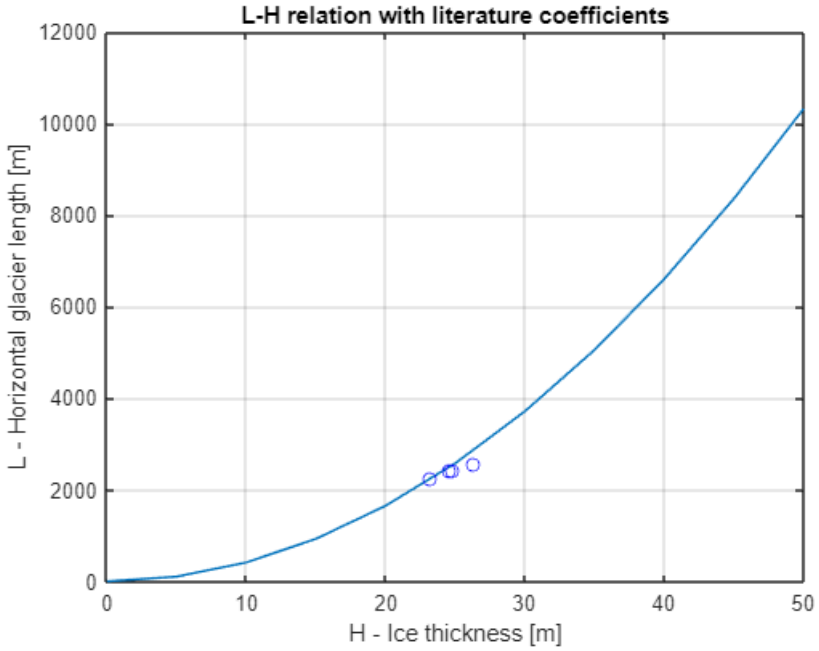

FIGURE 62: *Length-thickness relationship obtained through the Minimal Glacier Model (solid line) with literature parameters:* $\alpha_m = 3\ m^{0.5}, \upsilon = 10$. *Circles represent historical data.*

Figure 62 shows the model prediction for the parameters α_m and υ taken from literature. It can be observed that, although the historical data are quite aligned, the model does not

perfectly describe them. Through a model fitting, new parameter values, specific for the Indren Glacier case of study, were found (Figure 63). In particular, it was obtained $\alpha_m = 9.32\ m^{0.5}$ and $\upsilon = 34.19$.

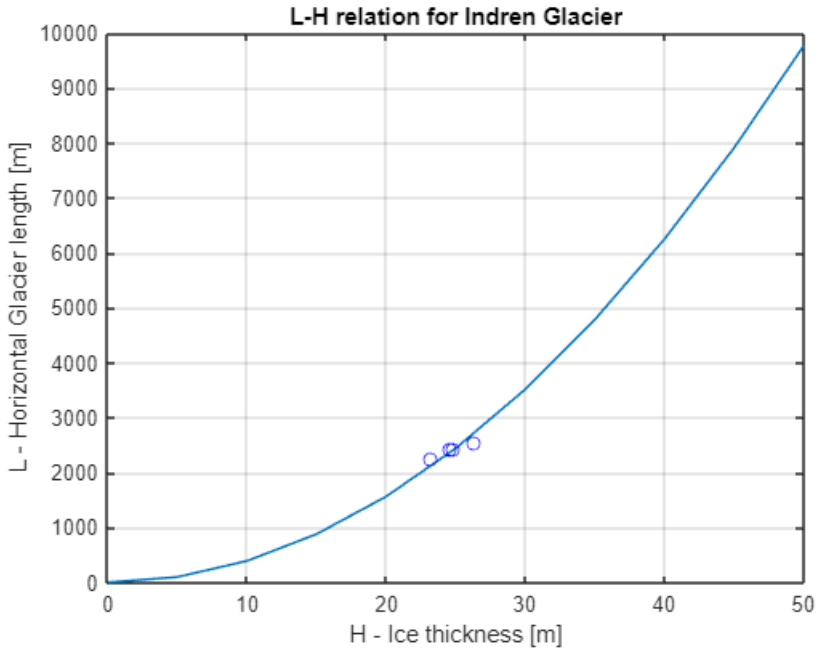

Figure 63: *Length-thickness relationship obtained through the Minimal Glacier Model (solid line) with parameter values obtained through tuning procedure:* $\alpha_m = 9.32\ m^{0.5}, \upsilon = 34.19$. *Circles represent historical data.*

As it can be seen from Figure 63, with these new values, the L-H function is able to better describe the historical data.

5 Discussion

5.1 Analysis of superficial variations

Looking at the results shown in Figure 15, it is possible to notice that in only 20 years the glacier has consistently shrank. Furthermore, considering both the elevation fluctuations and the areal extent of the glacier, it seems that the biggest changes occurred in the last decade, between 2008 and 2018.

From Figure 16 it can be observed that the ice loss has occurred mainly in the frontal part of the glacier. It is also interesting to notice that in correspondence of where the rock has emerged in the last years, a reduction in elevation is shown also in the layer subtractions (2018-2008 and 2018-1999).

In addition, Figure 16 also emphasizes that there have been no significant changes between 1999 and 2008. In actuality, it looks like the elevation, and therefore the ice thickness, has increased during these years. This last effect is actually due to an issue occurred with the standardized color scale used in Figure 16. The actual color scale of the difference in Figure 17 shows a decrease in elevation between 1999 and 2008, as the changes were too small to be accurately represented in the larger range of the standardized color scale. The ice thickness decrease registered between 1999 and 2008 is indeed around 6 m, which is much smaller compared to the 23 m of Figure 16. Besides, such small elevation decrease cannot be taken as a particularly remarkable value, reinforcing the theory that no huge change have occurred within this time period. Nonetheless, it is worthy to note that these elevation decrease are located at the highest altitudes, where the strongest sensitivity to climate forcings are experienced, and close to the zone where in 2008 the rock has emerged.

On the other hand, considering again Figure 16, it can be observed an ice thickness increase of about 10 m between 1999 and 2008. This was registered on the western side of the glacier, close to its perimeter, therefore such elevation increase could be explained by a possible debris deposition in that area, which is close to the delimiting rock of the glacier.

A further confirmation that the most severe ice losses have occurred in the second decade of the datasets, can be detected noticing that the elevation differences registered between 2008 and 2018 and 1999 and 2018 (Figure 16) are very similar, meaning that between 1999 and 2008 the elevation has remained quite constant. This effect was deeper investigated observing the temperature trends over the area of interest divided into the two considered decades. For this purpose, the data measured at Bocchetta delle Pisse was analyzed (Figure 64). It was obtained that between 1999 and 2008 there has been a temperature increase of only 0.031 °C/y $\pm$ 0.021 °C/y. While between 2008 and 2018 a temperature increase of 0.164 °C/year $\pm$ 0.018 °C/y was registered. This latter corresponds to a total temperature enhancement of 1.640 °C $\pm$ 0.180 °C over the last ten years.

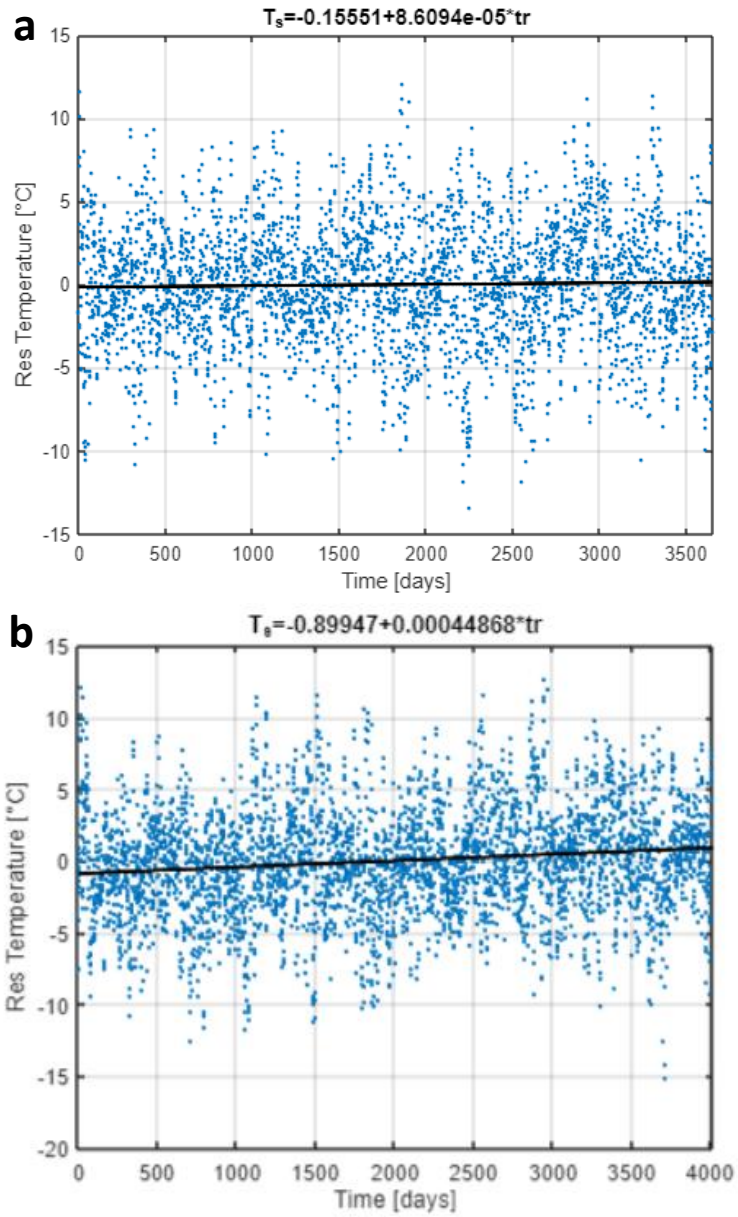

Figure 64: *Temperature trend measured at Bocchetta delle Pisse between (a) 1999 and 2008 and (b) 2008 and 2018.*

Further evidences support the rise in temperature recorded in the last years, like the one measured at Gabiet station, recording a mean air temperature increase of 2.8 °C between 2012 and 2015 (Colombo, et al. 2019).

Such high increase of temperature explains the large elevation variations observed in Section 3 (Analysis of Superficial Variations) between 2008 and 2018. The enhancement in air temperature may have led to a shift from solid to liquid precipitation and a more frequent and intense ice melting (Tognetto, et al. 2021). Even though some studies in literature have shown that generally glacial retreat is more influenced by temperature compared to snowfall (Giaccone, et al. 2015), specific considerations on the case of study have to be carried out, as some glaciers are more sensitive to summer temperatures and others to winter precipitations

(Peano, Chiarle and Hardenberg 2016). Therefore, in future, more detailed analysis taking into account also the snowfall time series should be performed. Nevertheless, this preliminary analysis of temperature trends is found to be consistent with the interpretations made on DTMs.

5.2 Analysis of internal variations

5.2.1 GPR

The diffuse scattering observed in the different radargrams which did not allow the bedrock recognition, could be caused by the transition between cold and warm ice, where the latter is characterized by the presence of small droplets of liquid water within it (Forte, et al. 2021). This resulted in an upper transparent layer in the radargram with only few reflections (cold ice), and a less transparent layer where diffuse scattering occurred (warm ice). To confirm this it should be recalled that both echo-sounding surveys were conducted during the summer period, when the high temperatures contribute to ice melting.

The existence of warm ice, causing the scattering events, can be linked to the presence of crevasses and fractures on the glacier surface, caused by the friction of the moving glacier, through which water percolates, reaching the ice-bedrock interface. Crevasses can be identified as multiple aligned scattering phenomena starting from the surface of the glacier. The water percolation, on the other hand, can be distinguished as subvertical scattering. In Figure 43, Figure 44, Figure 47 and Figure 52, it is possible to notice how the diffuse scattering occurs just below the crevasses indeed recognizable as aligned diffraction hyperbolas. Additional evidence can be found by examining the orthophoto (Figure 56), where the aforementioned profiles cross the crevasses (i.e., the black concave lines on the glacier's surface). This gives a solid explanation to the visualization problems encountered when analyzing the radargrams.

A peculiar feature is represented by line 12, for which the radargram could be subdivided into two sections (Figure 65): a left part where information can be easily retrieved and a right part where there is a high scattering zone. This phenomena is due to the different nature of the ice. On the left side of the line, the snow cover on the surface prevents from any water infiltration, leading to a more compact ice. On the other hand, the lack of any snowpack, as well as the presence of crevasses on the right side of the profile, leads to the presence of warm ice, likely rich in water. Additional cavities, observable on the right side of the profile, may have contributed to the water infiltration, enhancing the scatting phenomena.

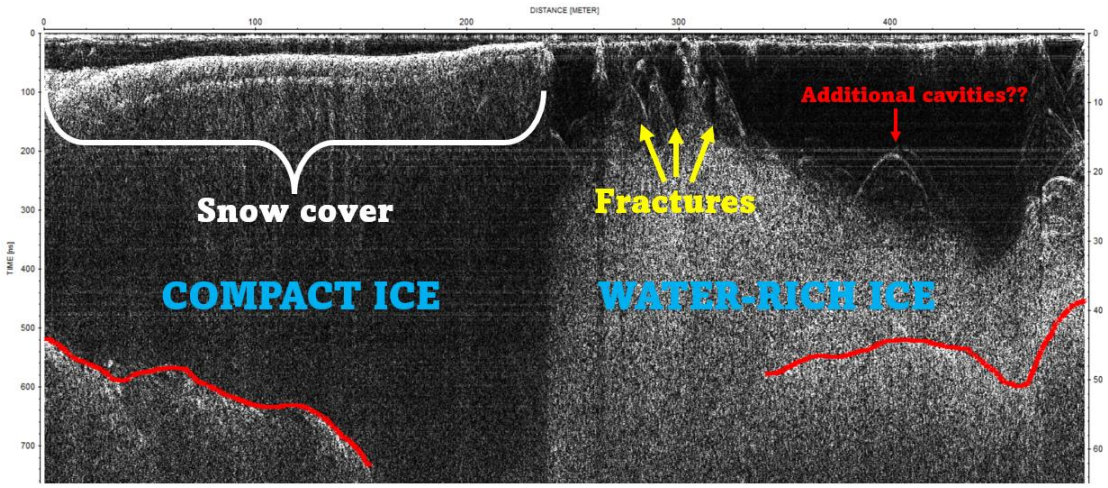

Figure 65: *Scheme displaying the cause behind the contrast between the left and right side of the radargram of line 12 (first survey campaign).*

Therefore, it can be deduced that the presence of snow cover over the glacier's surface, strongly helps in the bottom recognition, inhibiting water percolation. A good example can be given by line 9 (Figure 49) which shows how the presence of a snowpack all along the profile, allows for a clear visualization of the bedrock.

Based on these aspects, it can be concluded that the optimal period for conducting this type of surveys, in terms of data resolution quality, is likely during the winter. Nevertheless, the logistical and safety problems that may be faced during the cold months must be considered. The presence of snow does not allow the operator to clearly see the glacier's surface and the possible presence of crevasses. Due to the unfavorable winter conditions, field acquisitions are generally carried out in the warmer months, even if the internal conditions of the glacier are not optimal for the GPR survey.

Additionally, even if the glacier's surface was covered with snow and lacked crevasses or factures in that area, diffuse scattering phenomena could still be observed in the radargrams. Line 11 (Figure 51), in fact, shows no direct relationship between presence of crevasses in the upper layer and information loss at the ice-bedrock interface. Even though a snow cover is present all along the profile, and no diffraction hyperbola showing any fracture is detected by the radar, still information gets lost at the ice-bedrock interface, probably because of the presence of air/water-filled cavities. One possible reason behind this air/water infiltration could be due to the presence of past crevasses which with time have been closed by fresh snow compaction. Another potential explanation for this phenomenon could be a water infiltration occurring along the bedrock or the past deposition of mixed ice and debris (Forte, et al. 2021). This shows the fact that even in presence of a snow layer above the glacier, a loss of information could still occur.

Finally, also the antenna frequency could be investigated as a possible reason behind the scattering phenomena. In fact, the second survey campaign was conducted with a lower frequency because it was hypothesized that the diffuse scattering observed during the first campaign could be a result of insufficient penetration depth. High frequencies result in improved resolution, but this quickly deteriorates with greater depth and the radargrams

from the first campaign indeed seem to indicate a loss of information with increasing depth. However, the fact that the results of the second campaign are very poor, confirms that the diffuse scattering phenomena was independent from the chosen antenna. Furthermore, looking at the signals of line 1, 2-3, 7 and 11, it can be noted that information gets lost already at an early stage, within the first 300-500 ns, which correspond to quite shallow depths, contradicting the idea that the data loss is related to the decrease of resolution with depth. All these factors contribute to reinforcing the thesis that the phenomenon in question was just a direct consequence of the properties of the ice which was not pure and contained water droplets.

In conclusion, it is worthy to weigh the advantages and disadvantages of the application of GPR techniques to the case of glaciological studies. To begin with, the instrument in question is particularly light and easy-to-carry as demonstrated in Figure 18. This, combined with its high measurement rate, allows for a fast and easy survey campaign. Additionally, the fact that this type of survey is not invasive, non-destructive and do not need any contact, make this system particularly suitable for glacier-related studies. Finally, the low conductivity value of ice, does not attenuate the signal, making this method perfectly suitable for glaciological studies. Nevertheless, this system shows severe difficulties when applied in glacial environments characterized by the presence of crevasses and water, especially during summer period when surface snow melts.

A good way to improve the GPR surveys could be to mount the instrument on board of an aerial platform. This will allow to cover larger areas in shorter periods, avoiding the operators' exposition to challenging environments during winter periods (Forte, et al. 2021). However the costs for the survey would increase and the penetration depth, as well as the data quality, would decrease because of the presence of an additional layer of air between the instrument and the bedrock of the glacier[27].

5.2.2 GlaTE

Comparing the different model outcomes, it can be observed that, generally, the result of the glaciological model for 25-m resolution show some local heterogeneities in the central part, demonstrating a lower uniformity compared to the 50-m and 100-m resolution results. However, the entity of these heterogeneities is quite negligible and gets smoothened up by the GlaTE model, similarly to what happens to the other resolutions. Thus, it can be stated that the ice thickness modelled by the GlaTE algorithm is not particularly influenced by the pixel size used in the modelling process, given that similar results were obtained for the three investigated conditions. Under these circumstances, it is recommended to use the 100-m resolution results as reference. This decision is based on two factors. Firstly, the arrangement of the GPR data has a spacing larger than 100 m, therefore a model resolution which goes beyond this value is unnecessary. Secondly, following the aforementioned principle of Occam's razor, the simplest (i.e., smoothest) solution among options should be selected.

Examining the results of the glaciological model without the GPR constraints, it can be noticed that the predicted ice thickness is higher in the central region of the glacier, as opposed to the peripheral area. However, this over-deepening is much less pronounced compared to the one

[27] https://www.guidelinegeo.com/help-articles/what-is-a-drone-gpr/

observed from the GPR surveys. As a matter of fact, the maximum thickness predicted by the model of Clarke et al. (2013) in that specific region is around 40 m, whereas the GPR data indicate a depth of 60-65 m. This effect shows how the theoretical model alone tends to underestimate the ice thickness. This can be better observed by looking at the $h^{est} - h^{glac}$ graph, where a general underestimation of 20 m characterizes the glacial model. Only a small overestimation of 5 m can be observed on the lateral sides of the glacier. However, this value is not relevant if compared to the predicted underestimation.

The fact that the GlaTE model predicts high depths in the central part of the glacier, while in the other regions, smaller values are expected, could be linked to the fact that the areas remained uncover from GPR surveys can only rely on the glacial model estimations, which, as stated, showed underestimation issues. This does not clarify whether the external parts of the glacier are actually characterized by smaller thickness values or are only underestimated by the model. This aspect shows the limits of both GPR data and the theoretical glaciological model. On one hand, GPR surveys alone appear incomplete and inadequate to describe the whole glacier, since for a large part of it, which was not covered, no thickness estimation could be provided through data interpolation. On the other hand, the thickness estimated by the glacial model alone showed strong differences from the real bottom morphology observed through echo-sounding.

Nevertheless, the results obtained from GlaTE model are partially confirmed by other studies found in literature, showing the great advantages of combining the GPR data with the glacial model to obtain more reliable results. In particular, Figure 66 displays the results obtained by Viani et al. (2020) through the GlabTop (Glacier bed Topography) model applied to Indren Glacier. This model is based on an empirical relationship between basal shear stress and elevation (Linsbauer, Paul and Haeberli 2012). It is able to estimate the ice thickness starting from the glacier outline and its surface DEM. For this study, the authors have used a DEM acquired over the area of interest in 1991 and the glacier perimeter of 1999. This latter was modified in order to be in agreement with the hypothesized perimeter of the glacier in 1991.

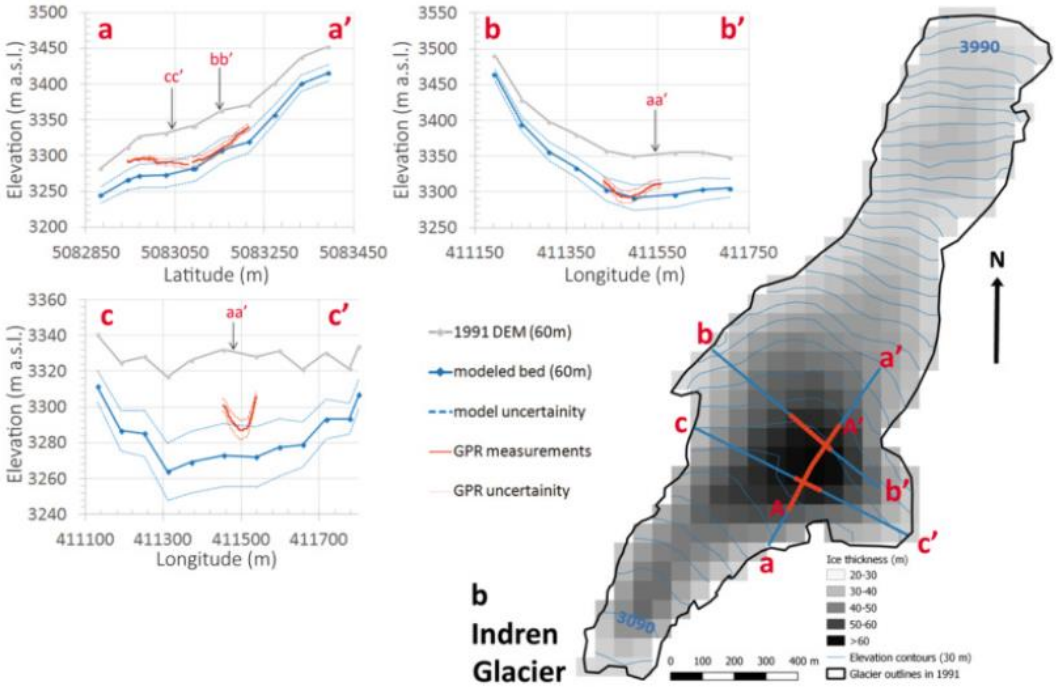

Figure 66: *GlabTop model results obtained for the Indren Glacier* (Viani, Machguth, et al. 2020)*. The three diagrams on the left represent the difference between the modelled results (in blue) and the radar measurements (in red).*

The authors of this study have then validated the obtained results through GPR data acquired over the lines indicated as aa', bb' and cc' in Figure 66. It can be observed that the model results are in agreement with the GPR data for lines aa' and bb', within the uncertainty ranges. For line cc', instead, the model does not well describe the U-shape of the glacier. Comparing these results with those obtained through the GlaTE model (Figure 59) it is possible to notice that the average thickness for the external area is of 10-20 m for GlaTE, whereas for GlabTop it is of 30-40 m. Furthermore, the GlabTop results reveal that the thickness of the glacier has a longitudinal distribution, and high depths (40-50 m) can be observed also on the frontal area. The GlaTE model, however, depicts a more uniform thickness across the glacier, with the exception of the central region, and the thicknesses in the frontal zone are shallower, around 20 m. Nevertheless, it is crucial to remember that the two models used DEMs from different time periods with a 20-year gap, justifying the differences in the predicted ice thickness, especially in the external areas of the glacier and in the shrinking tongue.

Additional evidences can be found looking at the DEM difference between 2018 and 1999 (Figure 16), where, within this time period, the elevation has decreased of 20 m in the front of the glacier, confirming what previously observed through the models. However, considering again the GlabTop and GlaTE outcomes, it can be seen that, at the highest elevations, between 1991 and 2018 a 20 m thickness reduction occurred, whereas, looking at the DEM difference, it seems that between 1999 and 2018 the elevation has increased of 10 m. The reasons behind this incongruity could be either due to the huge resolution difference between the DEM of 1999 and 2018, or because of an inaccuracy in the GlaTE or GlabTop results. Nevertheless, both models are in agreement for the central part of the glacier, where the highest depths are reached (50 to 60 m).

In addition to the research of Viani et al. (2020), other studies have been conducted in the area of interest. These literature works provided an opportunity to compare the GlaTE results with those of other studies. Specifically, previous research across all the Aosta Valley glaciers also adopted the GlabTop algorithm to estimate ice thickness over the region in 2008. The model was obtained starting from the region's glacier perimeters, their DEM and the central flowlines. By estimating the thickness for some specific points and interpolating the obtained values through the ANUDEM algorithm the researchers obtained the result shown in Figure 67 for the Indren Glacier.

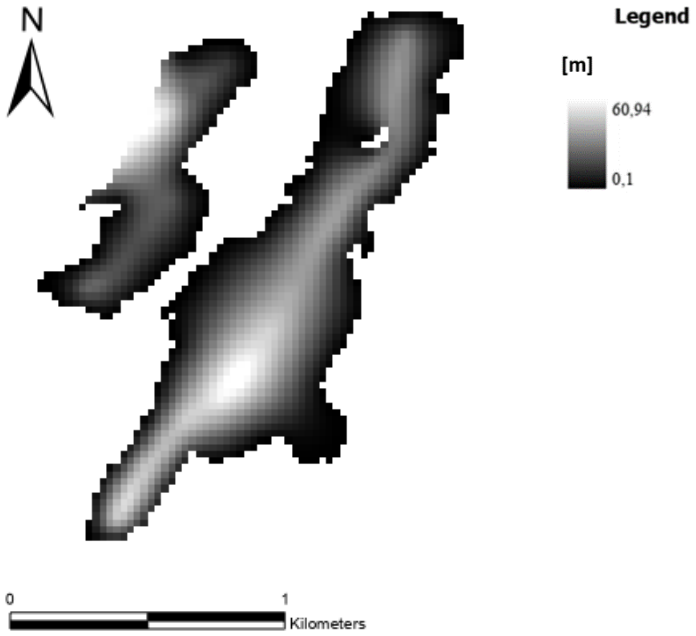

Figure 67: *GlabTop model results obtained for the Indren Glacier from a regional study of 2008* (Regione Autonoma Valle d'Aosta).

In detail, Figure 67 shows the Indren Glacier ice thickness estimated for 2008. In this case the glacier's depth is higher along the whole area, with values of approximately 45 m also on the front of the glacier, being in accordance with the results of Viani et al. (2020). The fact that the thickness estimated with the GlabTop algorithm remains quite similar for the study of Viani et al. (2020), based on a 1991 DEM and for the one conducted by Regione Autonoma Valle d'Aosta, based on the 2008 DEM, confirms the findings observed in Section 3 (Analysis of Superficial Variations). As a matter of fact, according to Figure 16, the highest elevation variations are registered between 2008 and 2018. This agreement is also verified by the temperature analysis conducted over the two time ranges. Additionally, Figure 67 confirms again the glacier's bottom characteristic of having the highest depths in the central area where GPR surveys were conducted.

For both the studies conducted by Viani et al. (2020) and Regione Autonoma Valle d'Aosta, it is particularly noteworthy that even though the GlabTop model was not based on GPR data, it was still able to show the deeper area in the center of the glacier, as revealed by GPR surveys. This further supports the findings of the GlaTE model, which used GPR data for that specific area.

In conclusion, the advantages and limitation of the GlaTE model can be discussed. From one hand, this algorithm offers significant advantages in constraining the glaciological model to echo-sounding data, as the integration of real data contributes to obtain more accurate results. Additionally, GPR techniques, as previously stated, are a fast and cost-effective way of collecting data. By including GPR data in the model, it was possible to obtain more accurate estimates of ice thickness for the entire glacier. On the other hand, the model showed some issues in describing the bottom morphology where no GPR data was acquired, and relying only on the glaciological model. This problem is linked to the value of the scaling factor α_{GPR} which strongly depends on the GPR data and on the assumption that these have a good areal coverage. This was not the case of this study, since the echo-sounding surveys covered only the central part of the glacier.

In future, a solution to this problem could be the estimation of α_{GPR} for many different glaciers. Through a statistical analysis, these values can be correlated with specific glacier's characteristics, such as the slope of the bed and the elevation of the area. In this way, more precise values of α_{GPR} also for cases where poor GPR data are available can be obtained (Langhammer, et al. 2019).

Finally, it can be concluded that in order to obtain better results from GlaTE modelling a better distribution of GPR data, covering the whole glacier's surface, would be recommended. Furthermore, the implementation of a more complex glaciological model, taking into account more parameters, could help in order to obtain better estimation for the areas not covered from GPR surveys. Moreover, overlapping GPR profiles generally help in validating the ice thickness estimated by analyzing single radargrams. This was the case of this study, however, the presence of water-rich ice did not allow this verification since the loss of information often occurred in the crossing sections of the profiles. A suggestion in order to avoid ambiguity in the GPR results and consequently in the ice thickness modelling, could be to perform a two-step acquisition strategy, when logistically and economically possible (Langhammer, et al. 2019). This consists in performing a first GPR survey and, if needed, acquire other profiles where the difference between h^{glac} and h^{est} is too high.

5.2.3 Minimal Glacier Model

Although this model was based on heavy simplifications, it allowed to have a rough estimation of the future glacier's evolution (Figure 60 and Figure 61). Looking at the historical data, the glacier's length have been decreasing over time, starting from a value 3200 m in 1820, reaching 2000 m in 2018. However, the glacier's shrinkage forecasted by the model, using the observed free air temperature gradient (i.e., $dT_{fa} = 0.04\ °C/year$), is overestimated compared to the actual retreat.

With the second analysis, considering $dT_{fa} = 0.02\ °C/year$ better forecasts are performed by the model. However, this second value was not retrieved from any observations and was purely assumed in order to have better predictions. Nevertheless, the fact that the model was heavily simplified allowed for this second analysis, since also the other input parameters were approximated.

Considering Figure 63, the parabolic relationship between glacier's length and thickness seems to well describes the data, for which, the longer is the glacier, the deeper it will be.

However, the limited number of available data, used to validate the model, raises uncertainty about the model accurately reflecting reality and the obtained estimates cannot be taken as exhaustive and precise.

Both the results of the glacier's sensitivity to climate and length-thickness relationship studies, revealed the limitations of this model. The cause of these inaccuracies is related to the heavy simplifications on which the model is based. One example is represented by the assumption of a one-to-one relationship between the length of the glacier and the mean ice thickness, which can lead to significant errors. Also the assumed in-phase relationship between ice volume and glacier's length may not always be true, as out-of-phase conditions may occur. Some of the basic simplifications of this model are relatively close to real conditions. One is the perfect plasticity assumption, which may also seem one of the most critical. Among the other things, this assumption implies that when the slope is large, the expected ice thickness is small. In real cases, this was generally observed to be true for many mountain glaciers and small ice caps. Additionally, even if the perfect plasticity condition were removed, and shear stress were allowed to vary, the glacier would tend to a geometry for which the basal shear stress would fall in a very narrow range (Oerlemans 2008). This is because the glacier tends to move and shape itself in a certain way to minimize the driving stress which causes the glacier to move. Since the driving stress is proportional to both the surface slope and thickness of ice, the glacier will tend to maintain a geometry for which these factors do not change too much.

Concerning the glacier's sensitivity to climate and the forecast of future evolutions, it must be taken into account that each glacier is unique and may respond differently to changes in temperature and precipitation, depending on different influencing factors. One of the most determining features in the glacier melting rate is its orientation. Since Indren Glacier has a South aspect, the effects are even more important, as South facing glaciers melt at a higher rate compared to other cases (Sher, et al. 2020) because they get more direct sunlight during the day. Moreover, the impacts of the glaciers orientation are even more important for those located in mid-latitudes of the northern hemisphere (Geçen and Toprak 2018). Another relevant factor that could be taken into account is the presence of debris cover and deposited dust from close moraines which could affect the melting rate because of a reduction of albedo. Also the shape of the glacier and the formation of lakes on its surface have effects, however it is not easy to directly correlate it to melting (Haeberli, Oerlemans and Zemp 2019). All these factors, as well as others, contribute to define the glacier dynamics in response to climate forcing. However, the contribution of each of these factors is difficult to estimate and no univocal contribution can be extracted from the existing literature (Peano, Chiarle and Hardenberg 2016).

Finally, it should be noted that basing the study of a glacier's future projections only on the historical temperature trends may not be exhaustive. For a more complete analysis, also considerations on future emissions and possible temperature scenarios should be taken into account. However this type of study goes beyond the objectives of this work and it is necessary to remind the great advantage of the Minimal Glacier Model, namely, the limited number of parameters required. In fact, generally, studies related to the analysis of glacier's evolution tend to avoid using more complex models because of the high amount of detailed information that they would require, leading to under sampling issues. Finally, simple models allow the detailed analysis of each of the considered parameters and it is a useful tool in order to

investigate the robustness of the dynamic behavior of a more complex model. Therefore a simplified model, like the one analyzed in this thesis, can serve as a useful initial step for glacier analysis before more detailed estimates are made.

Conclusions

The increase in global temperature has caused the loss of ice all over the world, contributing to the sea level rise and other serious consequences. Mountain, and in particular, Alpine glaciers, have demonstrated to be particularly vulnerable environments, as with increasing elevation their sensitivity to external temperature variations increases as well. Moreover, their reduced areal extent, together with their high mass turnover rates contribute to increase their reactivity to external climatic factors. Researches conducted over Alpine regions have indeed demonstrated that these environments are losing mass at an alarming rate. The ice melting of Alpine Glaciers can have serious repercussions concerning natural hazards, ecological impacts, as well as socio-economic impacts on local communities also far from the source areas. Alpine glaciers represent, in fact, an important source for the European water cycle since four of the main continental rivers are generated from these mountains. The continuous shrinkage of these glaciers could lead to a shortage of the water resource for drinking, agricultural and power generation purposes.

The study of ice volume variations over these areas could help to understand the evolution of glaciers and their response to climate change, as well as to implement effective adaptation strategies for these areas. A fundamental parameter required for the definition of a glacier volume is its ice thickness, however, its estimation could be quite challenging. The analysis of the Indren Glacier, located in the Italian Alps, allowed to investigate the ability of different techniques to estimate the glacier's thickness, as well as its relationship to other glacier parameters and its evolution over time.

The use of DEMs for the analysis of external variations, allowed to perform a preliminary estimation of the ice thickness variation occurred between 1999, 2008 and 2018. Although the resolution of the different models caused some interpretation issues, it could be observed that the highest elevation changes have occurred over the second time interval (2008-2018). This was also confirmed by the analysis of temperature trends at the Bocchetta delle Pisse weather station, which revealed that between 2008 and 2018, the temperature increased five times more than it did during the time period from 1999 and 2008.

The GPR data allowed for the ice thickness estimation in the central part of the glacier. However, the presence of crevasses and the absence of snow cover on the glacier's surface lead to a water infiltration inside the ice matrix. This caused a diffuse scattering phenomena in some of the radargrams, which did not allow the bedrock recognition and, although some of the radar profiles crossed in some areas, the loss of information in those zones only allowed for a partial validation.

The ice thickness modelling through the GlaTE algorithm showed the advantages of combining echo-sounding data together with the theoretical glaciological model of Clarke et a. (2013), allowing to obtain overall accurate results. As a matter of fact, the glaciological model alone demonstrated a tendency to underestimate the glacier's ice thickness. On the other hand, radar data were inadequate to estimate the depth all over the glacier, as they were acquired over a sparse network of profiles in the central area of the glacier. By constraining the theoretical model with the GPR data, more reliable results were achieved all over the site of interest.

The final temporal analysis performed on the Indren Glacier through the Minimal Glacier Model allowed to obtain a preliminary estimate of the glacier's length relationship to climate and thickness, respectively. Since the model was heavily simplified, it wasn't able to provide accurate results. However, it was still capable of providing valuable insights into the temporal variations of the glacier. Moreover, this model allowed to investigate the fundamental relationships between the key parameters of the glacier, representing a good starting point for future studies with more complex models.

References

Annan, A.P. "GPR methods for hydrogeoogical studies." *Hydrogeophysics* 50 (2005): 185-213.

Baroni, C., Salvatore, M. C., Alderighi, L., Gennaro, S., Zanoner, T., Carton, A., Carturan, L., Zorzi, M., Giardino, M., Bertotto, S., Perotti, L. "Final volume of NextData Project. Chapter 8: The changing Italian glaciers" 2018.

Beniston, M., Farinotti, D., Stoffel, M., Andreassen, L. M., Coppola, E., Eckert, N., Fantini, A., Giacona, F., Hauck, C., Huss, M., Hendrick, H., Lehning, M., López-Moreno, J-M., Magnusson, J., Marty, C., Morán-Tejéda, E., Morin, S., Naaim, M., Provenzale, A., Rabatel, A., Six, D., Stötter, J., Strasser, U., Terzago, S., Vincent, C. "The European mountain cryosphere: a review of its current state, trend and future challenges." *The Cryosphere* 12 (2018): 759-794.

Clarke, G. K. C., Anslow, F. S., Jarosch, A. H., Radić, V., Menounos, B., Bolch, T., Berthier, E. "Ice Volume and Subglacial Topography for Western Canadian Glaciers from Mass Balance Fields, Thinning Rates, and a Bed Stress Model." *Jorunal of Climate* 26, no. 12 (2013): 4282-4303.

Colombero, C., Comina, C., De Toma, E., Franco, D., Godio, A. "Ice Thickness Estimation from Geophysical Investigation on the Terminal Lobes of Belvedere Glacier (NW ITalian Alps)." *Remote Sensing*, 2019.

Colombo, N., Bocchiola, D., Martin, M., Confortola, G., Salerno, F., Godone, D., D'Amico, M. E., Freppaz, M. "High export of nitrogen and dissolved organic carbon from an Alpine glacier (Indren Glacier, NW Italian Alps)." 2019.

Forte, E., Santin, I.,Ponti, S., Colucci, R. R., Gutgesell, P., Guglielmin., M. "New insights in glaciers characterization by differential diagnosis integrating GPR and remote sensing techniques: A case study for the Eastern Gran Zebrù glacier (Central Alps)." *Remote Sensing of Environment* 267 (2021).

Freppaz, M., Williams, M. W., Gabrieli, J., Gorra, R., Mania, I., Ascher-Jenull, J., Egli, M., Celi, L. "Characterization of organic-rich mineral debris revealed by rapid glacier retreat, Indren Glacier, European Alps." *Journal of Mountain Science* 18, no. 6 (2021).

Geçen , R., Toprak. V. "The effect of aspect on glaciation: A case study of Eastern Black Sea mountains (Turkey)." 2018.

Giaccone, E., Colombo, N., Acquaotta, F., Paro, L., Fratianni., S. "Climate variations in a high altitude Alpine basin and their effects on a glacial environment (Italian Western Alps)." *Atmòsfera* 28, no. 2 (2015): 117-128.

Godio, A., and C. Colombero. "Course material of Applied Geophysics." 2020-2021.

Haeberli, W., Oerlemans, J., Zemp., M. "The future of alpine glaciers and beyond." 2019.

Langhammer, L., Grab, M., Bauder, A., Maurer., H. "Glacier thickness estimations of alpine glaciers using data and modeling constraints." *The Cryosphere* 13 (2019): 2189–2202.

Linsbauer, A., Paul, F., Haeberli, W. "Modeling glacier thickness distribution and bed topography over entire mountain ranges with GlabTop: Application of a fast and robust approach." *JOURNAL OF GEOPHYSICAL RESEARCH* 117 (2012).

Liu, J., Wu, Y., Gao, X. "Increase in occurrence of large glacier-related landslides in the high mountains of Asia." *Sci Rep* 11 (2021).

Losapio, G., Cerabolini, B. E. L., Maffioletti, C., Tampucci, D., Gobbi, M., Caccianiga, M. "The Consequences of Glacier Retreat Are Uneven Between Plant Species." *Front. Ecol. Evol.* 8 (2021).

Lucchesi, S., Giardino, M., Perotti, L. "Applications of high-resolution images and DTMs for detailed geomorphological analysis of mountain and plain areas of NW Italy." *European Journal of Remote Sensing* 46, no. 1 (2013): 216-233.

Maggioni, M., Freppaz, M., Piccini, P., Williams, M. W., Zanini, E. "Snow Cover Effects on Glacier Ice Surface Temperature." *Arctic, Antarctic, and Alpine Research* 41, no. 3 (2009): 323-329.

Milner, A. M., Khamis, K., Battin, T. J., Brittain, J. E., Barrand, N. E., Füreder, L., Cauvy-Fraunié, S., Gìslason, G. M., Jacobsen, D., Hannah, D. M., Hodson, A. J., Hood, E., Lencioni, V., Òlaffson, J. S., Robinson, C. T., Tranter, M., Brown, L. E. "Glacier shrinkage driving global changes in downstream systems." 2017.

Navarro, F., Eisen, O. "Ground-penetrating radar in glaciological applications." In *Remote Sensing of Glaciers*, 195-229. 2009.

Oerlemans, J. *Minimal Glacier Models.* 2008.

Peano, D., Chiarle, M., Hardenberg, J. V. "A minimal model approach for glacier length modeling in the Western Italian Alps." *Geogr. Fis. Dinam. Quat.* 39 (2016): 69-82.

Pepin, N., Bradley, R. S., Diaz, H. F., Baraer, M., Caceres, E., B., Forsythe, N., Fowler, H., Greenwood, G., Hashmi, M. Z., Liu, X. D., Miller, J. R., Ning, L., Ohmura, A., Palazzi, E., Rangwala, I., Schöner, W., Severskiy, I., Shahgedanova, M., Wang, M. B., Williamson, S. N., Yang, D. Q., Mountain Research Initiative EDW Working Group. "Elevation-dependent warming in mountain regions of the world." *Nature Climate Change* 5, no. 5 (2015): 424-430.

Regione Autonoma Valle d'Aosta. SCT - Sistema Conoscenze Territoriali. n.d. https://mappe.regione.vda.it/pub/geoCartoSCT/.

Sandmeier Geophysical Research - Introduction to the processing of GPR-data within REFLEXW. n.d. https://www.sandmeier-geo.de/Download/gpr_2d_import_processing.pdf.

Sher, M., Lide, T., Shaukat, A., Yasir, L., Muhammad Atif, W., Muhammad, Arif, G., Muhammad, S., Iqtidar, H., Liu, S. "Thin debris layers do not enhance melting of the Karakoram glaciers." *Science of Total Environment* 746 (2020).

Tognetto, F., Perotti, L., Viani, C., Colombo, N., Giardino, M. "Geomorphology and geosystem services of the Indren-Cimalegna area (Monte Rosa massif – Western Italian Alps)." *Journal of Maps* 17, no. 2 (2021): 161-172.

Viani, C., Machguth, H., Huggel, C., Godio, A., Franco, D., Perotti, L., Giardino, M. "Potential future lakes from continued glacier shrinkage in the Aosta Valley Region (Western Alps, Italy)." 2020.

Viani, C., Machguth, H., Huggel, C., Godio, A., Perotti, L., Giardino, M. *Possible future lakes resulting from continued glacier shrinkage in the Aosta Valley Region (Western Alps, Italy).* Vol. 19, in *EGU General Assembly Conference Abstracts*, 14961. 2017.

Appendix A

This section focuses on the issue of the resolution difference between the oldest DTM (1999) and the more recent ones (2008 and 2018). The purpose of this analysis is to provide an explanation why the options presented in Section 3 (Analysis of Superficial Variations) were ultimately chosen as the most suitable ones.

Figure 68 displays the layer differences between 1999 and 2008, and 1999 and 2018, respectively. For this result, no processing was performed over the DTMs and the original resolutions of the models were used.

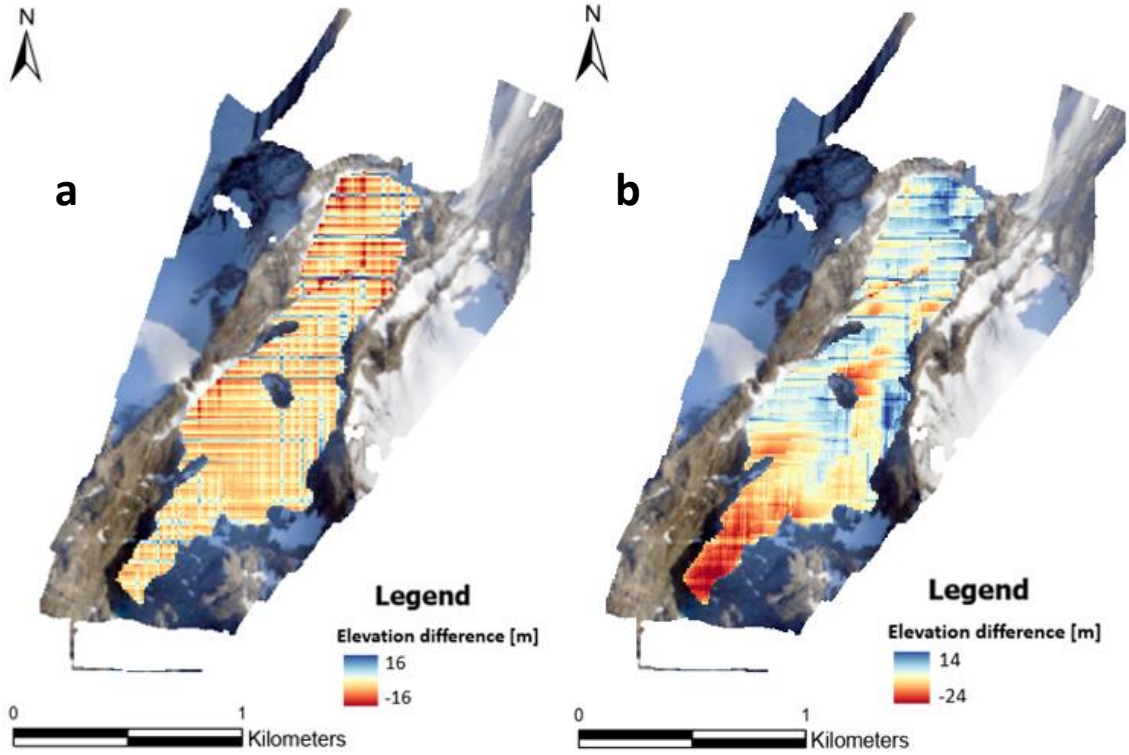

Figure 68: *Original Digital Elevation Models differences between : (a) 1999 and 2008 ; (b) 1999 and 2018,. No filter was applied in both cases.*

Looking at the results it is possible to notice how the high resolution differences lead to a poor data visualization, particularly for the 1999-2008 case (Figure 68 (a)), where the horizonal and vertical stripes do not allow any interpretation. For the 1999-2018 (Figure 68 (b)) case instead, although the grid pattern is still evident, the result is more clear. This partially explains why in Section 3 (Analysis of Superficial Variations), the 2008 layer was subject to a heavier processing compared to the 2018 one. The other reason, as already discussed, lies in the huge resolution difference between the 1999 and 2018 models, which did not allow any resample of the latter over the resolution of the first one. By simply applying a low pass filter to the result shown in Figure 68 (b), it was possible to obtain the final DEM difference displayed in Figure 16 (c).

Figure 69 shows the difference between the 1999 DEM and the one of 2008, where this latter was resampled over the cell resolution of the coarser one. In this case, the results look better and more information can be retrieved compared to the case of Figure 68 (a). However, the grid distribution is still heavily visible, explaining why, in the end, it was chosen to also apply the low pass filter to this result (Figure 17).

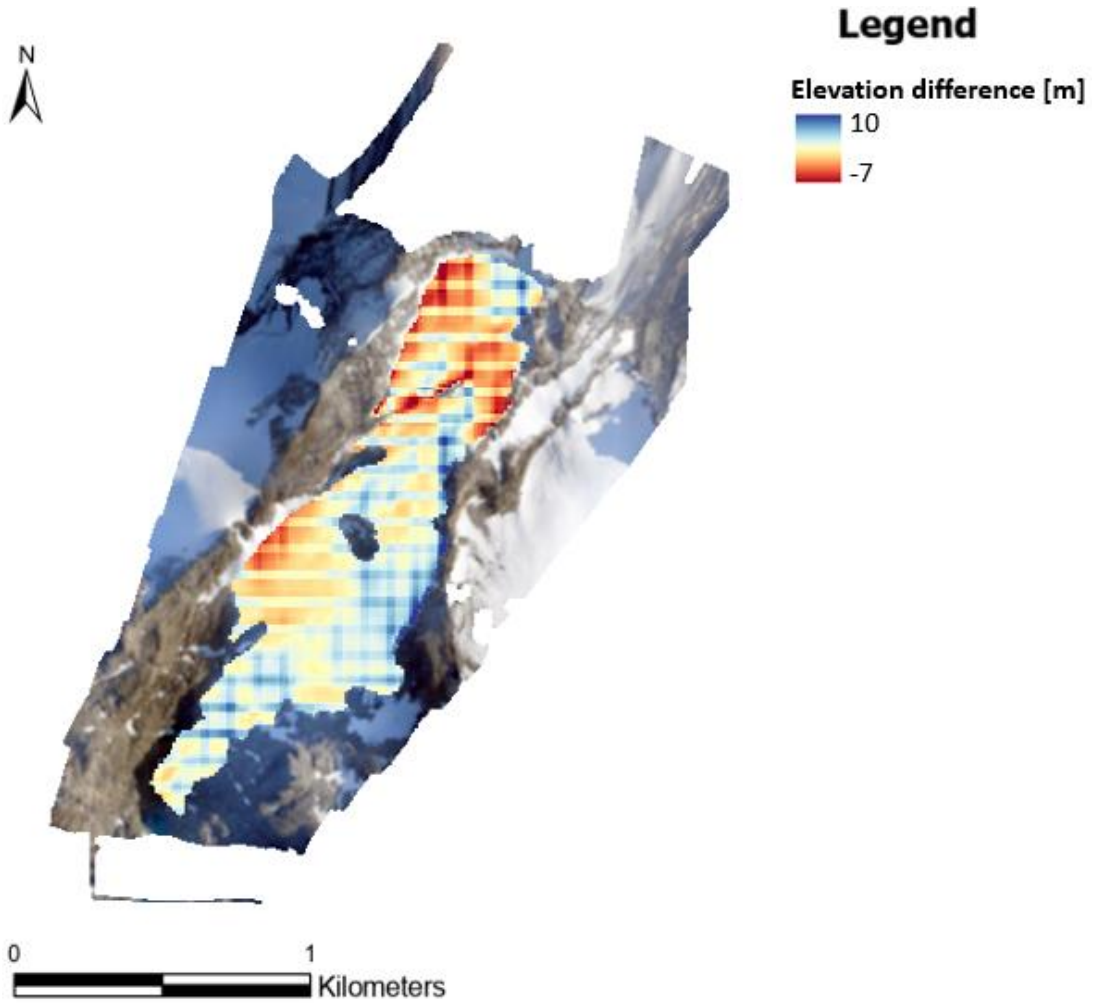

Figure 69: *Digital Elevation Models differences between 1999 and 2008. The 2008 model was resampled to the 1999 resolution, no filter was applied.*

For the sake of completeness it was also chosen to analyze the results obtained by subtracting the original 1999 and 2008 layers (i.e., without resampling processing) and applying the low pass filter to this difference, similarly to the 1999-2018 case. The result is shown in Figure 70.

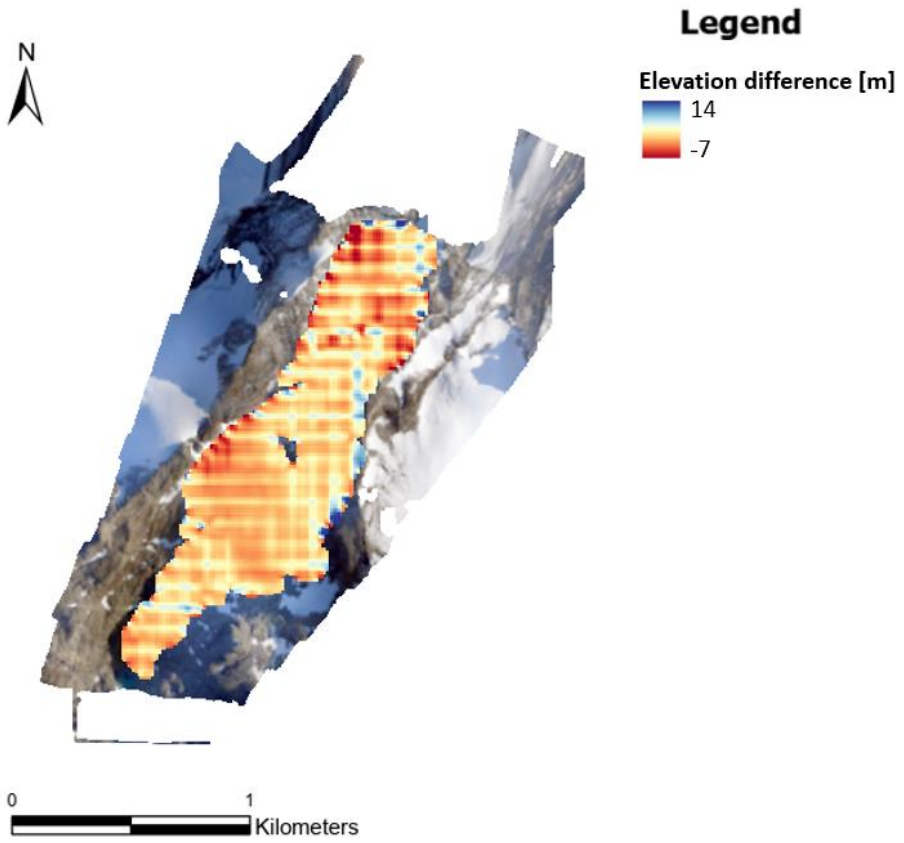

Figure 70: *Original Digital Elevation Models differences between 1999 and 2008. A low pass filter was applied to the difference.*

As it is possible to see, the obtained result is very poor and no clear data interpretation can be performed.

Finally, comparing the original color scale of the 1999-2008 difference (Figure 68 (a)) with the one obtained after the whole processing procedure (Figure 17), it can be noted that a loss of information has occurred during the smoothing techniques. In particular, both the resampling and the low pass filter have contributed to the loss of extreme values in the final result. However, it is evident how keeping the original data (Figure 68 (a)) would have not been feasible from an interpretation point of view, thus it was still decided to work with the smoothened results for the preliminary analysis of ice thickness variations.

Appendix B

In the following section the temperature analysis for Capanna Margherita and Gabiet stations will be addressed. For this purpose, the same procedure applied to Bocchetta delle Pisse station was followed. Therefore, here, only the results coming out from the different steps of the processing will be shown.

The original datasets are shown in Figure 71.

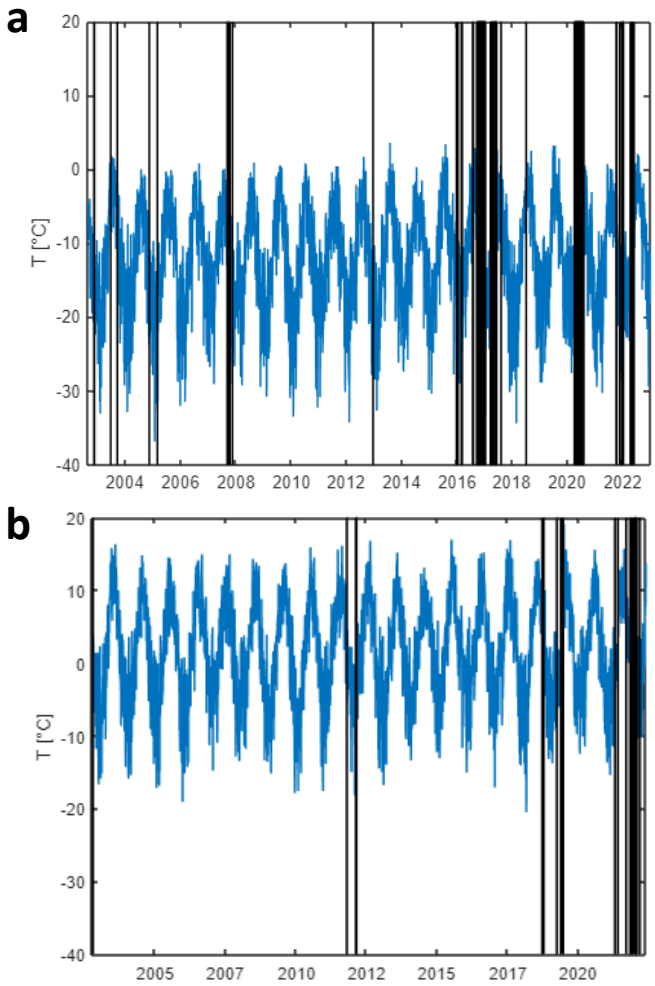

Figure 71*: Raw temperature data acquired at (a) Capanna Margherita (2002-2022) and (b) Gabiet (2002-2022).*

Looking at the timeseries of Capanna Margherita it is possible to notice a large absence of measurements in 2017, whereas for Gabiet station, mostly 2022 is missing.

The obtained results after the gap filling procedure are represented in Figure 72.

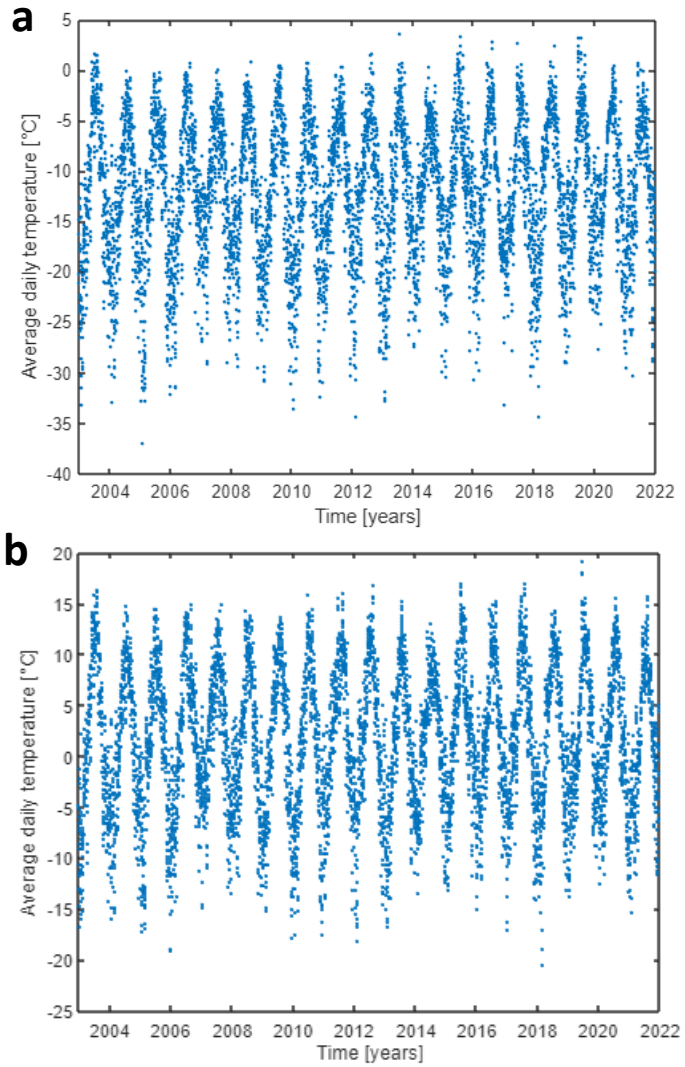

Figure 72: *Temperature data after gap filling process: (a) Capanna Margherita and (b) Gabiet.*

The spectral features of the datasets used for the definition of the harmonic components of the datasets are shown in Figure 73.

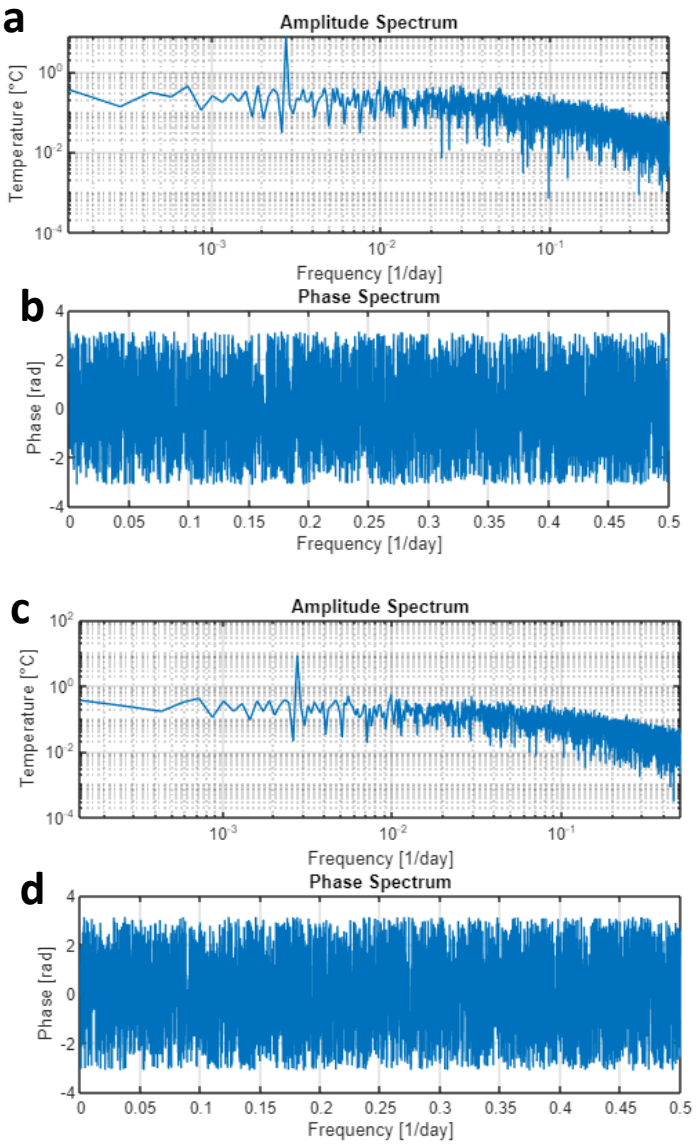

FIGURE 73: *(a) Amplitude Spectrum (b) Phase Spectrum of Capanna Margherita temperature data. (c) Amplitude Spectrum (d) Phase Spectrum of Gabiet temperature data.*

The astronomic components retrieved through Equation 23 are represented in red in Figure 74.

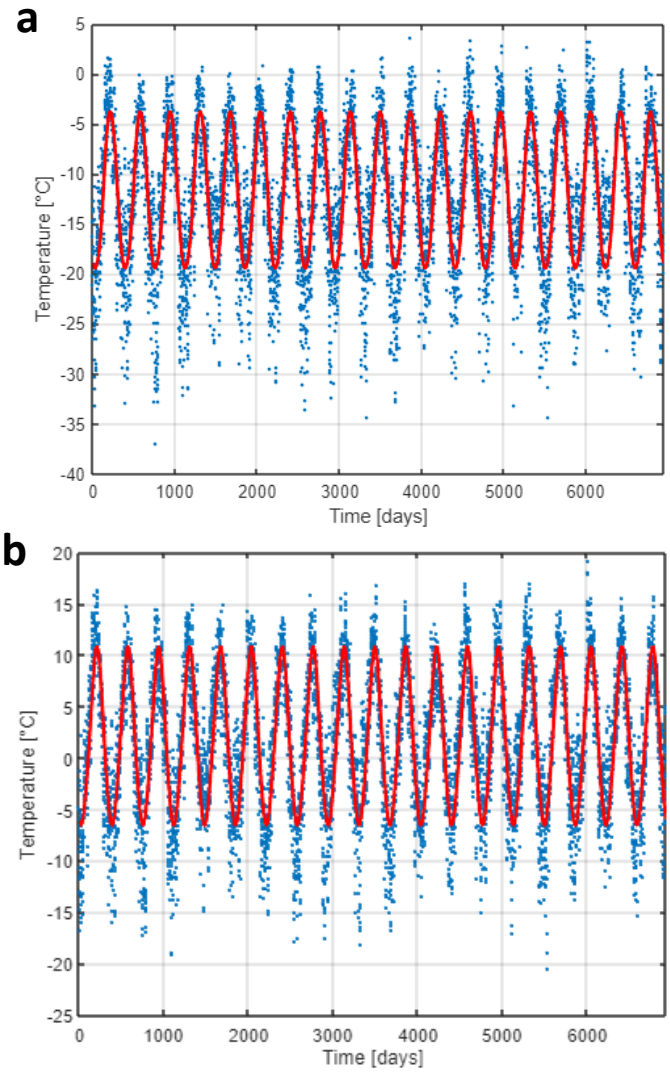

Figure 74: *Temperature data (blue) with astronomic component (red) at (a) Capanna Margherita and (b) Gabiet.*

The residuals obtained after the periodic component removal are shown in Figure 75.

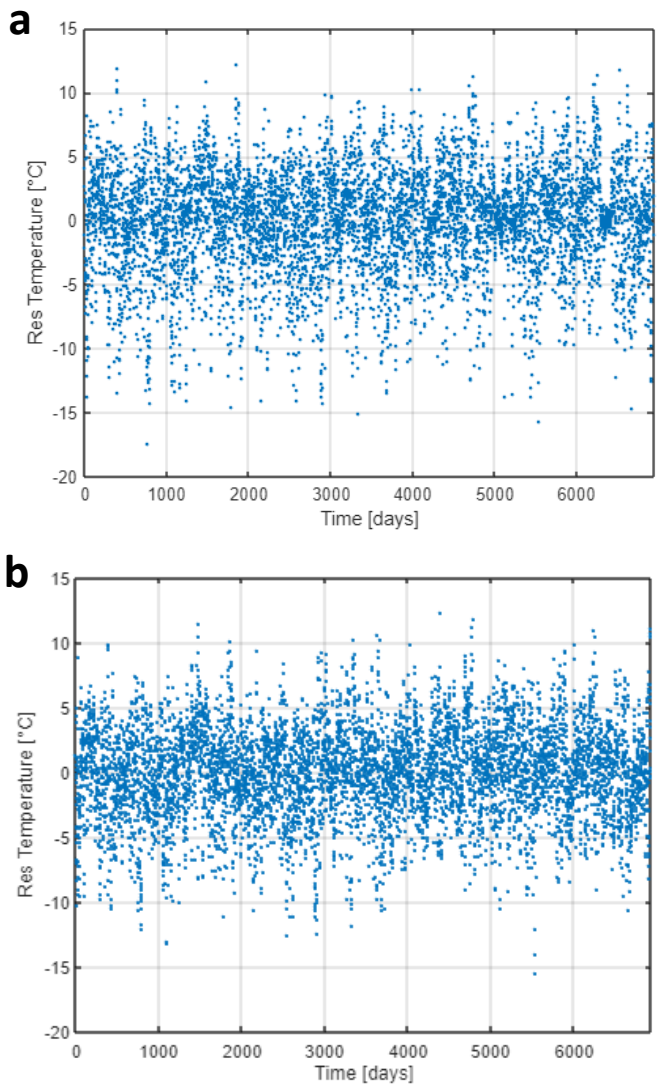

Figure 75*: Data residuals obtained through the removal of the astronomic component at (a) Capanna Margherita and (b) Gabiet.*

The final regression lines obtained through the residuals interpolation is visible in Figure 76.

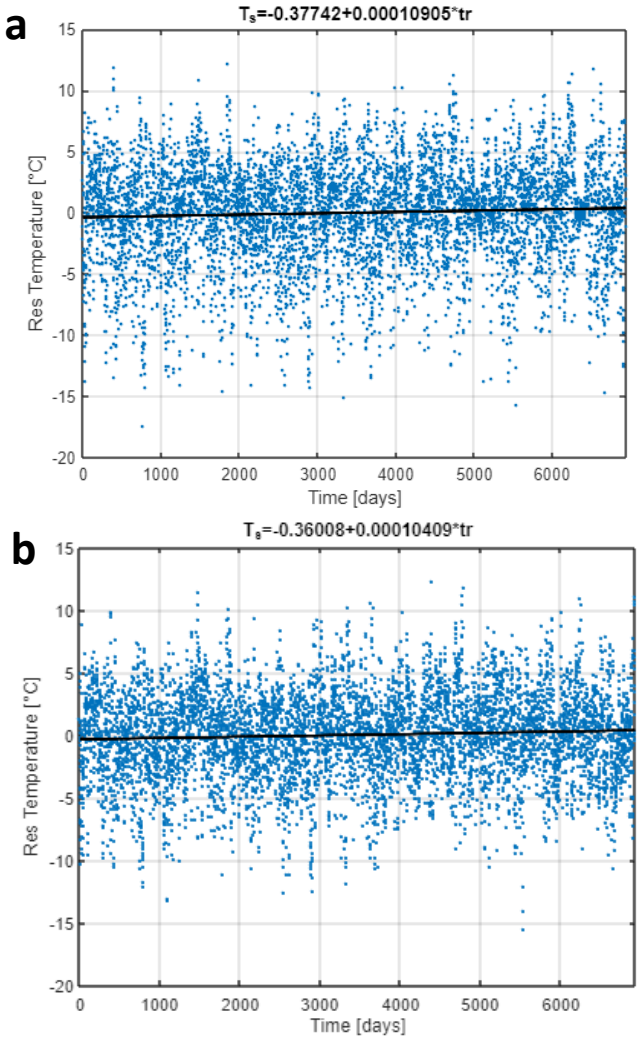

FIGURE 76: *Data residuals (blue) with linear regression (black) at (a) Capanna Margherita and (b) Gabiet.*

For the estimation of the temperature trend measured over the two considered stations, refer to Table 3.